Study on
Noise Features of Magnetron
and
Low Noise Wireless Power Transmission

Tomohiko Mitani

Study on
Noise Features of Magnetron
and
Low Noise Wireless Power Transmission

Tomohiko Mitani

December 2005

Thesis Supervisor: Prof. Hiroshi Matsumoto

Acknowledgments

I would like to express my sincere appreciation to my research supervisor Professor Hiroshi Matsumoto for providing me the wonderful opportunity to conduct the present study on Solar Power Satellite/Station (SPS) and Wireless Power Transmission (WPT). I am also grateful deeply to him for his continual and reliable guidance and constructive discussions on the present study.

I would like to express my deep appreciation to Professor Kozo Hashimoto for fruitful discussions and helpful comments throughout the present study. I am also grateful to him for his careful reading of the present thesis and his critical opinions in every detail.

I would like to express my sincere acknowledgment to Professor Yoshiharu Omura for the revision of the present thesis from the viewpoint of plasma science and computer simulation. I am also grateful to him for instructing me on the importance of English.

I would like to express my cordial appreciation to Dr. Naoki Shinohara for his continual guidance and significant discussions on the present study. I am also deeply grateful to him for his work as a young coordinator for the SPS research group in our laboratories.

I am grateful to Dr. Hideyuki Usui for his advice from the viewpoint of numerical simulations of a magnetron. I am also grateful to Dr. Hirotsugu Kojima for instructing me on the importance of the process on the present study. I would like to thank Dr. Yoshikatsu Ueda and Dr. Takayuki Umeda for their encouragement and helpful assistance. I am deeply grateful to all the colleagues of the SPS research group in our laboratories for their helpful assistance on the present study.

I would like to express my heartfelt appreciation to Ms. Keiko Miwa for her office administration and encouragement in the present study. I am deeply grateful to Ms. Chieko Kita for her office work of the laboratory I engage in. I am also deeply grateful to Ms. Tomomi Kawamata, Ms. Junko Kawamoto, Ms. Michiyo Koyama and all the secretaries of our research group for their office work and encouragement. I wish to thank all the staff of Research Institute for Sustainable Humanosphere (RISH) for their kind hospitality and encouragement.

I would like to express my deep acknowledgment to Mr. Masayuki Aiga, Ms. Nagisa Kuwahara, Mr. Toshiyuki Tsukada, Mr. Takanori Handa, Mr. Takeshi Ishii and all the staff of Utsunomiya Hiraide Plant, Panasonic Semiconductor Discrete Devices Co., Ltd. for collaborating on the improvement of an oven magnetron, for designing and manufacturing many samples of magnetrons, and for productive discussions on the present study.

The experiments of the present study have been conducted at Microwave Energy Transmission Laboratory (METLAB), which is served for the collaborative research programs of RISH, and Solar Power Satellite/Station Laboratory (SPSLAB).

Finally, I would like to thank my parents Kiyoshi and Takako, my sister Aya, her husband Jun and my grandfather Bunji for their continuous encouragements and hearty support in my private life.

Abstract

A magnetron is a kind of microwave tube, and well-known as a microwave heating source in a microwave oven. Besides, it is one of the strong candidates for a microwave power source of a future Wireless Power Transmission (WPT) system and a transmitter of Solar Power Station /Satellite (SPS) projects because its DC-RF conversion efficiency is higher, it costs less, and it has smaller weight/power ratio than solid state devices. However, a magnetron has a wide oscillation bandwidth and it generates spurious noises in various frequency bands. The wide bandwidth of the fundamental frequency represents a critical problem that a microwave beam from a SPS is unable to be focused stably to a receiving site. The spurious noises in various frequency bands are difficult to be prevented, and their radiation from a SPS transmitting system will severely interfere with other radio applications. Hence, it is indispensable to employ measures against the noise radiation from the SPS transmitting system.

Besides, a microwave oven has been facing a serious problem of electromagnetic compatibility (EMC) with other radio applications, by the drastic advancements in communication technology and information technology (IT). Line noises generated from a magnetron may interfere with broadcast communications in the MF, VHF and UHF bands, so that a microwave oven is obliged to have filters installed not only inside the magnetron but also in the power supply circuit. Moreover, the emergence of wireless-LAN (WLAN) owing to IT-related developments raises a new issue of EMC between a microwave oven and WLAN.

This thesis is devoted to a study on noise features of a magnetron and low noise WPT, in order to develop both a magnetron and a WPT system which are compatible with other radio applications of the day.

Firstly, we have conducted experimental measurements of electron emission from the filament cathode of a magnetron in order to obtain necessary data for discussing generation mechanisms of noises from a magnetron. From the experimental measurements of the anode current with axially-segmented anode blocks, we estimated the trajectory and diffusive motion of an electron. From the experimental results of the filament temperature, we have found out that the filament temperature is high enough to sustain the oscillation by the internal feedback mechanism even after the filament current is turned off, and that the filament temperature falls much more on both the filament ends, especially on the RF output side of the filament than at the center. Summarizing these experimental results above from the viewpoint of electron emission from the cathode filament, we concluded that the examined magnetrons denoted the tendency that electrons are estimated to be emitted most in the center region, next on the HV input side, and least on the RF output side.

Secondly, we have conducted a time domain analysis of magnetron noises. From the analysis, we have found out that spurious noises generated from a magnetron are classified into the following five types; (1) side band noises around the carrier and low frequency line noises at frequencies below about 150MHz, generated at an anode current of less than 0.2A, (2) high frequency spurious noises and low frequency line noises generated in the transition

region between the constant voltage range and the non-constant voltage range at an anode current of around 0.4A, (3) low frequency line noises generated in the non-constant voltage range characterized by frequencies of 400MHz or 800MHz and high frequency spurious noises, generated at an anode current of around 0.6A, attributed to the intermodulation of the low frequency line noises and the harmonics, (4) the harmonics generated in synchrony with the fundamental, and (5) low frequency line noises generated in synchrony with the electron circulation. We also discussed generation mechanisms of spurious noises from a magnetron with respect to each classification.

Thirdly, we have studied newly-designed low noise magnetrons. With regard to the modifications of the interaction space and the anode voltage, we have found that the wider the interaction space and the lower the anode voltage, the less the spurious noises are generated from a magnetron. Also, we found out that the modification of the anode voltage is more effective than that of the interaction space. With regard to newly-designed magnetrons with cathode shields, we conclude that a cathode shield attached to the end of the cathode filament works effectively for suppressing line noises when it is designed to correspond to the axial distribution of the filament temperature.

Finally, we have studied noise features of a filament-off magnetron for the use of WPT. We verified that turning off the filament current worked very well not only for a narrower oscillation bandwidth but also for suppression of spurious noises generated from a magnetron. In terms of oscillation bandwidth, we have found out that there are two main causes that the oscillation bandwidth of the filament-off magnetron becomes narrower; one is the disappearance of the disturbance in the anode current, and the other is the decrease of thermal effects by reduction of the filament temperature. In terms of spurious noises, we conclude that the dominant cause of the noise reduction is suppression of electron motions around the filament ends due to the falloff of the filament temperature, throughout the experimental measurements of the various magnetrons. We have also found out that there is the intermodulation between the low frequency line noises and the fundamental or the harmonics, and that high frequency radiation noises of the filament-off magnetron are suppressed greatly because of the suppression of the low frequency spurious noises.

Contents

List of Figures

List of Tables

Chapter 1

General Introduction

1.1 Magnetron

1.1.1 History of magnetron

A magnetron is a kind of cross-field electric tube, in which the applied magnetic field is perpendicular to the electric field. The cathode is set on the central axis and the cylindrical anode is on the same axis. The primitive magnetron was invented by A.W. Hull [1], its output power was, however, very small and its DC-RF efficiency is quite low because of the slight oscillation, what is called A-type oscillation. Since the segment-anode magnetron was invented by K. Okabe [2], magnetrons have been oscillated at microwave frequencies with much larger output power, what is called B-type oscillation, and its DC-RF efficiency has become drastically high. Then, the anode with internal cavity resonators and strap rings was devised to improve the oscillation more efficiently.

Magnetrons are classified into pulsed types and CW types. Pulsed magnetrons are used for radar systems. CW magnetrons are widely used for microwave heating, especially for ovens. Cooker-type CW magnetrons are used as a heating source of a microwave oven all over the world so that they are quite inexpensive. CW magnetrons are also utilized for microwave drying, medical treatment etc.

Early magnetrons were utilized as transmitters of radar systems. Hence, early studies of magnetrons have been aimed at generating high microwave power with high DC-RF efficiency, although many researchers and companies are ongoingly studying in order to achieve the purpose. After World War II, Raytheon Company invented a microwave oven and marketed it in 1953 [2]. Since its release, a microwave oven has had explosive sales as a home electric appliance.

However, a microwave oven has been facing a serious problem by the drastic advancements in communication technology and information technology (IT). This is electromagnetic compatibility (EMC). The early problem for a microwave oven on EMC was between line conductive noises from a magnetron and broadcast communication services. It is known that a mag-

netron widely and continuously generates noises from the order of kHz to 1GHz (*e.g.* [3]). If they propagate, these line noises may interfere with radio services in the MF band and television broadcasts in the VHF and UHF bands [4]. Studies and investigations of noises generated from magnetrons have been extensively reported in order to solve the problem [3–6]. Despite these exhaustive investigations, a satisfactory solution for a magnetron has not emerged yet, thus a microwave oven is obliged to have filters installed not only inside a magnetron but also in a power supply circuit in order to prevent these noises from propagation.

Moreover, the emergence of wireless-LAN (WLAN) owing to IT-related developments raises a new issue of EMC between a microwave oven and WLAN. Especially, the WLAN systems in the 2.4GHz band such as Bluetooth and IEEE 802.11b are allocated in the same ISM (Industrial, Scientific, and Medical) band as the carrier frequency of a microwave oven. Therefore, studies and investigations on this EMC issue has been conducted [7, 8], although the existence of a microwave oven has recognized since early times.

As described above, the EMC problems between a magnetron in a microwave oven and the communication systems have recently emerged as a hot research topic.

1.1.2 Principle of oscillation

A typical cross-section view of a present magnetron is shown in Fig. 1.1. The DC electric field $\boldsymbol{E}$ is applied between the anode and the cathode in a radial manner. The external magnetic field $\boldsymbol{B}$ perpendicular to $\boldsymbol{E}$ lets electrons, emitted from the cathode, go into $\boldsymbol{E} \times \boldsymbol{B}$ drift motion by the equation of motion

$$m\frac{d\boldsymbol{v}}{dt} = -e(\boldsymbol{E} + \boldsymbol{v} \times \boldsymbol{B}), \tag{1.1}$$

where e is the electron charge, m is the electron mass and $\boldsymbol{v}$ is the electron velocity.

The anode typically consists of even numbers of metal vanes and sectoral cavities. These cavities have the admittance matching with the interaction space between the anode and the cathode. Magnetrons are usually designed to have the π-mode oscillation, which is the mode that the phase difference of the microwave oscillation between the adjacent resonant cavities is π. The π mode is separated from all other non-π modes with strap rings, which are conductors connected to alternate anode vanes of the magnetron, as shown in Fig. 1.1.

Now, we describe the oscillation mechanism of a magnetron with a two-dimensional linear magnetron in the Cartesian coordinates, shown in Fig. 1.2, for ease of expression. First, the oscillation of a magnetron is triggered by slight RF noises generated in the magnetron tube when the anode voltage reaches the oscillation point. Then, the RF electric field is selectively vibrated in the π mode owing to the resonant cavities and the strap rings. When a RF potential on an anode vane becomes the minimum, the RF potentials on the adjacent anode vanes and the RF electric field lines are depicted as shown in Fig. 1.2. Then, there is an RF electric field $E_{\mathrm{rf}}(x, y, t)$ in addition to the electrostatic field E_{dc} between the cathode and the anode in a magnetron. Now the equation of motion Eq. (1.1) is rewritten with the electron

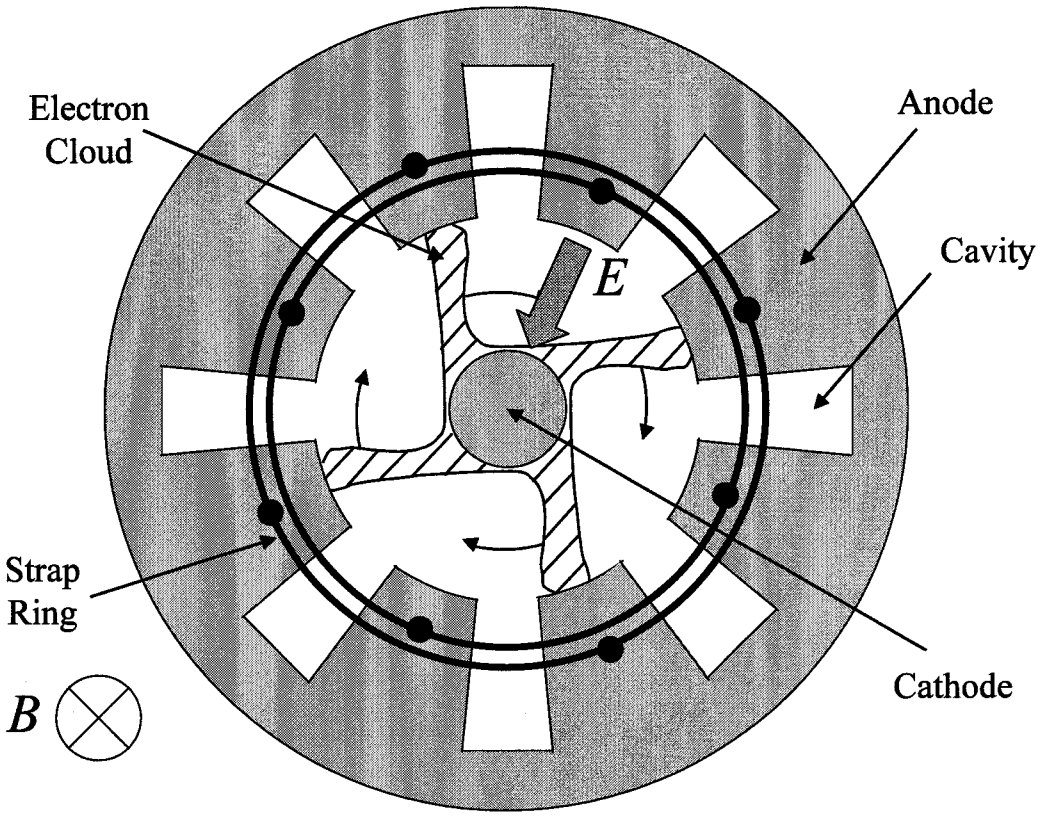

Figure 1.1: Cross-section view of a magnetron.

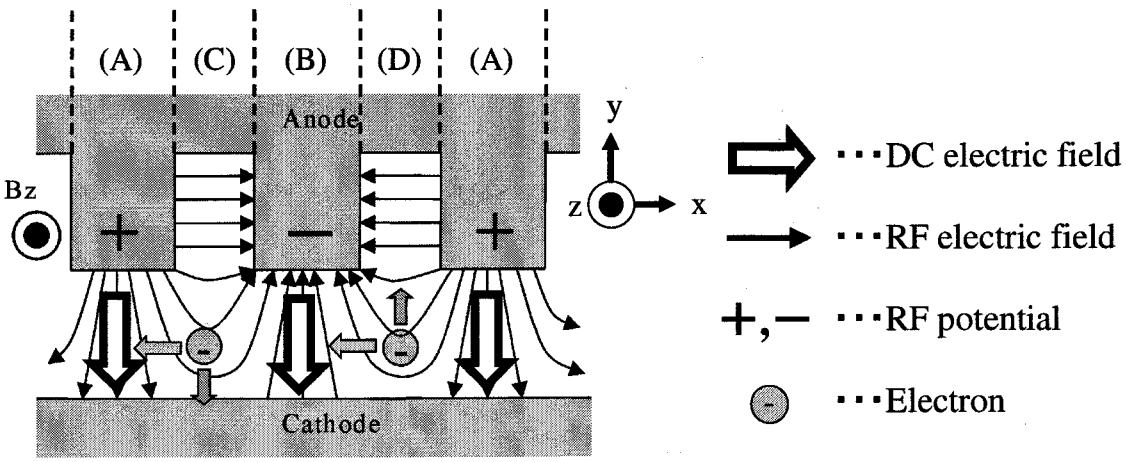

Figure 1.2: Schematic of a two-dimensional linear magnetron.

velocity $v = (v_x, v_y)$;

$$m\frac{dv_x}{dt} = -e(E_{\rm rf}(x,t) + v_y B) \tag{1.2}$$

$$m\frac{dv_y}{dt} = -e(E_{\rm dc} + E_{\rm rf}(y,t) - v_x B). \tag{1.3}$$

Then, substituting v_y in Eq. (1.2) and v_x in Eq. (1.3) for Eq. (1.3) and Eq. (1.2), respectively, then

$$\frac{m^2}{e^2B^2}\frac{d^2v_x}{dt^2} + v_x = -\frac{E_{\rm dc}}{B} - \frac{E_{\rm rf}(y,t)}{B} \tag{1.4}$$

$$\frac{m^2}{e^2B^2}\frac{d^2v_y}{dt^2} + v_y = -\frac{E_{\rm rf}(x,t)}{B}. \tag{1.5}$$

If there is no RF electric field *i.e.* $E_{\rm rf} = 0$, an electron motion is famously expressed as a cycloid motion, a cyclotron motion with a drift motion in the x direction. Hence, an electron motion in a magnetron, expressed by Eq. (1.4) and Eq. (1.5), shows the cyclotron motion with another drift motion in the y direction as well as the x direction.

Now the electron motion in the interaction space is divided into four regions by the position of an electron in the x axis: (A) an electron is passing through the positive RF potential, (B) an electron is passing through the negative RF potential, (C) an electron is passing from a negative RF potential to a positive RF potential, as the left-hand electron shown in Fig. 1.2, and (D) an electron is passing from a positive RF potential to a negative RF potential as the right-hand electron shown in Fig. 1.2. In the region (A), the electron accelerates in the x direction since the RF field in the y direction enhances the drift motion; on the other hand, it decelerate in the region (B) since the RF field in the y direction lessen the drift motion. Then, electrons are gradually bunched and they shift to either the region (C) or the region (D). In the region (C), the RF field in the x direction makes electrons move to the cathode by the drift motion in the y direction expressed by Eq. (1.5); on the other hand, electrons in the region (D) move toward the anode vanes. After all, electrons gradually form spoke-shaped electron clouds in the interaction space, as shown in Fig. 1.1. Every time the electron spokes pass through the edge of the resonant cavities, the induced current flows from the positive RF potential to the negative RF potential. Therefore, electrons behave as a negative resistance to the RF field, and finally repetition of these mechanisms above leads to the oscillation.

1.1.3 Reference magnetron in the present study

The magnetron model 2M210M1F1 manufactured by Panasonic Semiconductor Discrete Devices Co., Ltd. is used as the reference magnetron in the present study. A cross-section image of the reference magnetron in the $r - z$ plane is shown in Fig 1.3, where r and z is defined as the radial and axial direction, respectively. The reference magnetron as well as a conventional oven magnetron has a filament in order to produce thermal electrons, and the filament also play a role of the cathode.

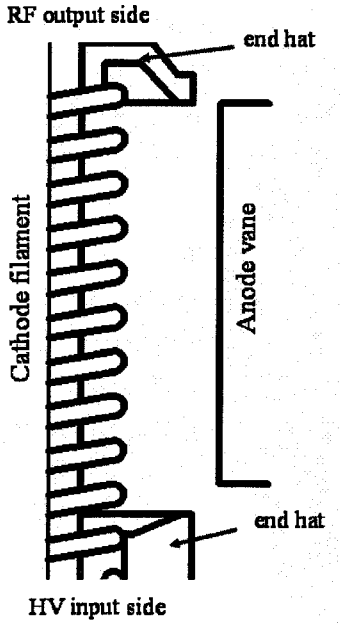

Figure 1.3: Cross-section image of the reference magnetron in the $r - z$ plane.

Table 1.1: Normal rated values of the reference magnetron 2M210M1F1.

Frequency	2.455GHz
Peak anode voltage	4.1kV
Mean anode current	300mAdc
AC filament current	10A

When it is driven by an unsmoothed full-wave rectified power supply, the normal rated values of 2M210M1F1 are put in Table 1.1. The anode current and the anode voltage can be replaced by the operating current and the operating voltage of the magnetron, respectively.

1.2 Wireless Power Transmission (WPT)

Radio wave technologies have been one of the most indispensable social foundations in our human society since J. C. Maxwell propounded the existence of radio wave theoretically in 1864. One of the well-known radio applications is wireless communication services such as radio and television broadcasting services, satellite broadcasting services, cell phone systems, WLAN etc. The radio wave is also applied to remote sensing services such as radar systems and sensors. These applications utilize the radio wave as a media to communicate or to detect information. Moreover, we utilize the radio wave, especially microwave, as an energy source. Its representative example is microwave heating of foods with a microwave oven.

The most important thing is that all the radio applications described above are based on wireless electromagnetic energy transmission. The nature of the radio wave has been reconsidered by an innovative field what is called Wireless Power Transmission (WPT) or Microwave Power Transmission (MPT) since the late of 20th century. Most of the WPT studies have been MPT studies, therefore WPT is deemed to MPT hereafter.

The history of WPT is said to have began around the early part of the 20th century when N. Tesla put forward its possibility [9,10]. He actually built up a huge coil with a ball of 3 feet in diameter on the top of a mast of 200 feet in height, and conducted the WPT experiment of 300kW at a frequency of 150kHz. It was hard to say that this experiment was successful due to its overlong wavelength. Then, the WPT was behind wireless communication technologies. The review of the WPT was triggered by the inventions of high power microwave tubes such as klystrons and magnetrons around the early 20th century. Then, W. C. Brown and his group have mostly contributed to studies on the WPT with microwave, that is, the MPT in 1960s [11]. He conducted his first practical WPT experiments in 1963 and succeeded in the demonstration of a microwave powered helicopter, as a photo of their demonstration is shown in Fig 1.4 [11]. Then, he and his group have achieved a certified overall DC to DC efficiency of 54%, which is still the world record for the overall efficiency of WPT systems, as a photo of their demonstrations is shown in Fig 1.5 [11]. They have also conducted the demonstration of the WPT over a distance of 1 mile, as a photo of their demonstrations is shown in Fig 1.6 [11].

The pioneering works on the WPT by Brown and his group has been motivating a lot of engineers and scientists in the world to research and development related the WPT technology. A research group in Kyoto University is one of the most active groups engaging in the WPT and a SPS, which is described in the next section, deeply. Various experiments

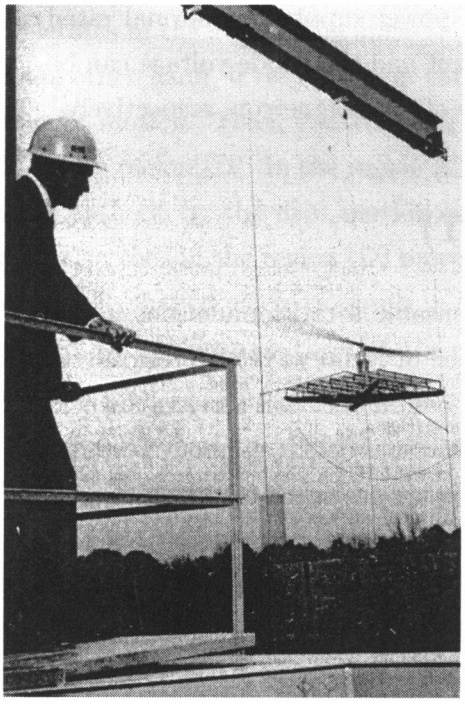

Figure 1.4: Demonstration of a microwave powered helicopter in 1964 [11].

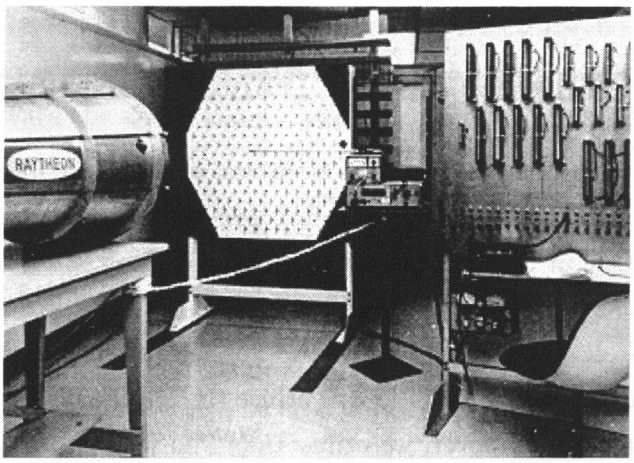

Figure 1.5: Certified demonstration of 54% overall DC to DC efficiency in 1975 [11].

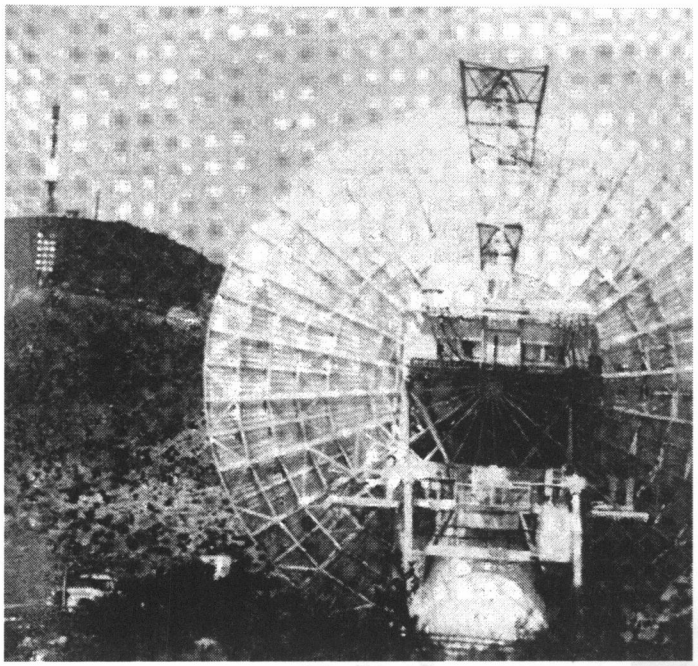

Figure 1.6: Demonstration of beamed power over 1 mile distance [11].

on the WPT has been conducted by the research group in Kyoto University and other co-operative research groups, whose research activities are condensed into [12]. In 1983, they have succeeded in the world first rocket experiment on the WPT in the ionosphere called MINIX (Microwave Ionosphere Nonlinear Interaction eXperiment) [13, 14], as a photo and an experimental result are shown in Fig. 1.7. The transmitting antenna in the MINIX is just a truncated waveguide. In 1993, they have succeeded in the second rocket experiment called ISY-METS (International Space Year - Microwave Energy Transmission in Space) [15] as a photo of ISY-METS is shown in Fig. 1.8. In the ISY-METS, a phased array system was employed as the transmitting system. In terms of the ground experiments, the WPT experiment to an airplane called MILAX (MIcrowave Lifted Airplane eXperiment) was conducted in 1992, as photos of the MILAX are shown in Fig. 1.9 [12]. A phased array system was also employed as the transmitting system in the MILAX, therefore the microwave beam was able to chase the airplane whose propeller was driven only by the rectified power from microwave. In 1994-95, the first ground-to-ground WPT experiment in Japan called the "Yamazaki" experiment (Yamazaki is the name of the town where the experiment was held.) was conducted [16], as a photo of the Yamazaki experiment is shown in Fig 1.10. A microwave power of 5kW was transmitted to rectenna arrays over a distance of 42m.

With regard to the ground-to-ground WPT experiments, there are some ongoing WPT projects; WPT experiments in La Réunion Island [17], and in Hawaii [18]. These future plans show that the commercial viability of the WPT applications is being researched actively and earnestly all over the world.

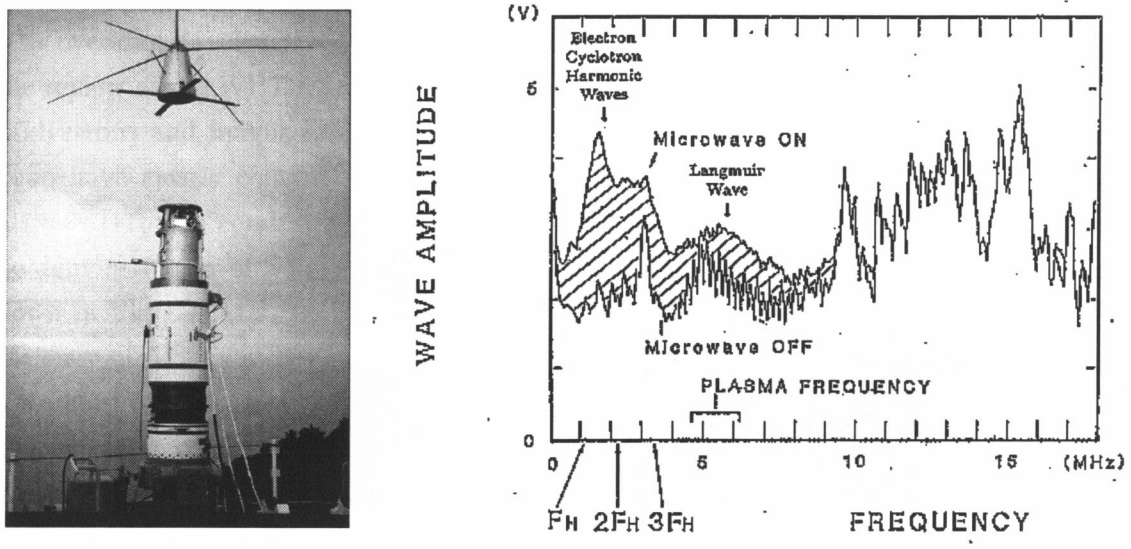

Figure 1.7: Photo of the MINIX at the launching site (left) [13], and plasma wave spectra measured in the MINIX (right) [14].

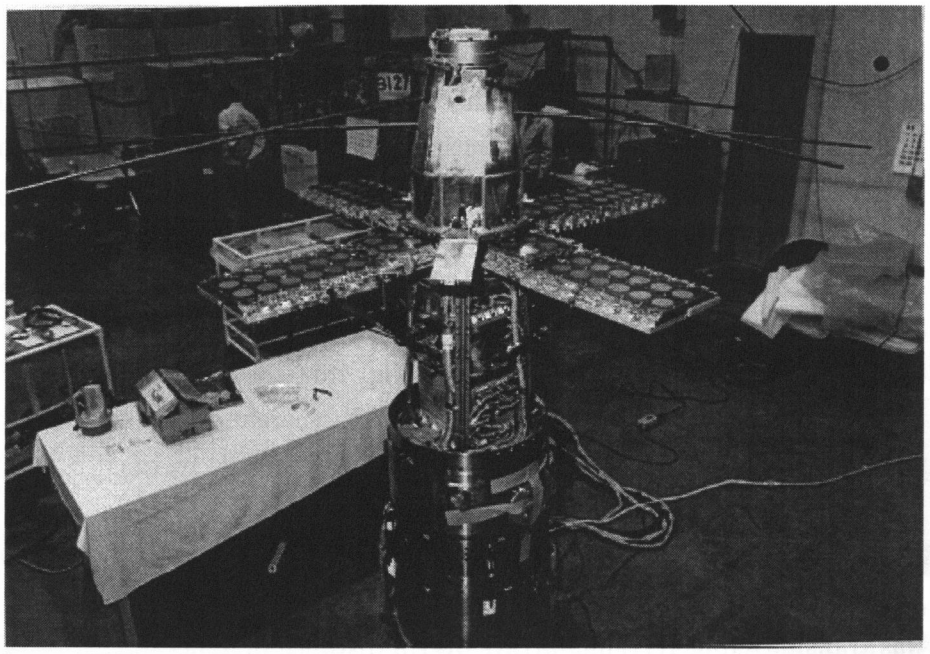

Figure 1.8: Photo of the ISY-METS

Figure 1.9: Photos of the MILAX [12].

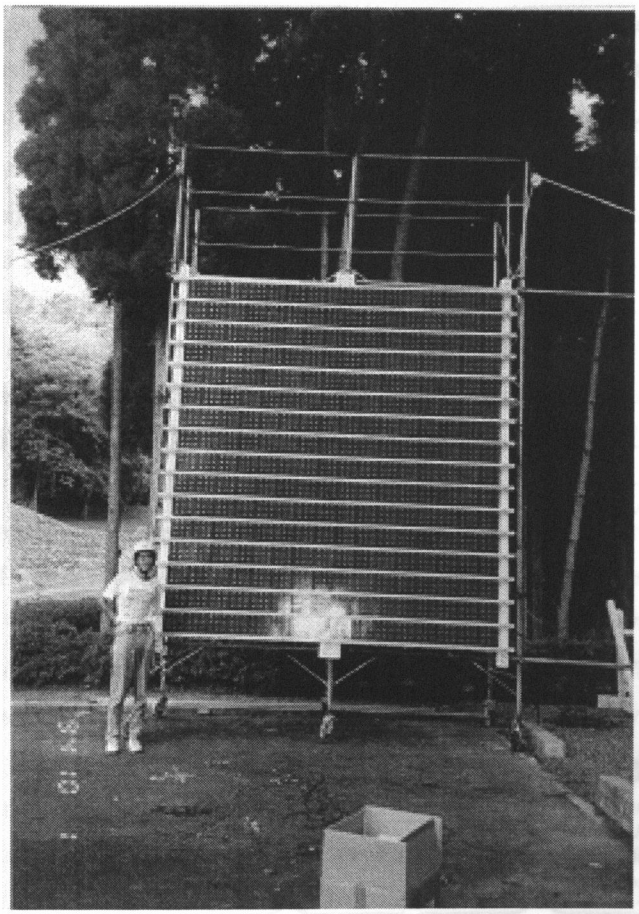

Figure 1.10: Photo of the rectenna array for the Yamazaki experiment.

A basic concept of the WPT is shown in Fig. 1.11. The WPT system is mainly divided into three sections: the transmitting section, the receiving section and the beam forming section. The transmitting section consists of DC-RF converters and transmitting antennas. The DC-RF converters mainly include electric tubes such as magnetrons, klystrons, TWTs etc., or solid state devices. The receiving section consists of receiving antennas and RF-DC rectifiers, which are generally called "rectennas" by combining two words: rectifiers and antennas. Studies on rectennas have been conducted by W. C. Brown [11], who holds the world record of the RF-DC conversion efficiency, and several researchers in Japan (e.g. [16, 19]). CWCs (Cyclotron Wave Converters) [20, 21] can be alternatives to the RF-DC rectifiers. The beam forming section is the intermediate section between the transmitting section and the receiving section. In order to prevent the power dissipation through the beam forming section, the transmitting section usually involves a high-gain transmitting antenna or a phased array system.

The accuracy of the beam control to the desired receiving site is also important. In the case of a SPS, a pilot signal is considered to be transmitted from the receiving site and the SPS transmits RF energy back to the arrival direction of the pilot signal. A typical way to realize these processes above is a retrodirective system [22]. A research group in the United States and our research group in Kyoto University have also studied and developed a retrodirective power transmitter [12, 23], and we have also studied a beam control system with spread-spectrum pilot signals [24].

The most significant difference between the WPT and wireless communication services is the management of the RF energy. The wireless communication services, especially broadcasting services and mobile communication systems require the efficient transmission of in-

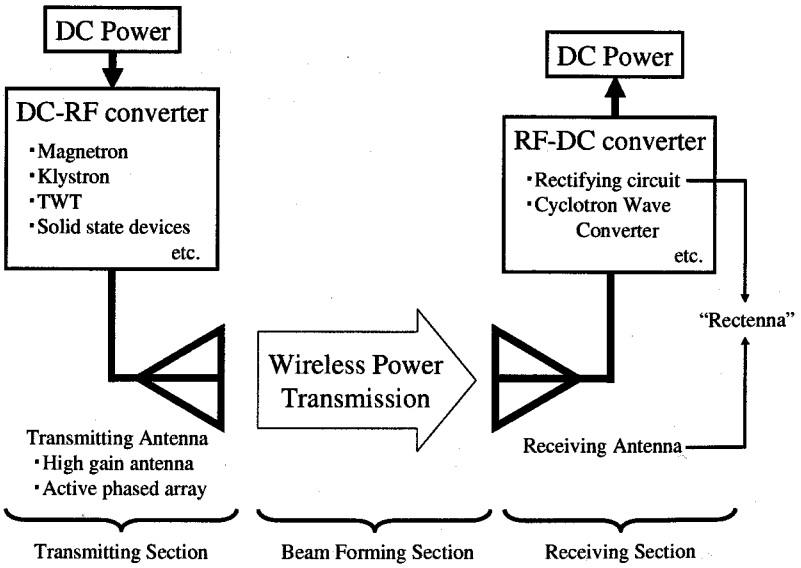

Figure 1.11: Basic concept of Wireless Power Transmission (WPT).

formation for service areas. Hence, the RF energy from the base station needs to be widely radiated. The WPT, on the other hand, requires the efficient transmission of the RF energy itself, hence the RF energy from the transmitting system should be focused only on the receiving site. High-efficiency and low loss are radically required of all the elements of the WPT system, which include the DC-RF converter on the transmitter, the beam control system, the RF-DC converter on the receiver etc.

The WPT services are of benefit at the places where it is impossible or it cost too much to install the fixed power transmission lines, for example, isolated islands, a mountain top etc. In the previous studies in Kyoto University, the WPT applications to a search robot in a gas pipe [25] and to an electric car [26,27] have been researched. Also, a Ubiquitous Power Service (UPS) by the WPT is also being studied in Kyoto University [28]. The UPS is one of the most suitable WPT applications for practical use. It ubiquitously supplies the electric power to small-powered devices such as cellular phones etc. with the WPT technology.

Above all, the biggest project of the WPT applications is a Solar Power Satellite/Station (SPS) project, described in the next section.

1.3 Solar Power Station/Satellite (SPS)

Rapid economic and population growth in the 20th and 21st centuries involves rapid increase in demand for energy. According to International Energy Agency, the world total energy supply in 2030 is projected to increase by 160% compared to that in 2001, and it highly depends on fossil fuels such as oil, coal, and natural gas by 80% in 2001 and will still depend on them by 83% in 2030 [29]. On the other hand, it is well-known that fossil fuels heavily lead to the carbon dioxide emission and their exhaustion will increasingly pose a severe problem to human life. Nuclear energy also has a serious problem in disposal of nuclear fuel wastes and nuclear accidents although it is COx and NOx emission-free. Sustainable energy resources such as solar energy, wind energy, hydro-energy, biomass energy etc. have therefore been a focus of constant attention as alternatives to fossil fuels. They however have a disadvantage for a stable supply of energy because the amount of their energy varies seasonally, or daily, or even momentarily.

A Solar Power Station/Satellite (SPS), which has being studied by researchers, scientists, engineers, or even economists, is expected to become one of the energy sources for the next generation under the current circumstances described above. The SPS is clean and exhaustless since it is a power station whose resource is solar energy. Furthermore, the SPS supplies a stable electric power almost all through the year except that it is eclipsed by the Earth, because the power generated in space, in other words, there is no seasonal and daily variation by clouds, rain, and nights.

The SPS was originally devised by P. E. Glaser in 1968 [30,31], and its concept design was developed by a collaboration of Department of Energy (DOE) and the National Aeronautics

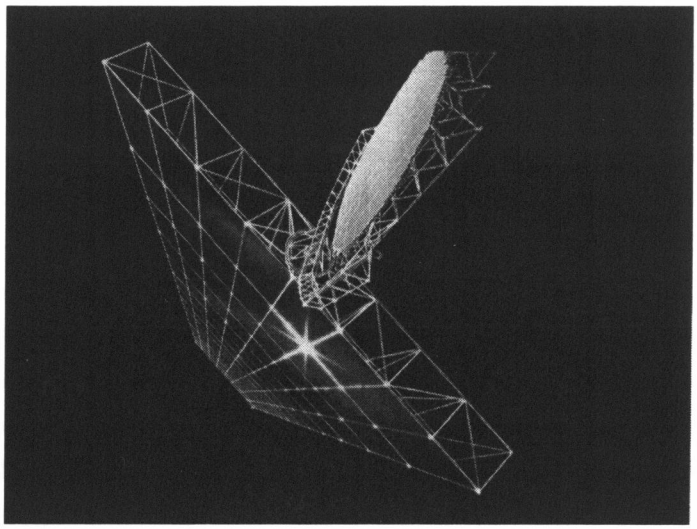

Figure 1.12: SPS NASA reference system [31].

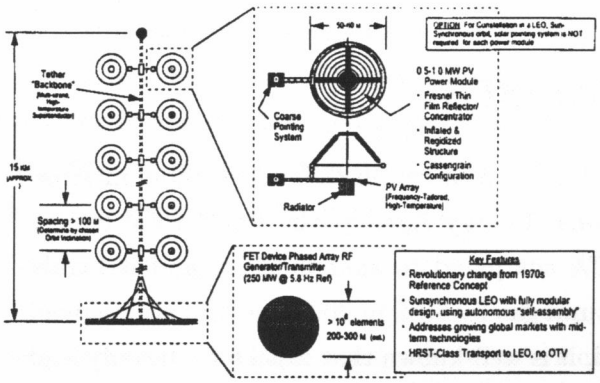

Figure 1.13: "Sun Tower" concept [33].

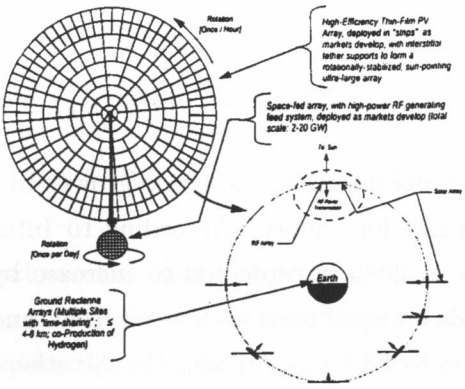

Figure 1.14: "Solar Disc" concept [33].

and Space Agency (NASA) [32]. Fig. 1.12 shows the SPS NASA reference system [31]. The SPS reference system mainly consists of the solar panels with the size of 5km×10km and the transmitting system with the diameter of 1km, and it weighs 50,000 tons. It is put into the geostationary orbit (GEO) and generates an enormous electric power of 10GW by solar photovoltaic cells. The electric power is converted into microwave power in the transmitting system, and the power is transmitted from the transmitting system in space to the receiving site on the Earth. The DC power on the receiving site is estimated to be 5GW, therefore the overall DC to DC efficiency is estimated to be about 50 %.

After the cease of the SPS studies in the United States in 1980's, NASA reviewed national and international studies on SPS in the program "Fresh Look Study [33]" in 1995-1997. The Fresh Look Study examined about 30 SPS concepts. The "Sun Tower" concept, depicted in Fig. 1.13 and the "Solar Disc" concept, depicted in Fig. 1.14, are the famous SPS concepts

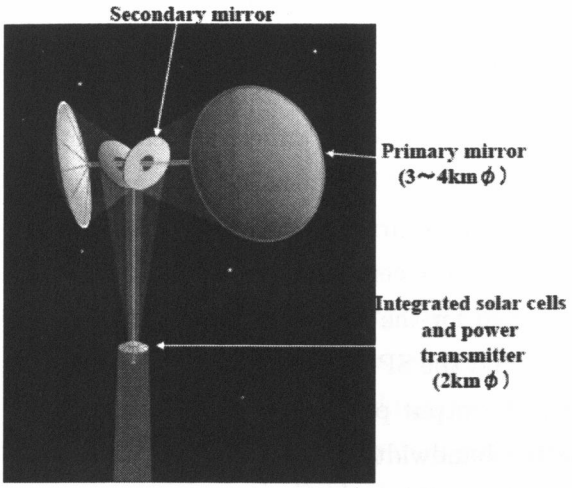

Figure 1.15: "Mirror-type" SPS concept – 2001 NASDA Reference System – [35].

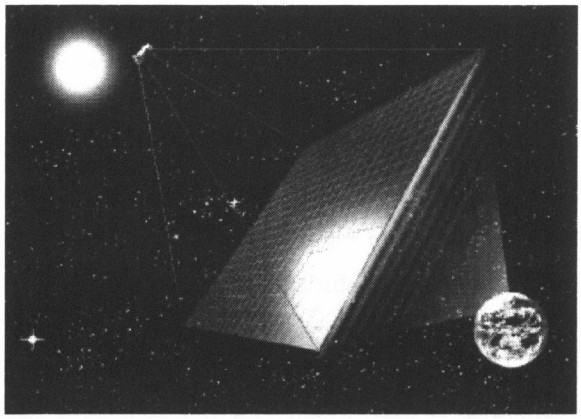

Figure 1.16: "Tether-type" SPS concept [36,37].

discussed in the Fresh Look Study. The Sun Tower, whose appearance is like a tree, is put into orbit at an altitude of 1000km and generates an electric power of 100-400MW. The Solar Disc is put into the GEO and generates an electric power of 1-10GW.

In Europe, the ACT (Advanced Concept Team) in the ESA (European Space Agency) has conducted a three-phased program since 2003 [34]. The ACT is conducting the first phase, the Validation Phase, which focuses on a comparison of space solar power plant with comparable terrestrial solutions on the one hand, and the assessment of the potential of the SPS for space exploration and space application on the other.

As stated above, lots of SPS studies have being conducted in several countries and groups. Especially, Japan has been showing energetic SPS activities in working committees, and experimental SPS concepts and 1GW-class commercial SPS concepts has been developed. The recent 1GW-class SPS concepts are classified into two types: a "mirror-type" SPS concept and a "tether-type" SPS concept. Fig. 1.15 and Fig. 1.16 show artist conceptions of the "mirror-type" SPS named "2001 NASDA Reference System" developed by the working group of the Japan Aerospace Exploration Agency (JAXA) [35], and the "tether-type" SPS developed by the working group of Institute for Unmanned Space Experiment Free Flyer (USEF) [36, 37], respectively.

The carrier frequency of almost all the SPS systems is designed to be in the ISM band of 2.45GHz or 5.8GHz. This is because microwave hardly suffers the ionospheric reflection and the atmosphere absorption in the frequency band from 1GHz to 10GHz. Therefore, the carrier frequency of almost all the WPT systems described in Sec. 1.2 is also designed to be in the ISM bands of 2.45GHz or 5.8GHz, although it has not been allocated for the WPT the and SPS yet.

1.4 Phase-Controlled Magnetron (PCM)

In the case of a SPS, microwave energy generated from a transmitting system must be efficiently and accurately focused on a receiving site with fast response, otherwise leaked microwave energy will not only cause power loss of the overall WPT system but also interfere in other communication systems severely. Therefore, a phased array system with enormous numbers of antenna elements, which is adopted in all of the recent SPS concepts, is one of the most essential techniques to be studied and developed for the SPS transmitting system.

Advantages of a magnetron for the use of the WPT and the SPS include its low cost, high DC-RF conversion efficiency (more than 70%) and high output power. On the other hand, a magnetron is very noisy and it has a wide oscillating bandwidth. In particular, the wide oscillating bandwidth is a significant disadvantage to the realization of a phased array with a phase control mechanism, which is indispensable for the SPS that handles an extremely large amount of power. A Phase-Controlled-Magnetron (PCM) has been developed in order to overcome the problem.

A basic configuration of the PCM is shown in Fig 1.17 [38]. The PCM is basically implemented in a phase locking of a magnetron in a phase of a reference signal whose frequency is necessary to be set in the frequency band of a magnetron. In order to realize both the frequency locking and the phase locking, an injection locking method, a method of the frequency locking by injecting the reference signal into an oscillator, is commonly used. The basic theory of the injection locking method was developed by Adler [39], and the following equation is well-known as Adler's equation;

$$\frac{\Delta f}{f} = \frac{2}{Q_{\mathrm{E}}}\sqrt{\frac{P_{\mathrm{in}}}{P_{\mathrm{out}}}}, \tag{1.6}$$

where Δf is the locking bandwidth, f is the center frequency of the oscillation, P_{in} is the RF input (injected) power, P_{out} is the RF output power, and Q_{E} is the external Q factor of the oscillator. When the frequency of the oscillator is locked in that of the reference signal, the

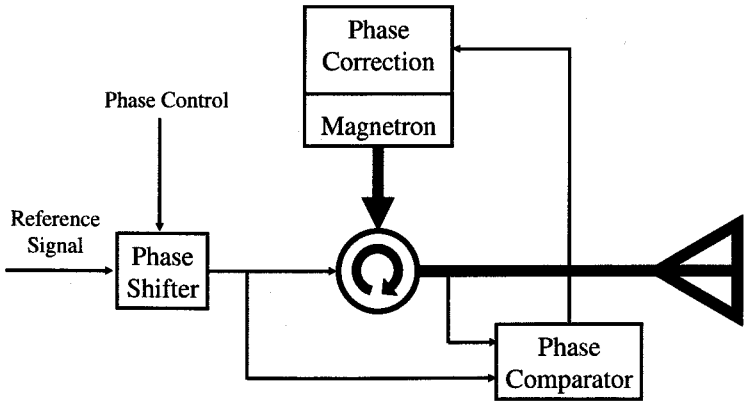

Figure 1.17: Basic configuration of a Phase-Controlled Magnetron (PCM) [38].

phase difference θ between the oscillator and the reference signal is also derived by Adler;

$$\theta = \sin^{-1} \frac{\Delta f' Q_E}{f\sqrt{P_{in}/P_{out}}}, \tag{1.7}$$

here $\Delta f'$ is the difference between the free-running frequency of the oscillator and the frequency of the reference signal.

Note that P_{in}/P_{out} is required to be large in order to lock the frequency and the phase of the oscillator as Δf becomes large, as expressed in Eq. (1.6). In the case of a cooker-type CW magnetron, the output power is several hundreds of watts, hence, the frequency and phase locking only by the injection locking method becomes difficult for practical use when the free-running frequency of a magnetron is away from the reference signal. Therefore, in order to cope flexibly with the individual difference of the free-running frequency of the magnetron, a combination of the injection locking method and a frequency control is commonly used. The frequency control is conducted by tuning the external magnetic field of the magnetron, or the anode current of the magnetron, or the output load impedance. By reducing the frequency difference between the magnetron and the reference signal close to zero with the frequency control method, large injected power is not necessary to lock the frequency and the phase of the magnetron.

A PCM has first been developed by Brown [40,41]. The PCM was realized by controlling the external magnetic field with a "buck boost" coil. A PCM by tuning the output load impedance has been developed in the University of Alaska Fairbanks [42]. The PCM was realized by a mechanical control system of the output load impedance with a servomotor.

Our research group in Kyoto University has also been developing a PCM by controlling the anode current of the magnetron [12,43–45]. In our PCM, a Phase-Locked-Loop (PLL) technique has been newly adopted. By a combination of the injection locking method and the PLL technique, both the frequency and the phase of our PCM can be automatically locked to the reference signal. Moreover, phases of multiple PCMs can be standardized by realizing $\theta = 0$ in Eq. (1.7) for each PCM. Owing to the accomplishment of the PCM, the experimental equipments with a phased array using PCMs at 2.45GHz and 5.8GHz were developed, which are named SPORTS (Space POwer Radio Transmission System) 2.45 shown in Fig. 1.18, and SPORTS5.8 shown in Fig. 1.19, respectively [46]. SPORTS2.45 includes 12 PCMs and generates microwave power of about 3.6kW. The microwave power beam is controlled by either of antenna systems; 12 horn antennas which are directly hooked up to 12 PCMs, or 96 dipole antenna elements which are hooked up to 12 PCMs via 8-ways power dividers. SPORTS5.8 includes 9 PCMs, which install a newly-developed 5.8GHz magnetron by Panasonic Semiconductor Discrete Devices Co., Ltd. and generates microwave power of about 1.26kW.

A light microwave power transmitter at 5.8GHz named COMET (COmpact Microwave Energy Transmitter) has been also developed by our research group [47,48]. The size of the COMET is only 310mm in diameter and 99mm in height, and the weight is less than 7kg.

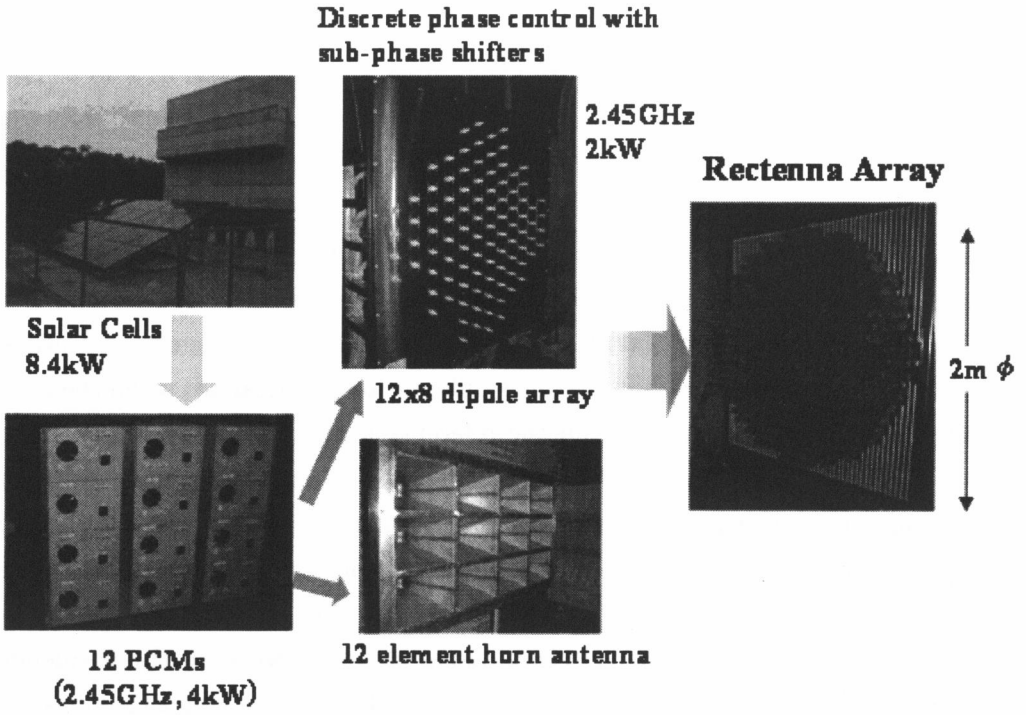

Figure 1.18: SPORTS2.45 [46].

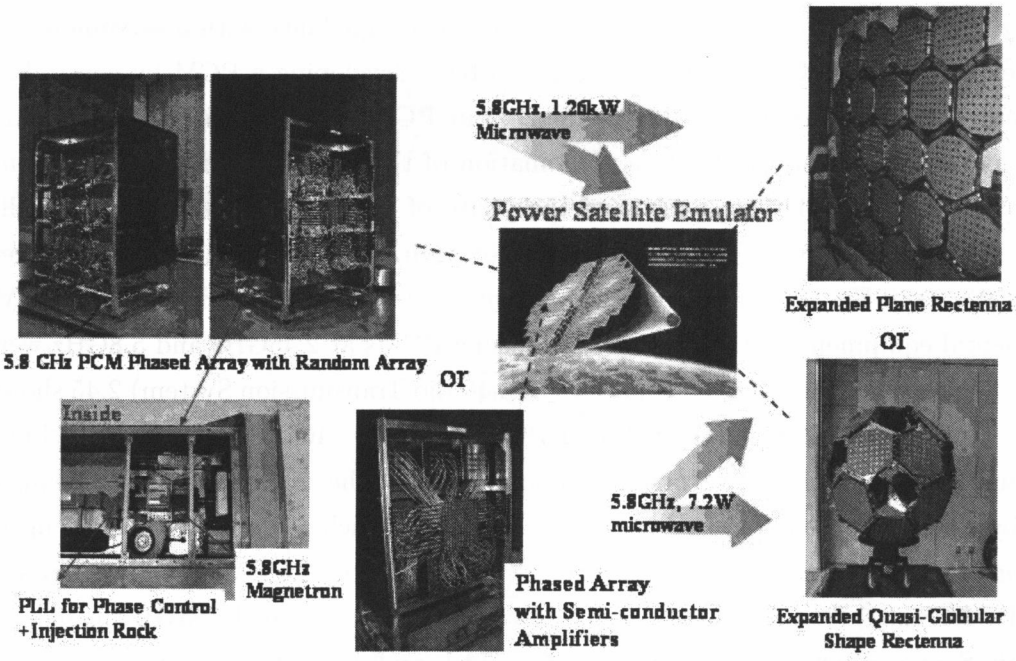

Figure 1.19: SPORTS5.8 [46].

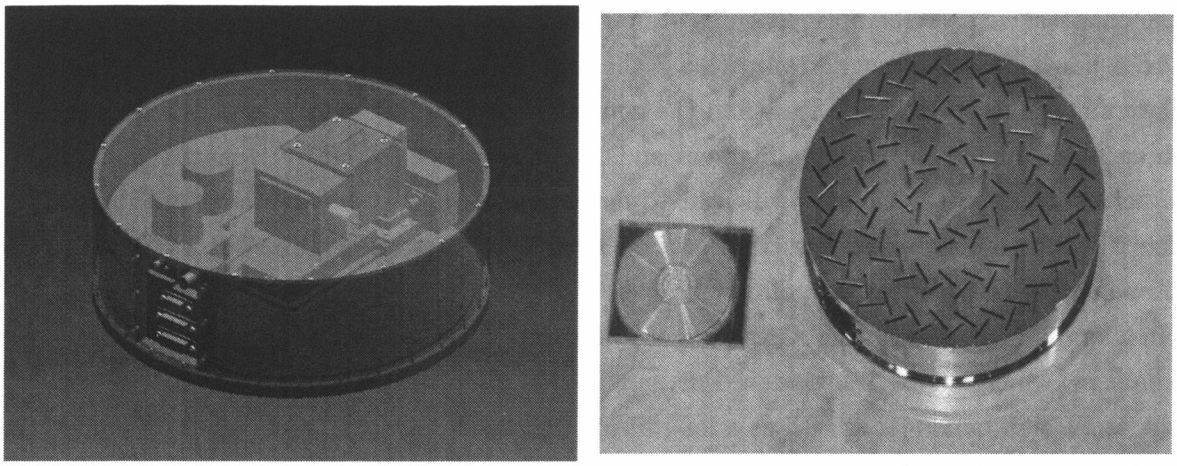

Figure 1.20: COMET [47,48].

Moreover, we succeeded to develop a Phase-and-Amplitude-Controlled Magnetron (PACM) by tuning both the anode current and the external magnetic field simultaneously [48–50].

1.5 Contribution of the present study

This thesis is devoted to a study on noise features of a magnetron and low noise WPT, in order to develop both a magnetron and a WPT system which are compatible with other radio applications.

In Chapter 2, we describe experimental measurements of electron emission from the cathode filament of a magnetron. A feature of the present study is that experimental measurements are conducted with three-dimensional aspects, which has not been treated in many previous studies on a magnetron. We conducted the experimental measurements of the anode current with axially-segmented anode blocks. We also conducted the experimental measurements of the filament temperature of a magnetron with a hole in the anode block. These experimental results play important roles in discussing generation mechanisms of noises from a magnetron, and designing a new type of a magnetron in the subsequent chapters.

In Chapter 3, we conducted a time domain analysis of magnetron noises for the purpose of clarifying generation mechanisms of spurious noises from a magnetron. We found out, from experimental results, that noises could be classified into five types. We also discussed spurious noise sources according to the classified noise types. The achievement in this chapter will contribute to dealing with these classified noises independently for development of a low noise magnetron, because the generating mechanisms of the categorized noises are likely to be different from each other.

In Chapter 4, we describe newly-designed low noise magnetrons. In the first part of the chapter, we conducted experimental measurements on the relationships between noise levels and the interaction space, and between noise levels and the anode voltage. In the latter part

of the chapter, we describe noise features of magnetrons with cathode shields. We found out that our newly-designed magnetron with a cathode shield only on the high voltage input side radiated spurious noises much less than the conventional oven magnetron and a magnetron with cathode shields on both the filament ends, which was suggested by Kohsaka *et al* [5]. The achievement in the chapter will lead to development of a future low noise magnetron which will contribute to cost reduction of a microwave oven by uninstalling filter circuits as well as EMC with other radio applications.

In Chapter 5, we describe noise features of a filament-off magnetron. The internal feedback mechanism, which has been introduced as an effective way for a quiet magnetron operation in the oscillation band [41] as well as a long life of the cathode [38,41], most effectively takes place by turning off the filament current during the oscillation of a magnetron. We found out that turning off the filament current is a significantly effective method for a magnetron not only to make the oscillation bandwidth narrower but also reduce the radiation noise levels in high frequency bands and the line noise levels in low frequency bands, when the magnetron is operated by a DC stabilized power supply. These achievements will contribute greatly to realization of low noise WPT systems. Especially, the improvement of the oscillation bandwidth has led to the development of a PCM described in Sec. 1.4.

In Chapter 6, we summarize the present study and give conclusions achieved by the present experimental measurements. Finally, we give suggestions for future researches and developments of a low noise magnetron and a low noise WPT system.

Chapter 2

Measurements of Electron Emission from Magnetron Cathode

2.1 Introduction

In this chapter, we describe experimental measurements of electron emission from the cathode filament of a magnetron. The cathode filament of the magnetron for a microwave oven is directly heated by an AC power supply for the purpose of supplying electrons necessary to maintain the oscillation in the form of thermal electron emission. The oscillation usually stops without this electron supply. On the other hand, either reducing or cutting off the filament current after the oscillation is known as an effective method for a magnetron to prevent the cathode from its short life due to unnecessary heating [38]. Moreover, Brown has also introduced this technique in order to suppress spurious noises around the carrier frequency band [41, 51]. This improvement is due to the "internal feedback mechanism", which we describe in detail in Chapter 5.

A feature of the present study is that experimental measurements are conducted with three-dimensional aspects. Many previous studies on analysis of a magneton has been discussed with two-dimensional aspects and the motion of electrons in the axial direction has been omitted. However, the two-dimensional aspects are not approved on both end sides of a magnetron, because it has a much more complex structure and the electromagnetic field. For example, there is the axial electrostatic field as well as the radial one on both end sides due to the existence of end hats, and the magnetic field lines are neither constant nor perfectly parallel to the axial direction. Therefore, some experimental measurements and discussions in the present chapter are conducted from the three-dimensional viewpoint.

In Sec. 2.2, we describe measurements of the anode current. The measurements are achieved by a magnetron with axially-segmented anode blocks. First, we measure the anode current of a cylindrical diode when the external magnetic field is not applied. Then, we measure the anode current of a magnetron. From experimental results and theoretical equations,

we discuss motion of an electron in a cylindrical diode and a magnetron analytically.

In Sec. 2.3, we describe measurements of the filament temperature. The measurements are achieved by a magnetron whose anode has a hole to see through the cathode filament directly. Two experimental measurements of the filament temperature are described. The former is measurements of the filament temperature at the center of the cathode in order to investigate the relationship between the filament current and the filament temperature when we take the anode current as a parameter. The latter is measurements of the axial distribution of the filament temperature in order to investigate the axial distribution of electron emission.

These measurements were also conducted as parts of necessary data for researching generation mechanisms of noises from a magnetron in the subsequent chapters.

2.2 Experimental measurements of the anode current with axially-segmented anode blocks

2.2.1 Configurations of a magnetron with axially-segmented anode blocks

A photo and a schematic view of a magnetron with axially-segmented anode blocks are shown on the left-hand side and the right-hand side of Fig. 2.1, respectively. The axially-segmented anode is formerly manufactured as a commercial magnetron, and it is processed and axially separated into five pieces: the outer sheath on the high voltage (HV) input side (Outer sheath (I)), the anode block on the HV input side (Anode (I)), the anode block on the center (Anode (C)), the anode block on the RF output side (Anode (O)), and the outer sheath on the RF output side (Outer sheath (O)), from above in Fig. 2.1. Each anode block is insulated from the adjacent anode blocks with a ceramic plate in order to investigate the amount of current flowing in the anode block.

With respect to the external magnetic field, we examine two cases; one is a cylindrical diode case when the external magnetic field is not applied, and the other is a magnetron case when the external magnetic field of 0.11T is applied. In the cylindrical diode case, electrons emitted from the cathode are considered to move straightforward to the anode only with the radial velocity component. Hence, the axial distribution of electron emission is roughly estimated by the measurement of the anode current flowing in each anode block. In the magnetron case, the relative amounts of the anode current flowing in the anode blocks are compared to those in the cylindrical diode case.

2.2.2 Measurement system

Fig. 2.2 shows a schematic of a measurement system for obtaining the anode current with the axially-segmented anode blocks. The magnetron is installed in a vacuum chamber to evacuate. The pressure in the chamber varies from 4.8×10^{-3}Pa before heating the filament, to 3.6×10^{-2}Pa after the measurements. Each anode block is connected to a resistance of 1Ω

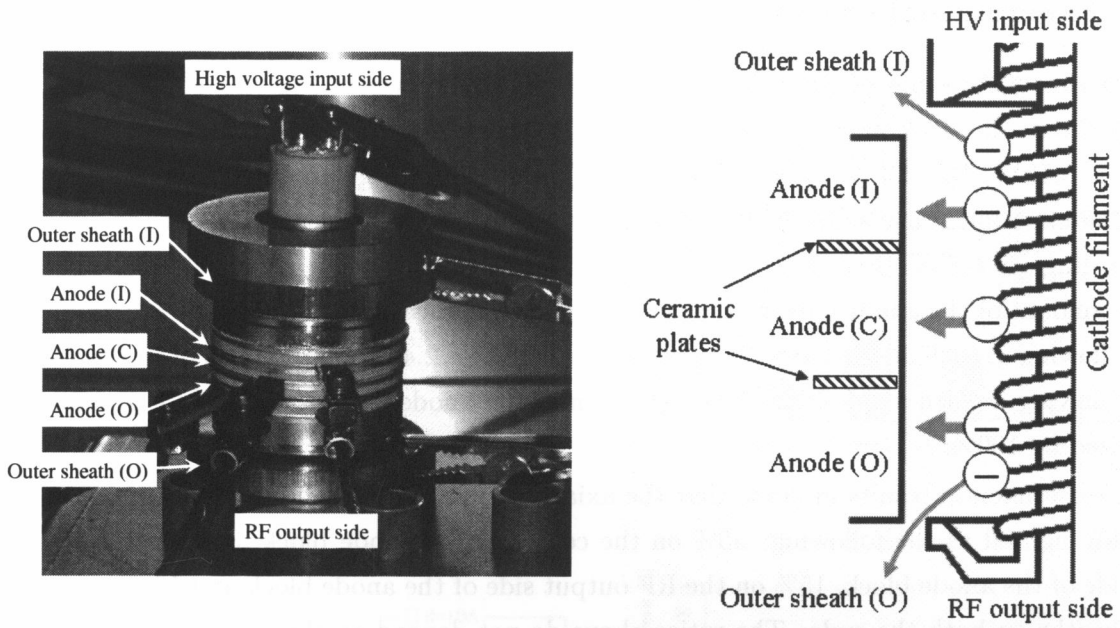

Figure 2.1: Photo (left) and schematic view (right) of a magnetron with axially-segmented magnetron anode blocks.

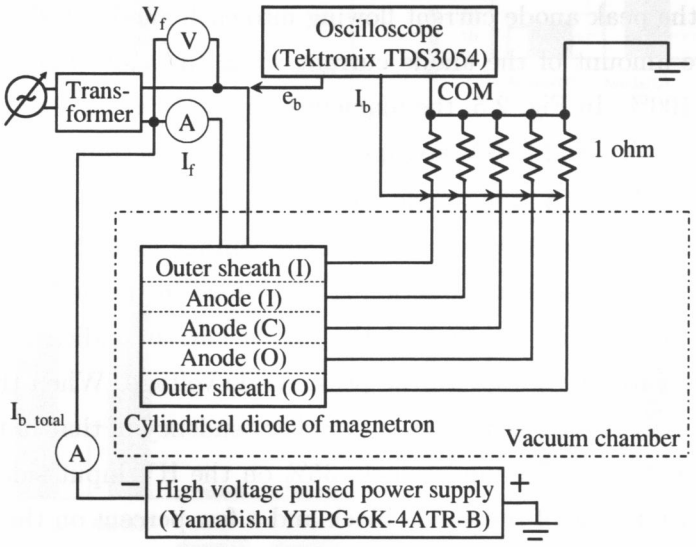

Figure 2.2: Schematic of a measurement system for obtaining the anode current with axially-segmented anode blocks.

outside of the vacuum chamber, and the anode current flowing in each anode block is obtained by measuring the voltage of each resistance with an oscilloscope (Tektronix TDS3054). In the magnetron case, the Outer sheath (O) is electrically connected to the Outer sheath (I) for convenience of setting. A high voltage pulsed power supply (Yamabishi YHPG-6K-4ATR-B, pulse frequency: 50Hz, duty ratio: 0.5) is used for an operation of the magnetron in order to prevent it from overheating.

2.2.3 Experimental results

The experimental results of the cylindrical diode case are shown in Fig. 2.3 and Fig. 2.4. Fig. 2.3 shows the peak anode current observed by the oscilloscope when the peak anode voltage is 0.5kV (Fig. 2.3 (a)), 1kV (Fig. 2.3 (b)) and 1.5kV (Fig. 2.3 (c)). Also, Fig. 2.4 shows the experimental results of the relative amount of electron emission when the peak anode voltage is 0.5kV (Fig. 2.4 (a)), 1kV (Fig. 2.4 (b)) and 1.5kV (Fig. 2.4 (c)). The relative amount of the anode current is calculated from the measurement data of each anode current flowing in each anode block. The vertical axis in Fig. 2.4 shows the ratio of the anode current flowing in each anode block when the sum of the anode current values in Fig. 2.3 is normalized by 100%.

The experimental results indicate that the axial distribution of the anode current values is roughly figured as the following: 45% on the center of the anode block, 30% on the HV input side of the anode block, 15% on the RF output side of the anode block and 10% on the outer sheaths on both the ends. The ratios above do not depend on the anode voltage and the filament current.

Fig. 2.5 shows the experimental results of the magnetron case. The left figure shows the experimental results of the peak anode current flowing into each anode blocks, and the right figure shows the relative amount of the anode current when the sum of the anode current values is normalized by 100%. In Fig. 2.5, the filament current is fixed at 10A, and the peak anode voltages of 0.9kV, 3.0kV and 5.0kV are applied to the magnetron.

From the left figure of Fig. 2.5, the anode current hardly flows when the peak anode voltage is 0.9kV, then it suddenly flows when the anode voltage exceeds a threshold value, which is determined by the Hull's cutoff equation [1] described in the next subsection. The experimental results of the relative amount of the anode current indicate that the axial distribution of the anode current varies with the peak anode voltage. When the peak anode voltage is 5.0kV, the axial distribution denotes the similar tendency of that in the cylindrical diode case: 50% on the center of the anode block, 35% on the HV input side of the anode block, 15% on the RF output side of the anode block and a few percent on the outer sheaths on both the ends. As the peak anode voltage reduces, the relative amount of the anode current shifts from the HV input side to the RF output side.

2.2.4 Discussions

Child-Langmuir law in a cylindrical diode

Here we discuss electron motion in a cylindrical diode analytically in order to investigate the behavior of electrons in the cylindrical diode.

In the case of an infinitely long cylindrical diode as shown in Fig. 2.6, the one-dimensional Poisson's equation, the energy conservation equation, and the equation of continuity in the

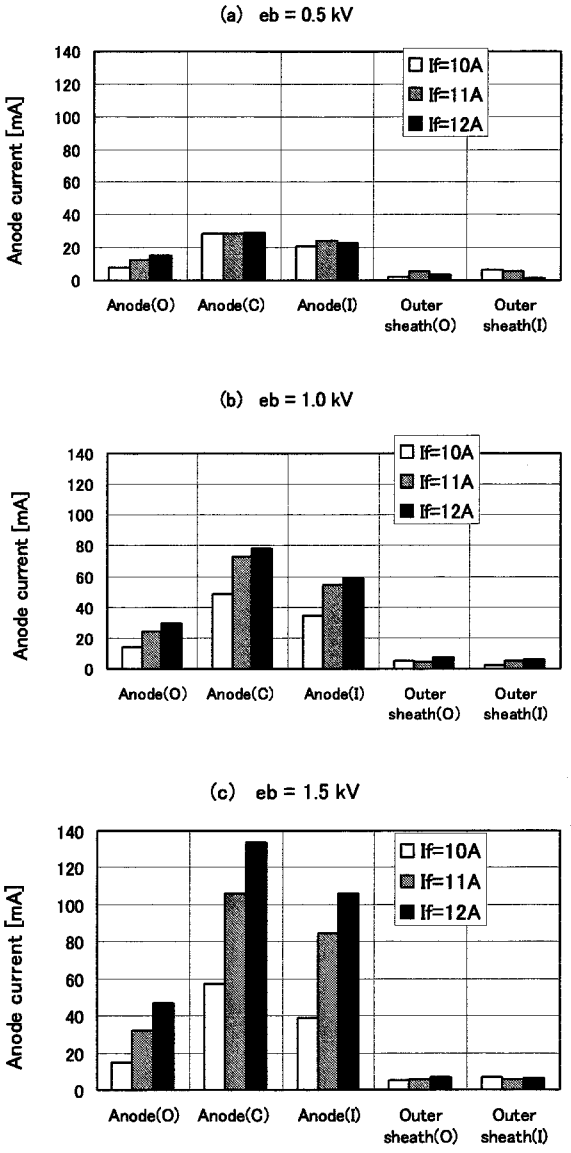

Figure 2.3: Experimental results of the anode current flowing in each axially-segmented anode block in the cylindrical diode case when e_b is (a) 0.5kV, (b) 1.0kV and (c) 1.5kV. e_b: peak anode voltage, and I_f: filament current.

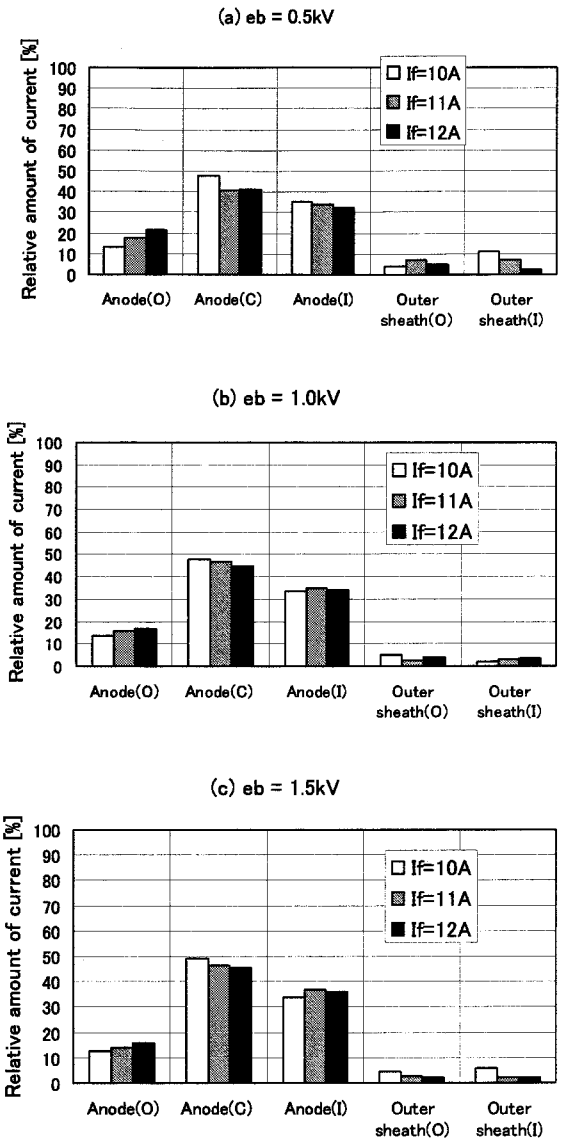

Figure 2.4: Experimental results of the relative amount of the anode current flowing in each axially-segmented anode block in the cylindrical diode case when e_b is (a) 0.5kV, (b) 1.0kV and (c) 1.5kV. e_b: peak anode voltage, and I_f: filament current.

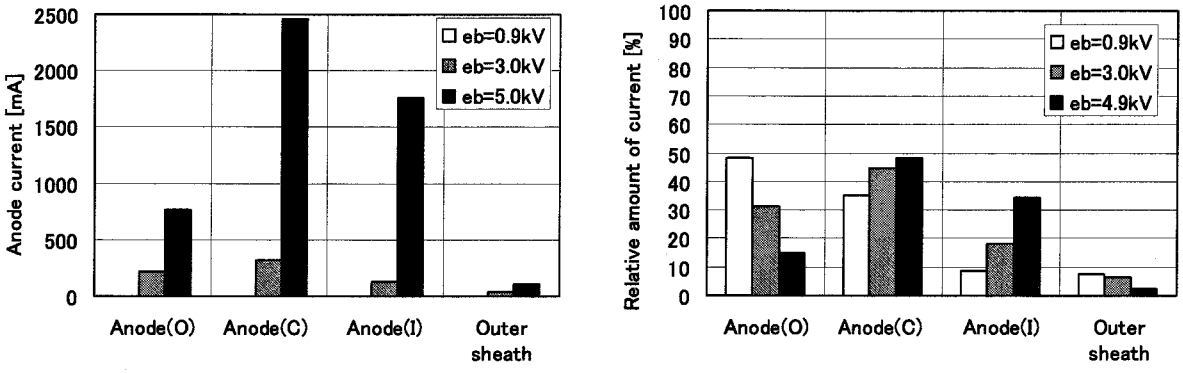

Figure 2.5: Experimental results of the anode current (left) and the relative amount of anode current (right) flowing in each axially-segmented anode block at a filament current I_f of 10A in the magnetron case. e_b: peak anode voltage.

cylindrical coordinates are expressed in the followings:

$$\frac{1}{r}\frac{d}{dr}\left(r\frac{d\phi(r)}{dr}\right) = -\frac{\rho}{\varepsilon_0}, \tag{2.1}$$

$$\frac{1}{2}mv^2 = eV, \tag{2.2}$$

$$J(r) = -\rho v, \tag{2.3}$$

respectively, where $\phi(r)$ is the potential at a radius of r, ρ is the charge density, ε_0 is the dielectric constant in vacuum, m is the electron mass, e is the electron charge, v is the electron velocity, and $J(r)$ represents the current density on a cylindrical plane at a radius of r. The negative sign in the right-hand side of Eq. (2.3) means that the current flow is opposite to the direction of the electron motion. When I is defined as the current per axial unit length,

$$I = 2\pi r J(r) = -2\pi r\rho v = \text{const.} \tag{2.4}$$

From Eq. (2.1), Eq. (2.2), Eq. (2.3) and Eq. (2.4),

$$\frac{d}{dr}\left(r\frac{dV}{dr}\right) = \frac{I}{2\pi\varepsilon_0}\sqrt{\frac{m}{2e}}V^{-\frac{1}{2}}. \tag{2.5}$$

Eq (2.5) can not be directly solved. However, in the case of parallel plate electrodes, the Child-Langmuir law is derived by conducting the same process;

$$I = \frac{4\varepsilon_0}{9}\sqrt{\frac{2e}{m}}\frac{V^{\frac{3}{2}}}{d^2}, \tag{2.6}$$

where d is the gap between the anode and the cathode of the parallel plate electrodes. Hence,

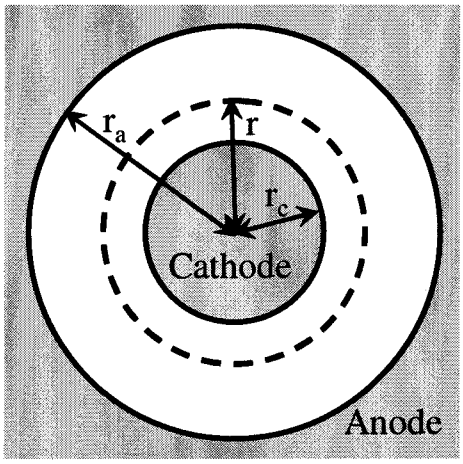

Figure 2.6: Cross-section view of a cylindrical diode. r_a: anode radius, r_c: cathode radius.

referring to Eq. (2.6), the final solution takes the following expression including a series;

$$
\begin{aligned}
I &= \frac{8\pi\varepsilon_0}{9}\sqrt{\frac{2e}{m}}\frac{V^{\frac{3}{2}}}{r_a\beta_a^2}, \qquad (2.7)\\
\beta &= \ln\left(\frac{r}{r_c}\right) - \frac{2}{5}\left[\ln\left(\frac{r}{r_c}\right)\right]^2 + \frac{11}{120}\left[\ln\left(\frac{r}{r_c}\right)\right]^3 \\
&\quad -\frac{47}{3300}\left[\ln\left(\frac{r}{r_c}\right)\right]^4 + \cdots, \\
\beta_a &= \beta|_{r=r_a},
\end{aligned}
$$

where r_a and r_c is the radii of the anode and the cathode, respectively [52, 53].

The curves in Fig 2.7 shows the relationship between the three-halves power of the anode voltage in the horizontal axis and the current flowing in each anode blocks from the experimental results in Fig 2.3 in the vertical axis. The curves at the filament current of 12A in Fig 2.3 show straight lines, therefore, they quite meet the Child-Langmuir's law in the cylindrical coordinates expressed in Eq. (2.7), and the cylindrical diode is operated in the region of the space charge limitation. On the other hand, the curves at the filament current of 10A in Fig 2.3 diverge gradually from the Child-Langmuir's law and finally the anode current is independent of the anode voltage. Therefore, in these regions, the cylindrical diode is operated in the region of the temperature limitation, and the anode current is determined only by the filament temperature.

As described above, the experimental results of the cylindrical diode case quite meet the fundamental laws on vacuum electronics.

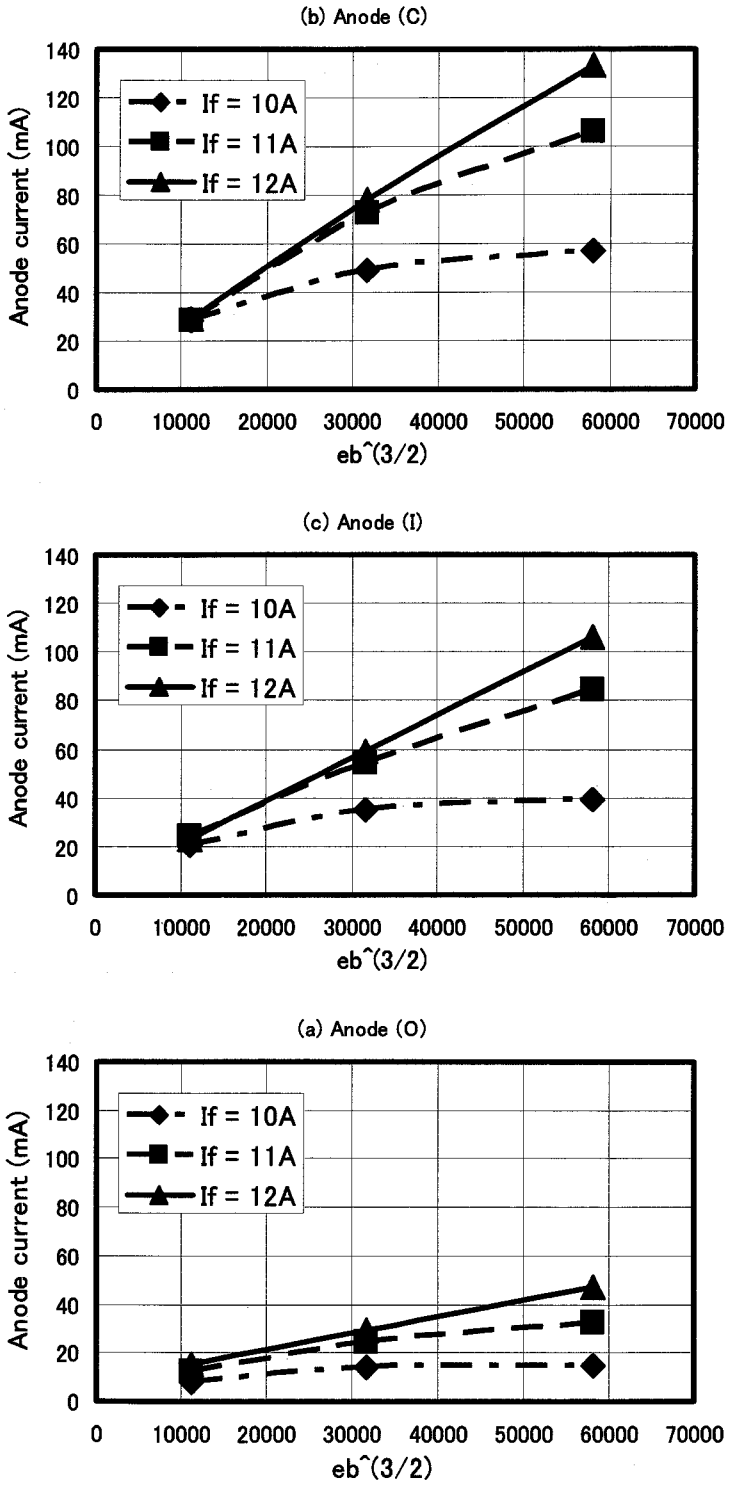

Figure 2.7: Three-halves power of the anode voltage vs. the current flowing in each anode blocks from the experimental results in Fig 2.3. (a): the center of the anode, (b): the HV input side, and (c): the RF output side. e_b: anode voltage, and I_f: filament current.

Electron motion in a cylindrical diode

The motion of a single electron in a cylindrical diode is expressed by Eq. (1.1) when $\boldsymbol{B} = 0$. Therefore,

$$m\frac{dr}{dt} = e\frac{d\phi(r)}{dr}. \tag{2.8}$$

From Eq. (2.8), the traveling time of the single electron from the cathode $r = r_c$ to the anode $r = r_a$ is solved by setting $dr/dt = 0, r = r_c$ when $t = 0$ and $\phi(r_a) = V$ at $r = r_a$;

$$t = (r_a - r_c)\sqrt{\frac{m}{2eV}}. \tag{2.9}$$

In the case of a magnetron 2M210M1F1, which we have used as the reference in this thesis, $r_a - r_c$=2.525mm, thus the traveling time t is equal to 1.10×10^{-10}s when the anode voltage V is 1.5kV.

Electron motion in a magnetron

Here we discuss electron motion in a magnetron analytically and compare the motion to that in a cylindrical diode.

When electrons are assumed to be uniformly distributed in a magnetron *i.e.* ρ = const., we integrate Eq. (2.1) by r, then

$$r\frac{\partial\phi(r)}{\partial r} = \frac{\rho}{2\varepsilon_0}r^2, \tag{2.10}$$

where the integration constant vanishes by assuming ρ has a large figure. This expedient assumption is commonly used because it helps us to solve the equation of motion Eq. (1.1) analytically, and its validity is supported by some experimental results [54]. Then, we integrate Eq. (2.10) and set the integration constants as $\phi(r_c) = 0$ and $\phi(r_a) = V$,

$$\phi(r) = \frac{r^2 - r_c^2}{r_a^2 - r_c^2}V. \tag{2.11}$$

With regard to the equation of motion, we can solve it by replacing the two-dimensional cylindrical coordinates by the coordinates on the complex plane, then $\boldsymbol{E}$ and $\boldsymbol{v}\times\boldsymbol{B}$ are expressed as the followings;

$$\boldsymbol{E} \Rightarrow -\frac{\partial\phi}{\partial x} - j\frac{\partial\phi}{\partial y} = -2e\frac{V}{r_a^2 - r_c^2}\xi, \tag{2.12}$$

$$\boldsymbol{v}\times\boldsymbol{B} \Rightarrow \left(-j\frac{\partial x}{\partial t} + \frac{\partial y}{\partial t}\right)B = -jeB\frac{d\xi}{dt}, \tag{2.13}$$

where $\xi = x + jy$ and B is the external magnetic field. From Eq. (2.11), Eq. (2.12) and Eq. (2.13), Eq. (1.1) is rewritten;

$$m\frac{d^2\xi}{dt^2} - jeB\frac{d\xi}{dt} - 2e\frac{V}{r_a^2 - r_c^2}\xi = 0. \tag{2.14}$$

Then, the solution of Eq. (2.14) is derived;

$$\xi = R_1 \exp(j\Omega_1 t) + R_2 \exp(j\Omega_2 t), \tag{2.15}$$

$$\text{where} \quad \Omega_{\frac{1}{2}} = \frac{eB}{2m} \pm \sqrt{\left(\frac{eB}{2m}\right)^2 - \frac{2e}{m}\frac{V}{r_a^2 - r_c^2}}, \tag{2.16}$$

$$R_1 = \frac{\Omega_2}{\Omega_2 - \Omega_1} r_c, \quad R_2 = \frac{\Omega_1}{\Omega_1 - \Omega_2} r_c. \tag{2.17}$$

Here $|\xi| = r_c$ and the initial velocity is 0 when $t = 0$, as the initial conditions. Therefore, the single electron in a magnetron has circular drift motion with a radius of $|R_2|$, and rotational motion with a radius of $|R_1|$ [54].

By numerical analysis, we depict the trajectory in Fig. 2.8. The left-hand figure and the right-hand figure show the trajectory of the single electron in a magnetron, and the time variation of the radial position of the electron, respectively, when the anode voltages are 1kV, 3kV and 5kV. The reference magnetron 2M210M1F1 is used for parameters to solve the trajectory, except that the intensity of the external magnetic field is 0.11T which is applied in the present measurements.

From Fig. 2.8, the electron does not reach the anode when the anode voltage is less than the threshold value which is determined by the Hull's cutoff equation [1]. The Hull's cutoff equation is given by Eq. (2.15), Eq. (2.16), Eq. (2.17) and the condition that an electron just reaches the anode. The last condition means the maximum radius of the electron trajectory is equal to the anode radius, *i.e.* $|R_1| + |R_2| = r_a$. Therefore, the Hull's cutoff equation expressed as the following;

$$eV = \frac{m}{8}\left(\frac{eB}{m}\right)^2 r_a^2 \left(1 - \frac{r_c^2}{r_a^2}\right)^2. \tag{2.18}$$

For the reference magnetron, the cutoff voltage is 4.17kV when B=0.11T, hence, an electron reaches the anode when the anode voltage is 5kV, and not when it is 1kV and 3kV, as shown in Fig. 2.8.

The traveling time t of the electron from the cathode to the anode is estimated to be 1.81×10^{-10}s at an anode voltage of 5kV from the curves on the right-hand side of Fig. 2.8. It is about 1.65 times as much as that at an anode voltage of 1.5kV in the cylindrical diode case. Because the trajectory of the electron is bended by the magnetic field, the traveling time in the magnetron case becomes longer than that in the cylindrical diode case.

At an anode voltage of 3kV, the electron dose not arrive at the anode theoretically and it takes 2.92×10^{-10}s to reach the closest point to the anode from Fig. 2.8. In fact, however, the anode current flows when the anode voltage is lower than the cutoff voltage, as shown in Fig. 2.5. This is because the formation of electron spokes assists electrons in reaching the anode in a magnetron at a lower anode voltage than the cutoff voltage. Then, the traveling time of the electron from the cathode to the anode will be much longer than 2.92×10^{-10}s since electrons arrive at the anode while rotating several times in the interaction space with the formation of the electron spokes.

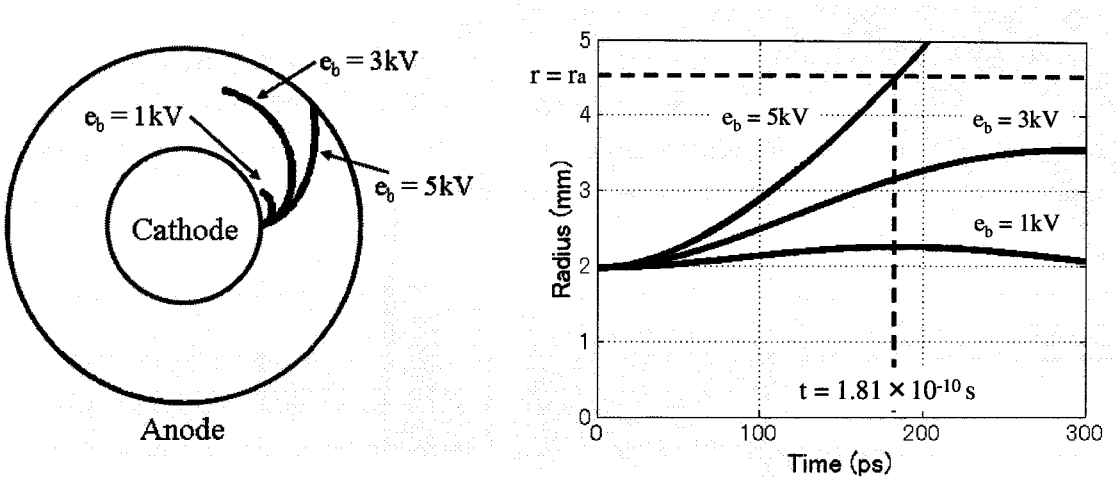

Figure 2.8: Trajectory of a single electron in a magneton (left) and time variation of the radial position of the electron (right). The reference magnetron model 2M210M1F1 is used for parameters to solve the trajectory.

Axial diffusive motion of electrons

We here discuss the effect of diffusive motion to the axial direction z. The electron motion to the axial direction is independent of B, thus it can be discussed in the case of both a cylindrical diode and a magnetron at the same time.

The axial velocity component of a single electron is provided by two reasons: one is because the initial velocities of thermal electrons have the axial component as well as the radial or azimuthal component, and the other is because electrons are diffused to the axial direction by the charge density gradient.

In the former case, we define $f_z(v_z)$ as the standardized distribution function of the number of thermal electrons moving to the axial direction with a velocity of v_z, $f_z(v_z)$ is given by the Maxwell's distribution;

$$f_z(v_z) = \frac{1}{N_{\text{total}}}\frac{dN}{dv_z} = \frac{v_z}{v_{\text{th}}^2}\exp\left(-\frac{v_z^2}{2v_{\text{th}}^2}\right), \qquad v_{\text{th}} = \sqrt{\frac{kT}{m}}, \tag{2.19}$$

where N is the number of electrons, N_{total} the total number of electrons, v_{th} is the thermal velocity of electrons and k is the Boltzmann constant [55]. For example, we assign T is 2000K to Eq. (2.19) from the experimental results of the filament temperature at the center of the cathode when I_b = 400mA and I_f = 10.5A, as described in the next section. Then, the thermal velocity v_{th}, which is the most probable value of $f_z(v_z)$, is equal to 1.74×10^5m/s. Since electrons continue in a state of uniform motion in the axial direction, the axial travel distance z_{th} by the thermal velocity from leaving the cathode to reaching to the anode is represented by $v_z t$, where t is the traveling time of the electron from anode to cathode. For example, the axial travel distance of a single electron with a velocity of v_{th} is calculated to be 1.91×10^{-5}m at an anode voltage of 1.5kV in the cylindrical diode case, and 3.15×10^{-5}m

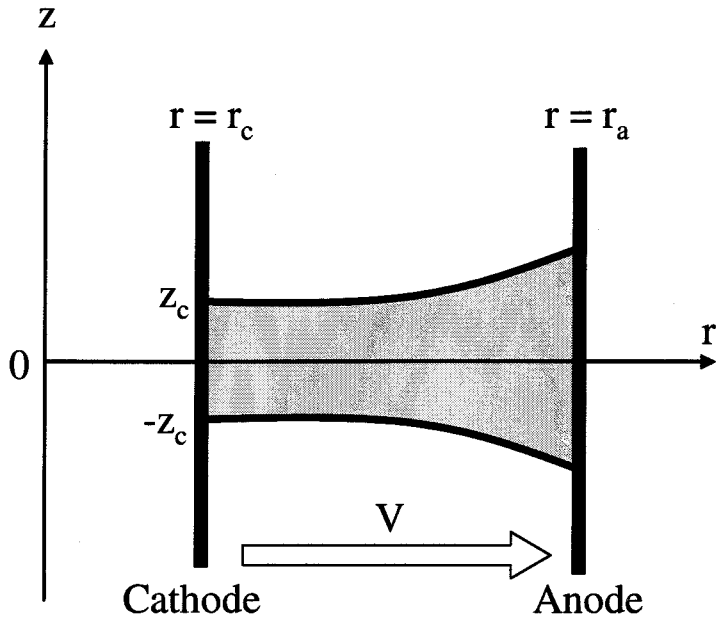

Figure 2.9: Diffusion of a beam in a cylindrical diode in the $r-z$ plane. r_a: anode radius, r_c: cathode radius, and V: anode voltage.

at an anode voltage of 5kV in the magnetron case. Therefore, diffusive motion by the initial velocities of thermal electrons can be neglected because the size of the magnetron we have experimented is the order of 10^{-3}m.

In the latter case, planar electron beam diffusion shown in Fig. 2.9 is used to analyze in the cylindrical diode case. When the coordinate axes in the $r-z$ plane are defined as shown in Fig. 2.9, the envelope curve of the planar beam is expressed in the following;

$$z = \left(\frac{I_0}{V^{\frac{3}{2}}} \frac{\sqrt{m/e}}{2^{\frac{7}{2}} \varepsilon_0} \right) (r - r_c)^2 + z_0, \tag{2.20}$$

where I_0 is the current per unit length of the r direction [56]. For example, the current flowing in the center of the anode (Anode(C)) when $e_b = 1.5$kV and $I_f = 12$A was measured to be 133.6mA from the experimental results. Then, we approximate a segmented anode block by a prefect cylinder, the surface area of the Anode(C) is calculated to be 8.48×10^{-5}m^2. We assume that I_0 is uniform in the radial direction between the cathode and the anode, then, the diffusion length $(z - z_0)$ at the anode $r = r_a$ in the cylindrical diode case is calculated from Eq. (2.20) to be 4.12mm, which is the same order of the axial length of the magnetron.

In the magnetron case, we analogize the diffusion length from the discussion above. Since Eq. (2.20) is the square function of r, and the traveling time from the cathode to the anode is about 1.65 times as much as that in the cylindrical diode case, the diffusion length at an anode voltage of 5kV in the magnetron case is calculated to be $(1.65)^2\times4.12$mm=11.2mm, which is also comparable to or a little bit longer than the size of the magnetron.

From discussions above, it is found out that diffusive motion of an electron mainly takes place by the charge density gradient. In the cylindrical diode case, the diffusion length is comparable to its size. In fact, 10% of the total amount of the anode current flow in the outer sheaths on both the ends, although the end hats, attached to both the cathode filament ends, play a role in prevention of the electron flow into the outer sheath of the magnetron.

Discussions of the relative amount of the anode current in the magnetron case

The diffusion length in the magnetron case at an anode voltage of 5kV is comparable to that in the cylindrical case. This corresponds to the experimental results in Fig. 2.4 and Fig. 2.5, which show that both the axial distributions of the anode current are similar.

On the other hand, the relative amount of the anode current gradually shifts from the HV input side to the RF output side as the anode voltage reduces, from the experimental results in Fig. 2.5. This is caused by the diffusive motion due to the long traveling time.

Even if we assume that the traveling time from the cathode to the anode is 2.92×10^{-10}s in the magnetron case at an anode voltage of 3kV, the diffusion length will be at least $(2.92 \times 10^{-10}\text{s}/1.10 \times 10^{-10}\text{s})^2\times4.12\text{mm}=29.0\text{mm}$. Furthermore, the actual diffusive length will be much longer than 29.0mm since the traveling times is expected to be several times as much as 2.92×10^{-10}s. As we mentioned that the size of the magnetron is the order of 10^{-3}m, the charge density gradient has strong effect on the diffusive motion of electrons to the axial direction. Especially, in the magnetron case, it is predicted that electrons are more easily diffused to the axial direction from the center to the sides, or even to outer sheaths by the diffusive motion.

In conclusion, the diffusive motion in the magnetron case can not be neglected, and the variation of the relative amount of the anode current, as shown in Fig. 2.5, is attributed to the axial diffusive motion.

2.3 Experimental measurements of the filament temperature

2.3.1 Measurement system

A schematic of a measurement system for obtaining the filament temperature of a magnetron is shown in Fig. 2.10. The operating power supply for the magnetron is a commercially available DC stabilized power supply (Glassman PS/LT005R360-20). The magnetron is coupled to a waveguide, and the microwave output is connected to an almost-matched termination of a high-power dummy load of 2.5kW (Nihon Koshuha, WDL-0233E).

A photo of the magnetron for the filament temperature measurement is shown in Fig. 2.11. The structure of the magnetron is almost the same as the reference magnetron 2M210M1F1, except that it has a hole in the anode block. A crystal plate is tightly attached to the hole in order to keep the magnetron tube in vacuum, and the cathode filament can be directly seen

through the crystal plate. The filament temperature is measured with an optical pyrometer, and its measurement error is about ±100°C. Although the resonant condition of the present magnetron is somewhat different from the reference magnetron due to the hole on the anode, both the filament shape and the filament material in the present magnetron are identical to the reference magnetron. Therefore, this arrangement is sufficient for obtaining the relationship between the filament current and the filament temperature of a magnetron. The AC filament current and the DC anode current is measured with ampere meters. Also, the anode current and the anode voltage are observed with an oscilloscope (HP 54600B).

2.3.2 Experimental results of filament current vs. filament temperature

Fig. 2.12 shows the experimental results of the filament current I_f vs. the filament temperature curves. Fig. 2.12 indicates that the filament temperature increases as the anode current and the filament current increase.

Also, we measured the minimum filament temperature at which the magnetron can start the oscillation. When the magnetron is operated by a DC stabilized power supply, the minimum filament temperature for the oscillation was 1230°C. This means that the magnetron can not oscillate at all when the filament temperature is below 1230°C.

As shown in Fig. 2.12, the filament temperatures when the filament current is turned off during oscillation are 1660°C, 1630°C, 1590°C, and 1520°C at anode currents of 400mA, 300mA, 200mA, and 100mA, respectively. All of these values are higher than 1230°C, the minimum filament temperature for the oscillation. At the start-up, electrons are produced in the magnetron only by the thermionic emission. Therefore, the experimental results at

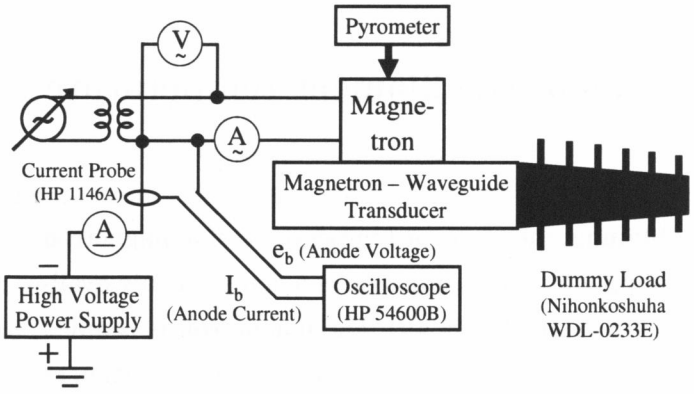

Figure 2.10: Schematic of a measurement system for obtaining the filament temperature of a magnetron.

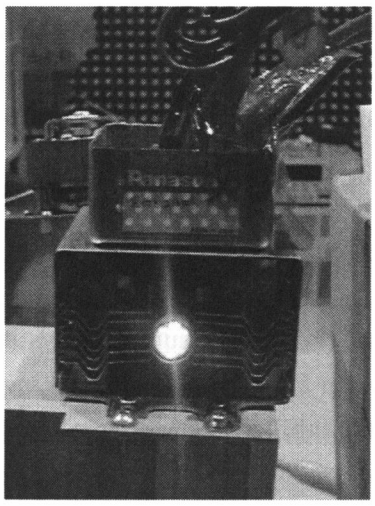

Figure 2.11: Photo of the magnetron for the measurements of the filament temperature. The light of the filament is seen through a crystal plate.

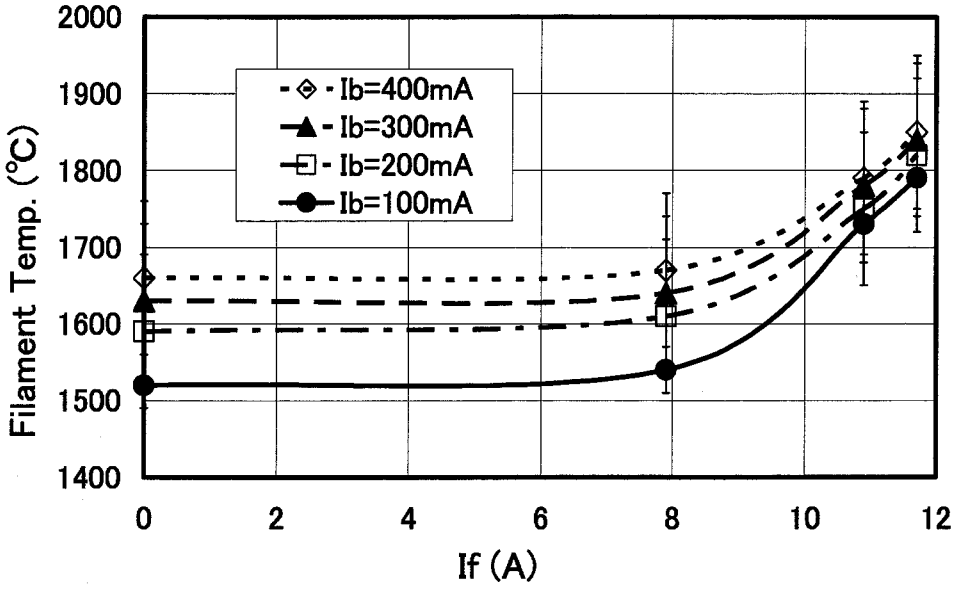

Figure 2.12: Filament current I_f vs. filament temperature. I_b: anode current.

I_f=0A mean that the filament temperature is high enough to emit thermal electrons from the cathode filament even when the filament current is turned off.

With regard to the cutoff of the filament current, Brown has mentioned "This temperature turned out to be the lowest temperature at which the thermionically emitting cathode can supply the needed anode current.", which is called the "internal feedback mechanism" [41]. Our experimental results in Fig. 2.12 explicitly supports his discussions in that the filament temperature was decreased by the reduction of the filament current.

2.3.3 Experimental results of axial distribution of the filament temperature

Fig. 2.13 shows the experimental results of the filament temperature in the axial direction. The horizontal axis shows the axial measurement points on the cathode filament: No. 1 is the end of the RF output side, No.4 is the center of the filament and No.7 is the end of the high voltage (HV) input side. The curves in Fig. 2.13 represent the filament temperatures in the preheating state (I_b = 0A, I_f = 10.5A), in the oscillating state (I_b = 400mA, I_f = 10.5A), and in the oscillating states with turning off the filament current (I_b = 400mA, I_f = 0A and I_b = 100mA, I_f = 0A).

Fig. 2.13 indicates that the filament temperature is the highest at the center, and that it is higher on the HV input side than on the RF output side.

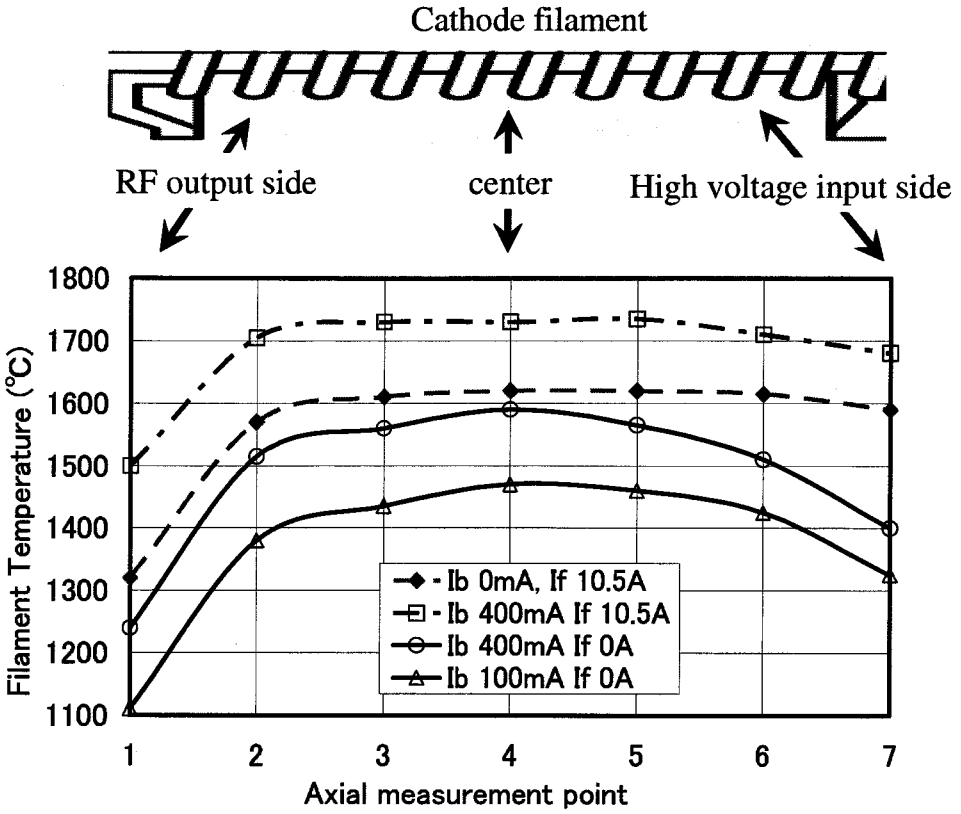

Figure 2.13: Axial distribution of the filament temperature. I_b: anode current, and I_f: filament current.

2.3.4 Discussions

Relationship between the filament temperature and the saturation current density

Now we discuss the experimental results by the Richardson-Dushman's equation [57], a well-known equation which relates to the saturation current density of the thermionic emission and the temperature of the emitting material;

$$I_{th} = SAT_K^2 \exp(-e\phi/kT_K), \tag{2.21}$$

where e is the electron charge, k is the Boltzmann constant, I_{th} is the saturation current of emission, S is the surface area, A is the thermionic emission constant, T_K is the temperature in Kelvin, and ϕ is the work function of the emitting material. For a microwave oven magnetron, the emitting material of the filament is a carburized thoriated tungsten (W_2C+Th), and its thermionic emission constant and work function are $0.97\times10^4 A/m^2/K^2$ and 2.18eV, respectively. Then, we define I_0 as the I_{th} when T_K is the minimum filament temperature for the oscillation, *i.e.* 1500K. Also, we define I_{th_ratio} as the ratio between I_{th} and I_0. Then,

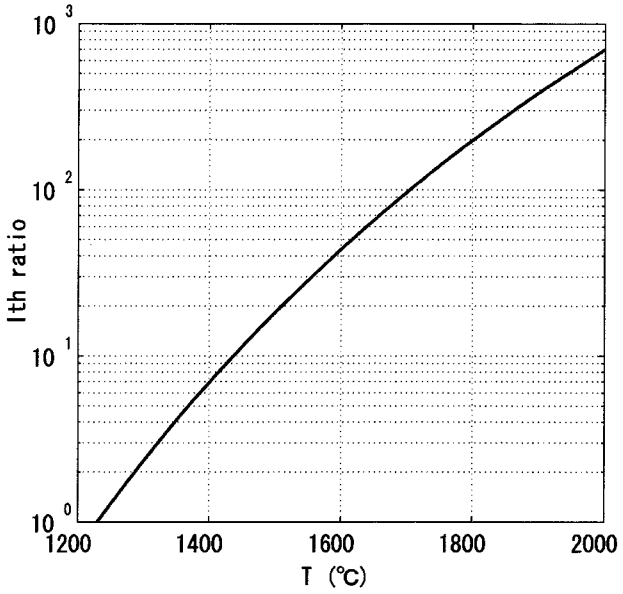

Figure 2.14: Curve of the temperature T vs. the ratio of saturated current $I_{\text{th\_ratio}}$. $I_{\text{th\_ratio}}$=1 when T=1230°C.

the following equation is derived;

$$I_{\text{th\_ratio}} \equiv \frac{I_{\text{th}}}{I_0} = \frac{T_{\text{K}}^2 \exp\{-e\phi/(kT_{\text{K}})\}}{(1500\ \text{K})^2 \exp[-e\phi/\{(1500\ \text{K})k\}]}. \tag{2.22}$$

Fig. 2.14 depicts the curve of temperature in Celsius vs. $I_{\text{th\_ratio}}$ derived from Eq. (2.22). For examples, we discuss the case that the anode current I_{b}=100mA and the filament current I_{f}=0A. The filament temperature in this case is obtained from Fig. 2.12; it is 1520°C. Thus, $I_{\text{th\_ratio}}$ obtained from Fig. 2.14 is equal to about 20. This means that the saturation current density is about 20 times as large as that of the state which the magnetron can barely oscillate.

Therefore, it is concluded that the filament has sufficient temperature to emit thermal electrons in order to sustain the oscillation even when the filament current is turned off. The reason why the filament temperature is still high even after turning off the filament current is because the filament suffers the back bombardment effects [38] and it is heated up by itself, although the secondary electron emission may also occur.

Axial distribution of the filament temperature

Fig. 2.13 shows that the filament temperatures of both the HV input side and the RF output side are lower than that of the center of the filament in all the states. This is because heat transmission from both the filament ends to the cathode end hats takes place. Especially, in the oscillating state with turning off the filament current, the filament temperatures of both the ends are relatively much lower than those in any other states. Therefore, thermal electrons are estimated to be less emitted from both the filament ends than that from the center.

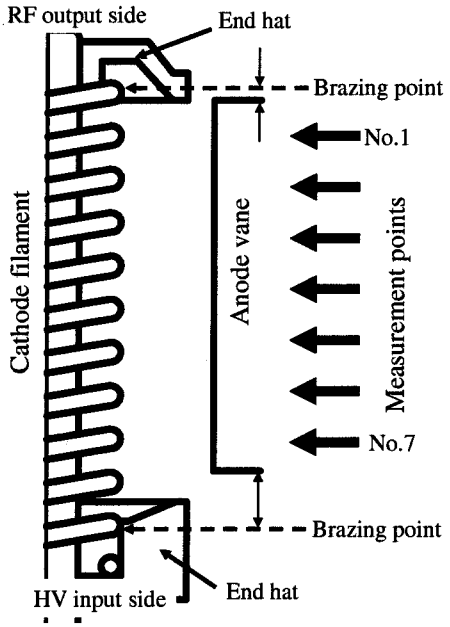

Figure 2.15: Brazing points between the cathode filament and the end hats.

Moreover, the filament temperature on the RF output side is measured to be lower than on the HV input side, whereas the axial distribution of the filament temperature is supposed to be symmetric. The experimental result that the axial distribution of the filament temperature is asymmetric is mainly attributed to both the structure of the magnetron and the brazing points between the cathode filament and the end hats, as shown in Fig. 2.15. The cathode filament is brazed to both the end hats, and the heat transmission takes place from the filament to both the end hats via the brazing points. When we view the filament from the anode vane as dose the optical pyrometer, the axial distance from the brazing point to the nearest measurement point on the RF output side is shorter than that on the HV input side. Hence, the filament temperature on the RF output side is measured to be lower than that on the HV input side, since the heat transmission takes place near the measurement points. Finally, the axial distribution of the filament temperature is originally symmetric; however, the measurement results show that the axial distribution is asymmetric because the center of the cathode filament is out of alignment axially from the center of the anode vane to the HV input side.

Due to the off-alignment of the cathode filament, thermal electrons are estimated to be much less emitted from the RF output side than from the HV input side. This tendency quite agrees with the measurement results of the relative amount of the anode current in the cylindrical case; the larger amount of electrons flew in the anode block on the HV input side than that on the RF output side, as described in Sec. 2.2.

Now we discuss the saturation current density again from Eq. (2.22) in the case of I_b = 100mA and I_f = 0A. Note that the filament temperature on the RF output side obtained

from Fig. 2.13 is 1110°C. It is lower than 1230°C, the minimum filament temperature for oscillation, and $I_{\text{th\_ratio}}$ obtained from Eq. (2.22) is about 0.14. Therefore, thermal electrons are emitted from the center of the cathode filament enough to maintain the oscillation of the magnetron; in contrast they are hardly emitted from the RF output side in this operating situation.

Besides, the axial position of the anode vanes of the reference magnetron is out of the center to the RF output side, from the viewpoint of the brazing points between the cathode filament and the end hats, as shown in Fig. 2.15. Therefore, the larger amount of electrons will flow in the anode block on the HV input side than that on the RF output side, and this corresponds to the measurement results of the relative amount of the anode current, as described in Sec. 2.2.

2.4 Summary

In this chapter, we have conducted experimental measurements of electron emission from the filament cathode of a magnetron.

First, we conducted the experimental measurements of the anode current with axially-segmented anode blocks. We found from the experimental results that

- in the cylindrical diode case, 50%, 30%, and 15% of electrons arrived at the center region of the anode, the HV input side, and the RF output side, respectively, and this ratio is independent of the anode voltage and the filament current,
- in the magnetron case, the relative amount of the anode current is similar to that in the cylindrical diode case when the anode voltage is higher than the cutoff voltage, however it gradually shifts from the HV input side to the RF output side as the anode voltage reduces.

We also analyzed the trajectory and the diffusive motion of an electron in the case of both the cylindrical diode and the magnetron from the experimental results. From the analysis, the axial travel distance of the electron by the diffusive motion was comparable to the size of the tube in the cylindrical diode case, and it was much larger than the size of the tube in the magnetron case. Therefore, the axial diffusive motion of the electron is not negligible in a magnetron operation. We have also found out that the axial diffusive motion is caused by the charge density gradient, and that it is hardly linked to the initial velocities of thermal electrons.

A few percent of the electrons flew in the outer sheaths of the anode. If they only have the radial velocity component, electrons are not able to arrive there at all, hence this phenomenon is attributable to the axial diffusive motion by the charge density gradient.

We also conducted the experimental measurements of the filament temperature of a magnetron. From the experimental measurements, we have found out that

- the filament temperature is high enough to sustain the oscillation even after turning off the filament current,
- the filament temperature falls much more on both cathode ends, especially on the RF output side than the center of the cathode after turning off the filament current,

when the magnetron is operated by a DC stabilized power supply. The latter item is mainly caused by the structure of the magnetron. The axial distribution of the filament temperature is originally symmetric; however, the measurement results show that the axial distribution is asymmetric because the center of the cathode filament is out of alignment axially from the center of the anode vane to the HV input side.

Summarizing this chapter from the viewpoint of electron emission from the cathode filament, we conclude that electrons are estimated to be emitted most in the center region, next on the HV input side, and least on the RF output side in the examined magnetrons. The conclusion is closely linked to newly-designed low noise magnetrons with cathode shields, because suppressing thermionic emission from both the cathode filament ends, especially from the HV input side contributes a great deal to the reduction of spurious noises, as described in Sec. 4.3.

Chapter 3

Time Domain Analysis of Magnetron Noises

3.1 Introduction

In this chapter, we describe a time domain analysis of magnetron noises when a magnetron is driven by a half-wave voltage doubler, as shown in Fig. 3.1. The analysis is conducted with a view to studying the relationship between the operating point of the magnetron and the noises. The half-wave voltage doubler is one of the typical power supplies for a magnetron in a microwave oven.

For the time domain analysis in the present thesis, the spectral intensity of the noise generated at a certain frequency is measured in the time domain. This is displayed in synchrony with the anode current waveform of the magnetron, and then the anode current value at the maximum noise level is derived at the examined frequency.

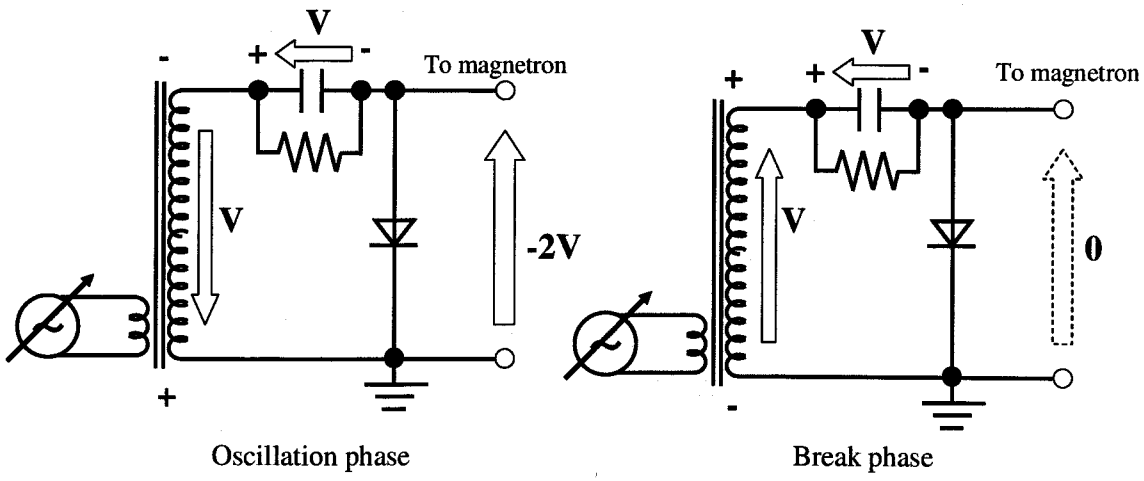

Figure 3.1: Half-wave voltage doubler.

With regard to the time domain analysis of a magnetron, Matsumoto *et al.* has conducted it in the fundamental band in order to investigate EMC between a microwave oven and wireless communication system in the 2.4GHz band, that is to say, WLAN [7, 8]. They constructed a time domain noise model, which consisted of a series of frequency modulated tone bursts realized with a set of FM/AM modulators, for a microwave oven [7]. As described above, even the fundamental oscillation of a 2.45GHz magnetron is taken as a noise source for WLAN systems in this day and age.

Also, the sources of line noises in the MF, VHF and UHF bands have been studied by Yamamoto *et al.* [4, 6]. Although the fundamental solution for a magnetron to be installed in a commercialized microwave oven has not been found out yet, one of the objectives of their study has been EMC of a microwave oven with broadcasting services such as radio and television.

In this chapter, we describe that we could classify noises from a magnetron into five types from the time domain analysis. Also, generation mechanisms of some spurious noises are analytically discussed.

3.2 Measurement system

Fig. 3.2 and Fig. 3.3 show a schematic and a photo of a measurement system conducted in the present study, respectively. The reference magnetron 2M210M1F1 was used for the experiments. A half-wave voltage doubler was used for the magnetron operation.

Fig. 3.4 shows the anode current waveform and the anode voltage waveform when the magnetron is operated by the half-wave voltage doubler. In the case of a half-wave voltage doubler, a magnetron repeats the oscillation and the break at every half period. At the oscillation period, the anode current and the anode voltage vary in time, *i.e.* the operating point varies in time as shown in Fig. 3.4. In this study, such variations of the operating point are used to measure the anode current at the maximum noise level for each noise generating frequency in order to analyze the relationship between the noise at the examined frequency and the operating point.

After the magnetron was brought into the oscillation with a specified anode current value of 300mAdc, the measurement is initiated when the magnetron and the waveguide are thermally stable. The measurement is conducted in the condition that the feedthrough capacitor and the choke coil attached to the magnetron are removed, in order to detect all spurious noises generated from the magnetron itself as much as possible. The measured frequency bands are 100kHz–1GHz for the low frequency bands, 2.35–2.55GHz for the fundamental bands, and 4–14GHz for the high frequency bands. In the low frequency bands, line noises on cables between the magnetron and the half-wave voltage doubler are measured with a current probe (FCC F-55). In the fundamental frequency bands and the high frequency bands, leakage electromagnetic waves are measured with a spiral antenna and a horn antenna, re-

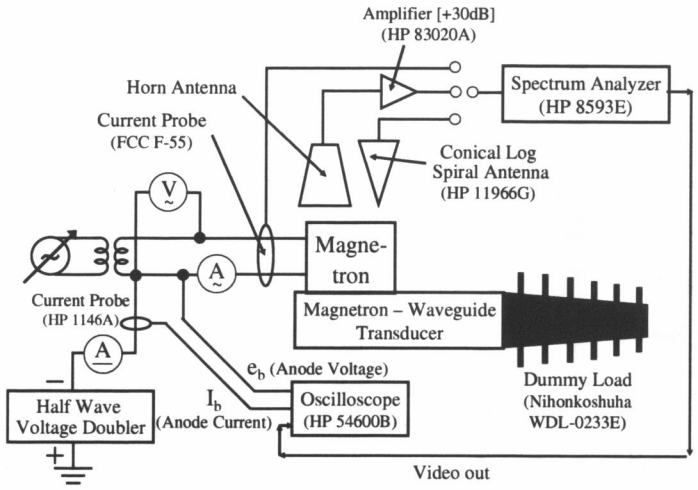

Figure 3.2: Schematic of a measurement system for a time domain analysis.

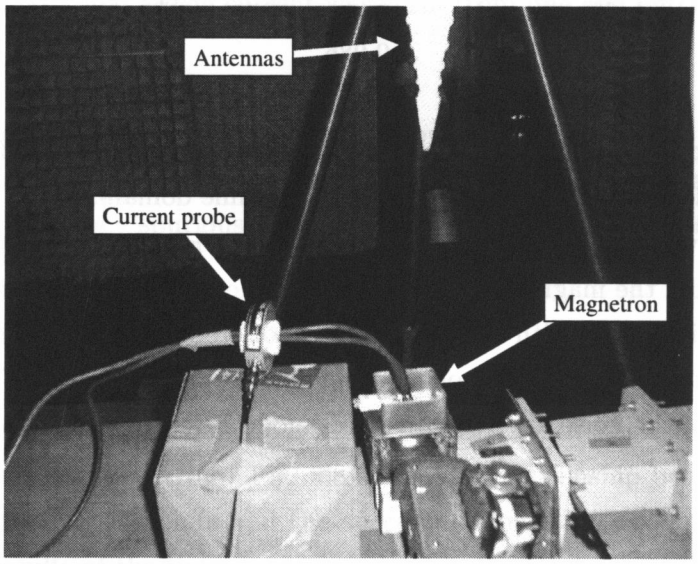

Figure 3.3: Photo of the measurement system.

spectively. Since these measurements are not those for the spectrum radiated from the RF output of the magnetron, one cannot derive the absolute value of the spectral intensity radiated from the output antenna. However, since the main objective of the present study is an analysis of the relationship between the noise at the examined frequency and the operating point, this method allowing the spectrum measurement in various frequency bands is used.

The magnetron noises in each frequency band are measured with a spectrum analyzer (HP 8593E). In the present study, the measured frequency range of the spectrum analyzer is zero spanned, in order to observe the magnetron noise in the time domain. The video output signal, which outputs the time domain waveform of the noise displayed on the spectrum analyzer, is synchronized with the anode current waveform of the magnetron in the oscilloscope

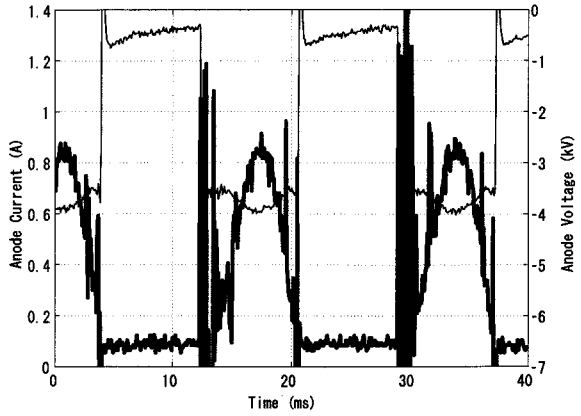

Figure 3.4: Waveforms of the anode voltage (thin line and left axis) and the anode current (thick line and right axis) of the magnetron driven by the half-wave voltage doubler.

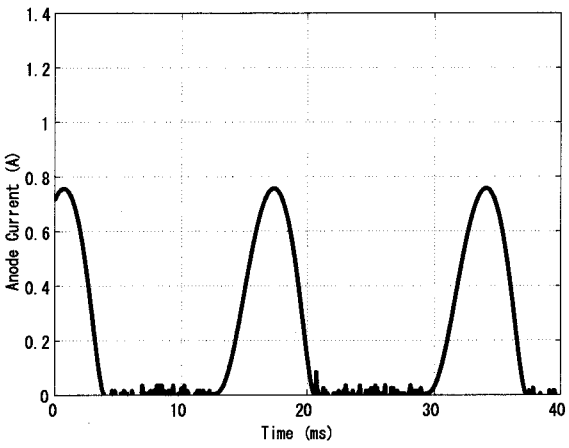

Figure 3.5: Corrected waveform of the anode current approximated by a 9th polynomial curve. The correlation factor is 0.986.

display (HP 54600B). In this way, the relationship between the spectral intensity at a certain frequency and the anode current can be monitored in the time domain.

The anode current waveform shown by the thick lines in Fig. 3.4 is superposed on the line noises generated from the magnetron. Therefore, for the anode current waveform, a 9th polynomial approximation curve with the effect of the noise elimination (with a correlation factor of 0.986) is used as the corrected anode current waveform, as shown in Fig. 3.5. Then, the relationship between the noise and the corrected anode current waveform is analyzed in the time domain.

3.3 Experimental results

As an example of the data obtained in the present measurement method, Fig. 3.6 shows the video output signal waveform from the spectrum analyzer (thick line) and the anode current waveform (thin line) when the low frequency line noise at 2MHz is measured. The video output signal from the spectrum analyzer provides a waveform whose signal levels are 0~1V. Here, the signal levels of 1V and 0V correspond to the top and bottom of the grid lines on the display of the spectrum analyzer, respectively. Thus, the magnitude of the video output signal corresponds to the noise level on the time axis at the measured frequency. In this study, the anode current at the maximum video output signal is defined as the "spectrum generation anode current value" $I_g(f)$ at a frequency of f. Then, the relationship between f and $I_g(f)$ is analyzed. For instance, the anode current at the time when the video output signal becomes the maximum at a frequency of 2MHz is 0.096A, as shown in Fig. 3.6; hence $I_g(f = 2\text{MHz})$ is equal to be 0.096A.

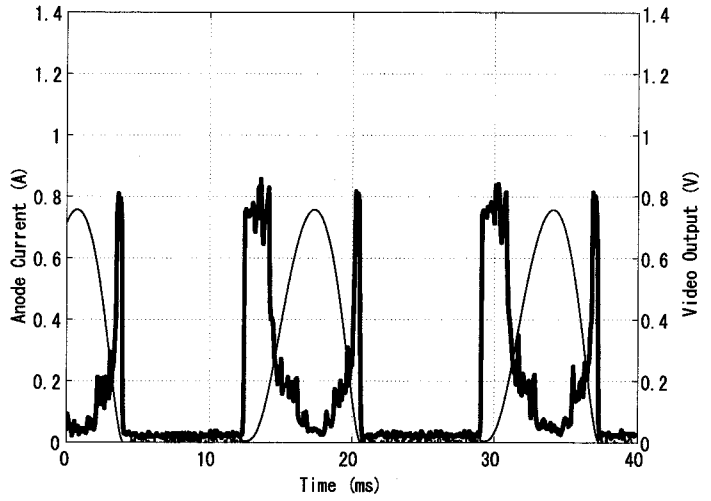

Figure 3.6: Waveforms of a video output signal from the spectrum analyzer (thick line and right axis) and the corrected anode current waveform (thin line and left axis) at a frequency of 2MHz.

In the following subsections, firstly the time domain analysis results on the fundamental spectrum of the magnetron are discussed. Then, the time domain analysis results are explained for high frequency spurious noises and low frequency line noises.

3.3.1 Fundamental spectrum

Fig. 3.7 shows the measurement results of the fundamental spectrum of the magnetron. In the present experiment, the time domain analysis was carried out at the frequencies indicated by ○ on the fundamental spectrum. Fig. 3.8 shows the relationship between the frequency of the time domain analysis points and the spectrum generation anode current $I_g(f)$. All the experimental results of the time domain analysis in the fundamental bands are shown in Appendix A.1.

3.3.2 High frequency spurious noises

Fig. 3.9 shows the measured spurious spectrum in the high frequency bands. In the present experiment, the time domain analysis was performed at the frequencies indicated by ○ on the high frequency spurious spectrum in Fig. 3.9. The time domain analysis results of the high frequency spurious noises are shown in Fig. 3.10. All the experimental results of the time domain analysis in the high frequency bands are shown in Appendix A.2.

3.3.3 Low frequency line noises

Fig. 3.11 shows the measured line noise spectrum generated from the magnetron at low frequencies. In the present experiment, the time domain analysis was carried out at the

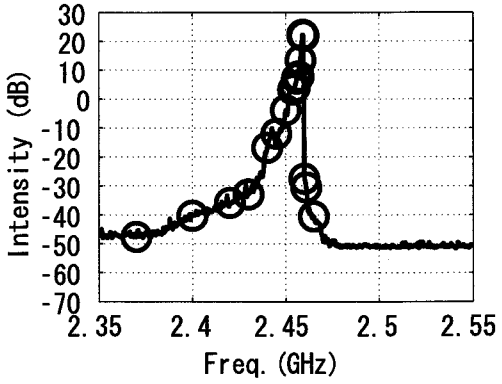

Figure 3.7: Spectrum of the magnetron in the fundamental bands. ○ shows time domain analysis points.

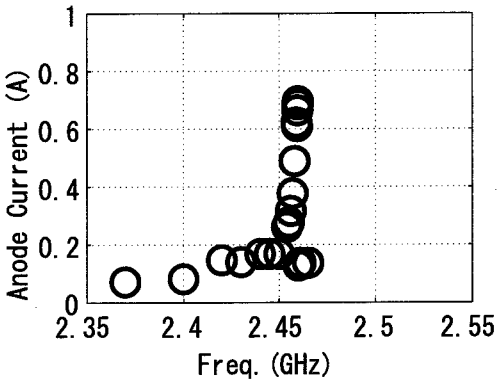

Figure 3.8: Time domain analysis in the fundamental bands.

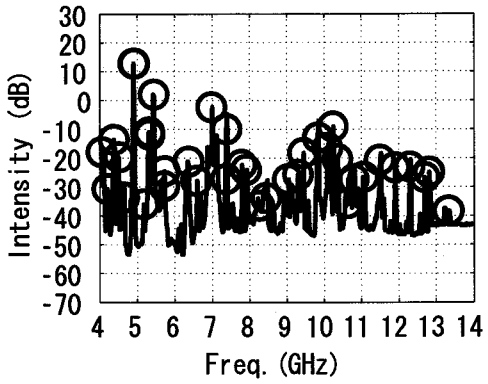

Figure 3.9: Spurious noises from the magnetron in the high frequency bands. ○ shows time domain analysis points.

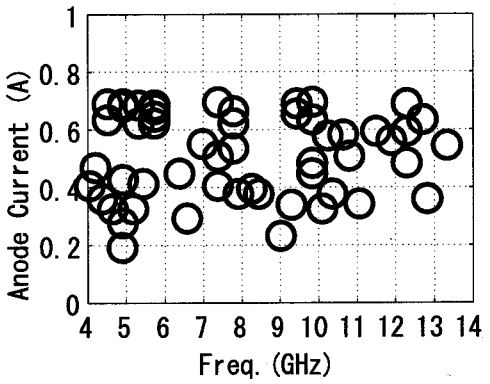

Figure 3.10: Time domain analysis of spurious noises in the high frequency bands.

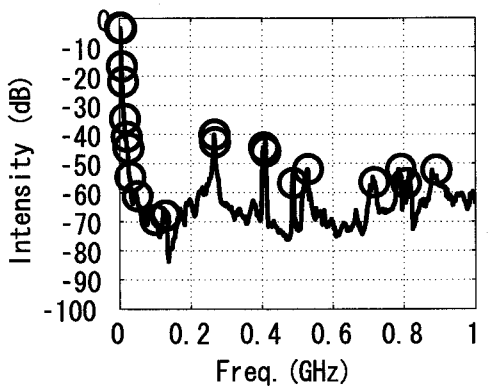

Figure 3.11: Line noises from the magnetron in the low frequency bands. ○ shows time domain analysis points.

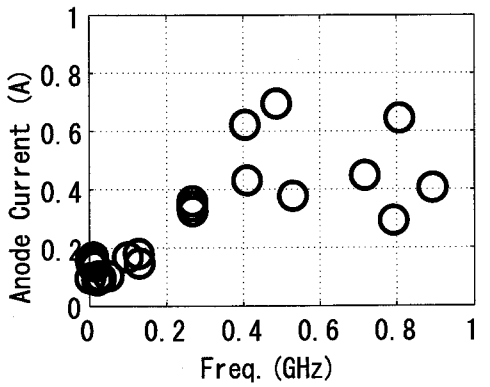

Figure 3.12: Time domain analysis of the line noises in the low frequency bands.

frequencies indicated by ○ on the low frequency line noise spectrum in Fig. 3.11. The results of the time domain analysis of the low frequency line noises are shown in Fig. 3.12. All the experimental results of the time domain analysis in the low frequency bands are shown in Appendix A.3.

3.4 Classifications of magnetron noises by the time domain analysis

3.4.1 Fundamental spectrum

With regard to the fundamental spectrum results, as shown in Fig. 3.7 and Fig. 3.8, there is a tendency for the increase of $I_g(f)$ as the frequency becomes higher from the lower frequency side up to the peak frequency of 2.4597GHz. The peak frequency is obtained where the anode current becomes the maximum. This result indicates the frequency pushing characteristic of a magnetron. Frequency pushing is a phenomenon in which the oscillation frequency increases with the anode current of the magnetron [38]. This is a primary cause of the expanse of the oscillation bandwidth when a magnetron is driven by a non-smoothed power supply. Thus, frequency pushing of the fundamental wave is confirmed by the time domain analysis.

Note that $I_g(f)$ indicate less than 0.2A in lower side bands from 2.35GHz to about 2.45GHz and the upper side bands from 2.46GHz. In these side bands, the slope of $I_g(f)$ is quite different from that observed in the frequency pushing. Therefore, the generation mechanism in these side bands named "side band noises around the carrier" is different from that of the fundamental oscillation.

3.4.2 High frequency spurious noises

With regard to the high frequency spectrum results, as shown in Fig. 3.9 and Fig. 3.10, we first classified the high frequency spurious noises into two groups; the harmonic components of the fundamental, and the spurious noises excluding the harmonics. Then, we subdivided the latter spurious noises into two groups; $I_g(f)$ is equal to around 0.4A and around 0.6A.

The harmonics of the fundamental

In the case of the harmonic components of the fundamental, $I_g(f)$ is observed to be near 0.7A, which is the maximum value of the anode current waveform, as shown in Fig. 3.10. Also, since frequency pushing is observed as in the fundamental case, the harmonics are found to be generated in synchrony with the fundamental.

Spurious noises excluding the harmonics generated at $I_g(f)$ of around 0.4A

With respect to the spurious components excluding the harmonics, Fig. 3.13 shows a histogram of $I_g(f)$ when the time domain analysis points ○ in Fig. 3.10 are used as the sampling

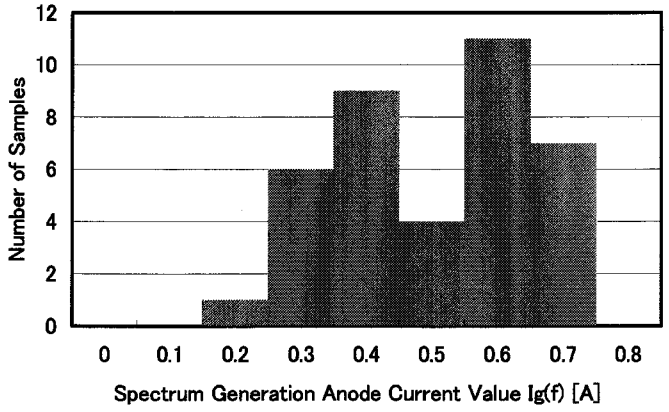

Figure 3.13: Histogram of the spectrum generation anode current values $I_g(f)$ from time domain analysis results of high frequency bands excluding the harmonics.

points. Here, the anode current values are classified by rounding up and down the first two decimal places. From Fig. 3.13, $I_g(f)$ can be divided into two groups. One is the noise group generated at $I_g(f)$ of around 0.4A. Considering the anode current waveform and the anode voltage waveform in Fig. 3.4, it is found that the anode voltage at an anode current of around 0.4A is in the region of transition from the constant voltage range, where the anode voltage is almost constant with an increasing anode current, to the non-constant voltage range, where the anode voltage increases with the anode current.

Spurious noises excluding the harmonics generated at $I_g(f)$ of around 0.6A

Another source is the noise group generated at $I_g(f)$ of around 0.6A from the histogram in Fig. 3.13. The frequencies of this noise group are distributed in a characteristic manner; these noises are generated at a frequency interval of ±400MHz and ±800MHz with respect to the harmonics. As the source of this noise group, it is most appropriate to consider intermodulation between the harmonics and the low frequency line noises of 400MHz or 800MHz, since the generation behavior is very similar to that for the low frequency noises at 400MHz and 800MHz, as shown in Fig. 3.11 and Fig. 3.12.

3.4.3 Low frequency line noises

With regard to the low frequency spectrum results, as shown in Fig. 3.11 and Fig. 3.12, we first divide the line noises into two groups; in the frequency bands over 150MHz and below 150MHz. Then we subdivided line noises over 150MHz into three groups.

Line noises over 150MHz

First, with respect to the line noises generated over 150MHz, Fig. 3.14 shows a histogram of $I_g(f)$ when the time domain analysis points ○ in Fig. 3.12 are used as the sampling points.

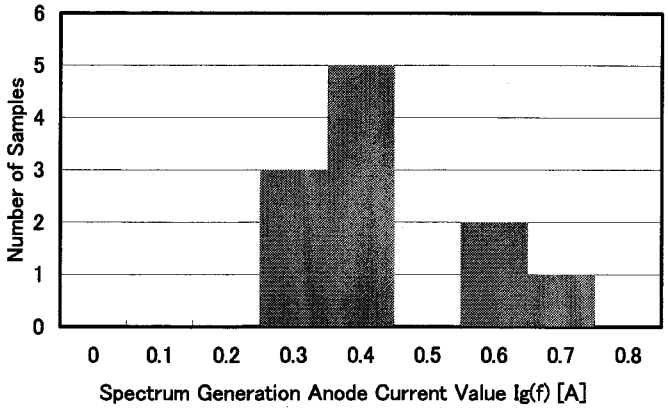

Figure 3.14: Histogram of the spectrum generation anode current values $I_g(f)$ from time domain analysis results of low frequency bands over 150MHz.

Here, the anode current values are rounded up or down in the first two decimal places. Fig. 3.14 shows that the anode current value $I_g(f)$ with the highest rate is 0.4A and that this situation is in the transition region between the constant voltage range and the non-constant range, as in the case of the high frequency spurious noises other than the harmonics.

Line noises at 400MHz and 800MHz

At 400MHz and 800MHz, noises occurs in the non-constant voltage range in which $I_g(f)$ is equal to around 0.6A. They seem to be related to the noises generated at a frequency interval of $\pm$400MHz and $\pm$800MHz with respect to the harmonics, since both of them are generated at the same $I_g(f)$. As a feature, the noise levels are higher than those in the surrounding regions.

Line noises generated in synchrony with electron circulation

Further, the strong noise generated at 487MHz is found to occur in the non-constant voltage range with $I_g(f)$ of more than 0.6A, as at 400MHz and 800MHz. However, this noise frequency is close to 1/5 of the oscillation frequency of 2.45GHz. This is a noise generated in synchrony with the circulation motion of electrons [4]. The generation mechanism of the noise above is described in detail in the next section.

Line noises below 150MHz

On the other hand, the line noise generated at frequencies below about 150MHz is found to occur at $I_g(f)$ of less than 0.2A. It is expected that the noise generation mechanism is different from those described above.

Of great interest is that the side band noises around the carrier are also generated at almost the same $I_g(f)$. Therefore, line noises below 150MHz may be highly relevant with the

side band noises. Here we identified these line noises below 150MHz as the side band noises around the carrier.

3.4.4 Summary of classifications

From the time domain analysis results, magnetron noises can be classified into the following five types;

(1) Side band noises around the carrier and low frequency line noises at frequencies below about 150MHz, generated at an anode current of less than 0.2A.

(2) High frequency spurious noises and low frequency line noises generated in the transition region between the constant voltage range and the non-constant voltage range at an anode current of around 0.4A.

(3) Low frequency line noises generated in the non-constant voltage range characterized by frequencies of 400MHz or 800MHz, and high frequency spurious noises generated at an anode current of around 0.6A, attributed to the intermodulation of the low frequency line noises and the harmonics.

(4) The harmonics generated in synchrony with the fundamental.

(5) Low frequency line noises generated in synchrony with the electron circulation.

Fig. 3.15 shows the frequency spectra in the left column and the time domain analysis results in the right column, respectively, whose data are the same as shown from Fig. 3.7 to Fig. 3.12, but are classified according to the noise types. Colored circles show the time domain analysis points classified according to the noise types, as the color table of the classified noise types applicable to Fig. 3.15 is shown in Table 3.1.

Table 3.1: Color table of the classified noise types applicable to Fig. 3.15.

Type (1)	orange
Type (2)	purple
Type (3)	pink
Type (4)	green
Type (5)	blue
Fundamental oscillation	black

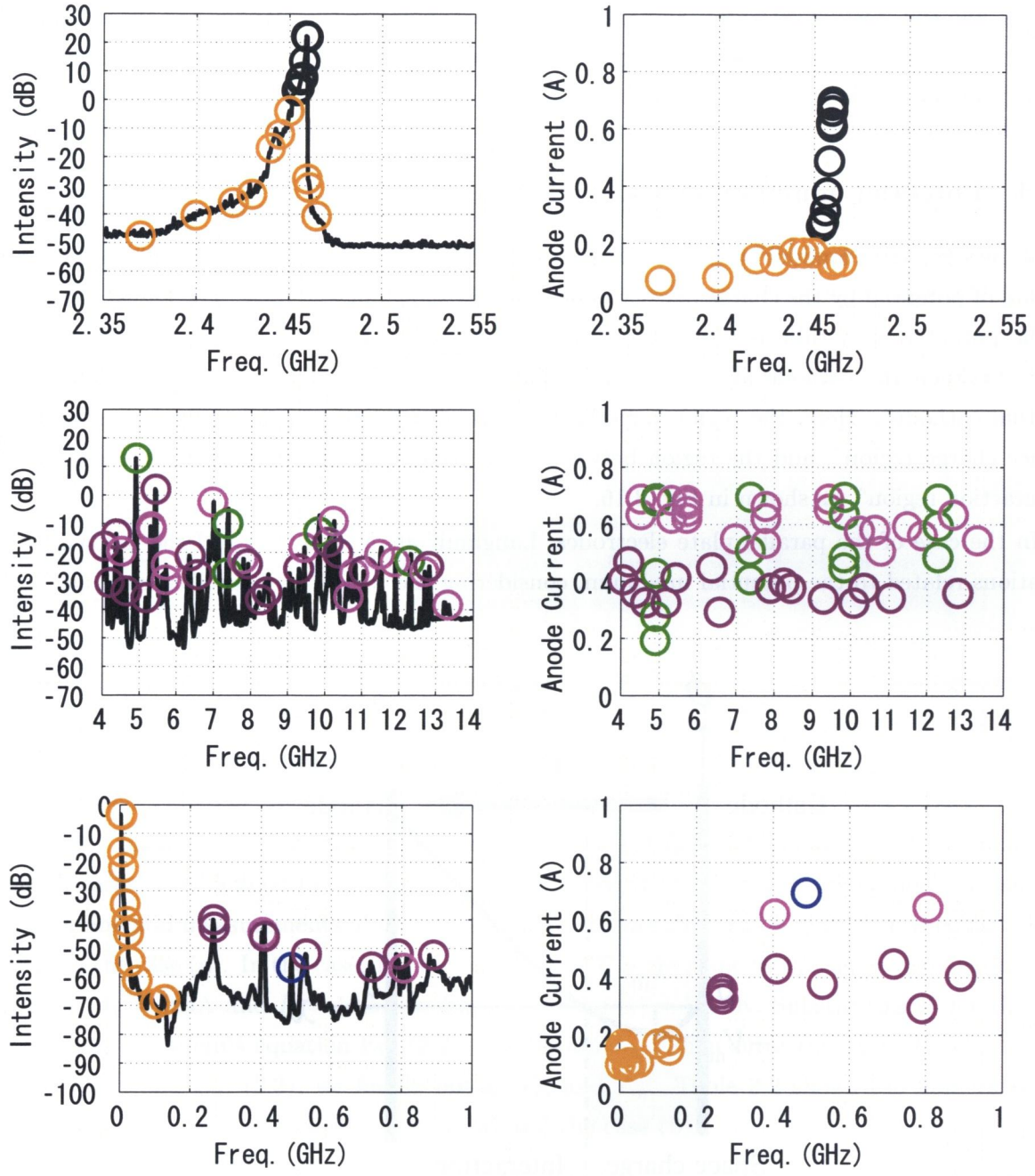

Figure 3.15: Colored frequency spectra (left column) and time domain analysis results (right column) of the magnetron. Colored circles show the time domain analysis points classified according to the noise types; the type (1): orange, the type (2): purple, the type (3): pink, the type (4): green, the type (5): blue, and the fundamental oscillation: black.

3.5 Discussions of noise sources of a magnetron

In this section, we first describe the "potential minimum", the fall of potential by the charge density, and the "virtual cathode", another zero potential between the cathode and the anode. Then, we discuss noise sources of a magnetron with respect to each classification described in the previous section.

3.5.1 Potential minimum and virtual cathode

Since there is a large amount of thermal electrons in the vicinity of the cathode in a magnetron, the fall of potential by the charge density takes place as shown in Fig. 3.16. The lowest value of the potential in a tube is named "potential minimum". Then, another zero potential exists between the cathode and the anode. The position of the zero potential is named "virtual cathode". Here, the region between the cathode and the virtual cathode is called "space charge region", and the region between the virtual cathode and the anode is called "interaction region", as shown in Fig. 3.16.

In the case of the parallel plate electrodes, Langmuir analytically derived the following equations related to the potential minimum, considering the initial velocity of thermal elec-

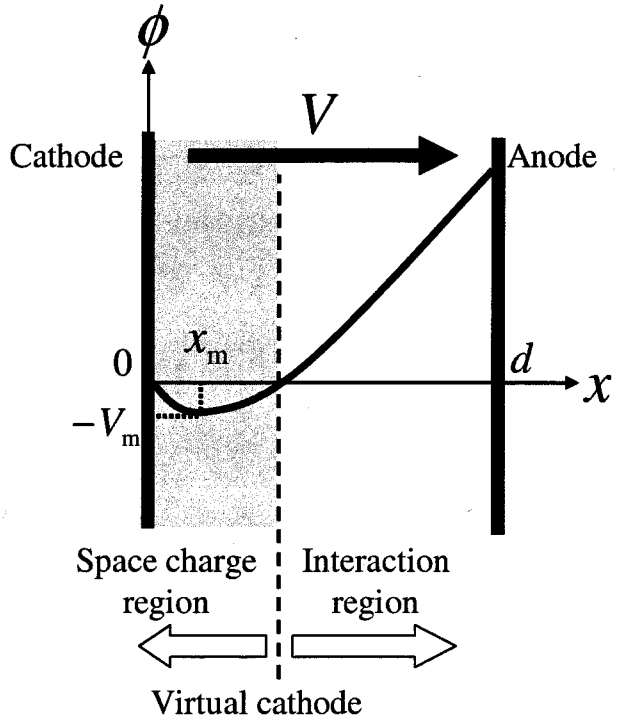

Figure 3.16: Potential minimum and virtual cathode. d: distance between the anode and the cathode, V: anode voltage, V_m: potential minimum, x_m: position of the potential minimum from the cathode.

trons [55];

$$I_{\rm b} = S_{\rm a}\frac{\sqrt{2}}{9\pi}\sqrt{\frac{e}{m}}\frac{(V-V_{\rm m})^{\frac{3}{2}}}{(d-x_{\rm m})^2}\left(1+2.66\sqrt{\frac{V_{\rm T}}{V+V_{\rm m}}}\right), \tag{3.1}$$

$$V_{\rm m} = V_{\rm T}\ln\frac{I_{\rm th}}{I_{\rm b}} = \frac{T}{(11600\ {\rm K/V})}\ln\frac{I_{\rm th}}{I_{\rm b}}, \qquad V_{\rm T} = \frac{T}{(11600\ {\rm K/V})}, \tag{3.2}$$

where $I_{\rm b}$ is the anode current, $I_{\rm th}$ is the saturation current of electron emission given by the Richardson-Dushman's equation Eq. (2.21), $S_{\rm a}$ is the surface area of the anode, V is the anode voltage, T is the cathode temperature in Kelvin, d is the distance between the anode and the cathode, $V_{\rm m}$ is the absolute value of the potential minimum, and $x_{\rm m}$ is the position of the potential minimum from the cathode as shown in Fig. 3.16. Assuming that $I_{\rm th}$ is several times larger than $I_{\rm b}$, $x_{\rm m}$ is expressed as the following;

$$x_{\rm m} = \frac{2.55-\sqrt{2(I_{\rm b}/I_{\rm th})}}{(9.18\ {\rm A}^{-\frac{1}{2}}{\rm K}^{\frac{3}{4}})\times\sqrt{I_{\rm b}/S_{\rm a}}T^{-\frac{3}{4}}}\times 10^{-5}. \tag{3.3}$$

In the case of a magnetron, the influence of the initial velocity is less than the case of the parallel plate electrodes [57], although equations of the potential minimum has not been derived yet because they are difficult to solve mathematically. Hence, we estimate the potential minimum and its position in a magnetron by analogy with the equations of Eq. (3.1), Eq. (3.2) and Eq. (3.3).

Assuming that the anode is a perfect cylinder and it has no cavities and gaps between anode vanes, then $S_{\rm a} = 2\pi r_{\rm a}h$, where $r_{\rm a}$ is the anode radius and h is the anode height. The emitting material of the filament is a carburized thoriated tungsten (W_2C+Th), and its thermionic emission constant and work function are $0.97\times10^4{\rm A/m^2/K^2}$ and 2.18eV, respectively. Then we calculate $V_{\rm m}$ and $x_{\rm m}$ in two cases: (a) $I_{\rm b}$ = 400mA and (b) $I_{\rm b}$ = 5mA. In both cases, T is defined by the filament temperature at the center of the cathode. From the experimental measurements of the filament temperature shown in Fig. 2.13, T is equal to 2000K in the case (a). In the case (b), we assume that T is the same as that in the preheating state *i.e.* $I_{\rm b}$ = 0mA and $I_{\rm f}$ = 10.5A in Fig. 2.13; then, T = 1890K. Substituting T for the Richardson-Dushman's equation Eq. (2.21), we obtain $I_{\rm th}$. Then substituting T, $I_{\rm th}$ and $I_{\rm b}$ for Eq. (3.2) and Eq. (3.3), we finally obtain $V_{\rm m}$ and $x_{\rm m}$. Table 3.2 shows the numerical results of $I_{\rm th}$, $V_{\rm m}$ and $x_{\rm m}$ in both the case (a) and the case (b).

Table 3.2: Table of the filament temperature T, the saturation current of emission $I_{\rm th}$, the potential minimum $V_{\rm m}$ and its position from the cathode $x_{\rm m}$, when $I_{\rm b}$ = 400mA and 5mA.

$I_{\rm b}$	T	$I_{\rm th}$	$V_{\rm m}$	$x_{\rm m}$
(a) 400mA	2000K	14.9A	0.624V	1.96×10^{-2}mm
(b) 5mA	1890K	6.36A	1.16V	1.82×10^{-1}mm

As shown in Table 3.2, V_m becomes smaller and x_m comes closer to the cathode as I_b increases. Here, the distance d between the anode and the cathode is 2.525mm in the reference magnetron. Therefore, x_m is estimated to be about 0.8% of d in the case (a), and about 7% of d in the case (b).

These numerical results above are explained in the following. When the anode current is relatively low, the amount of electrons in the interaction region is also relatively small. Thus, the large amount of electrons is stored in the space charge region. Some electrons hardly overcome the potential minimum and they return to the cathode. As the anode current increases, electrons gradually shift from the space charge region to the interaction region, and they contribute to amplification of the oscillation. On the other hand, the amount of electrons in the space charge region is gradually small, and then the potential minimum gradually rises due to the decrease of the space charge density. At the same time, the position of the potential minimum comes closer to the cathode. When the anode current is comparable to the saturation current of electron emission *i.e.* $I_b \approx I_{th}$, almost all the electrons flow into the anode, therefore, neither the potential minimum nor the virtual cathode exist any longer.

3.5.2 Discussions of sources of the magnetron noises classified by the time domain analysis

Now we discuss sources of the magnetron noises classified by the time domain analysis. The classification is summarized in Subsec. 3.4.4.

Type (1): noises generated at an anode current of less than 0.2A

The type (1) is the side band noises around the carrier and the low frequency line noises at frequencies below about 150MHz, generated at an anode current of less than 0.2A.

Detailed analysis of the noise generated at frequencies below 150MHz, it is indicated that the noises are generated suddenly from the start-up of the oscillation, as represented by the video output signal in Fig. 3.6. Therefore, sudden irregular motion of electrons or distortion of the microwave electromagnetic field by discontinuities at the start-up of the oscillation is conceivable as a candidate for noise sources of the type (1).

With respect to the type (1) at frequencies below about 150MHz, the ion plasma oscillation (near 10 MHz and its harmonics) and the ion relaxation oscillation (several hundred kHz–1MHz) are noted as noise sources by Yamamoto *et al.* [4], although a question arises whether the neutral plasma conditions are met in a magnetron.

Ion plasma oscillation

The ion plasma oscillation is considered as one of the line noises sources below 150MHz described by Yamamoto *et al.* [4, 6]. The ion plasma oscillation takes place in the space charge region if it exists, and the ion plasma frequency f_{pi} of a monovalent ion is given by

the following equation;

$$f_{\mathrm{pi}} = \frac{1}{2\pi}\sqrt{\frac{e\rho_{\mathrm{i}}}{m_{\mathrm{i}}\varepsilon_0}}, \tag{3.4}$$

where e is the elementary charge, ρ_{i} is the charge density of the ion, m_{i} is the ion mass and the ε_0 is the dielectric constant in vacuum. Here, Yamamoto *et al.* have assumed that the charge neutrality $\rho_{\mathrm{i}} = \rho_{\mathrm{e}}$ is satisfied in the space charge region [6].

Now the charge density of electrons ρ_{e} in the space charge region is estimated from the analogy of the Hull's cutoff equation Eq. (2.18). Note that the Hull's cutoff equation Eq. (2.18) is a conditional equation where the potential $\phi(r)$=V at a anode radius of r_{a}. Then, we generalize Eq. (2.18) at a anode radius of r, the Hull's cutoff equation is rewritten by the replacement of V and r_{a} by $\phi(r)$ and r, respectively;

$$\phi(r) = \frac{eB^2}{8m}r^2\left(1 - \frac{r_{\mathrm{c}}^2}{r^2}\right)^2. \tag{3.5}$$

Then, substituting $\phi(r)$ in Eq. (3.5) for the Poisson's equation Eq. (2.1), ρ_{e} in the space charge region at a radius of r is expressed in the following [58];

$$\rho_{\mathrm{e}} = -\frac{\varepsilon_0}{2}\frac{eB^2}{m}\left(1 + \frac{r_{\mathrm{c}}^4}{r^4}\right). \tag{3.6}$$

Also, they assumed that the relation between the position of the potential minimum x_{m} and the cathode radius r_{c} is estimated to be

$$\frac{x_{\mathrm{m}}}{r_{\mathrm{c}}} = 1.10, \tag{3.7}$$

and that the residual gas in a magnetron is nitrogen [6]. Then f_{pi} is calculated to be 10.4MHz.

Therefore, they have concluded that the ion plasma oscillation was one of the noise sources of a magnetron below 150MHz.

Possibility of ion plasma oscillation in a magnetron

Here we discuss a possibility of the ion plasma oscillation in a magnetron.

First, Yamamoto *et al.* [4, 6] assumed that the charge density of electrons is equal to be that of positive ions like a neutral plasma situation. Here the number of electrons n_{e} in a magnetron can be calculated to be $6.9 \times 10^{16}\mathrm{m}^{-3}$ by Eq. (3.6), $\rho_{\mathrm{e}} = en_{\mathrm{e}}$, and the assumption of Eq. (3.7). Hence, the assumption that the charge density of electrons is equal to be that of positive ions in a magnetron turns out to be questionable since the number of positive ions n_{i} in the magnetron has to be equal to n_{e} if the magnetrons satisfies the neutral plasma condition.

Next, we discuss whether the plasma condition that the Debye length is much less than the length of a system. The Debye length λ_{D} is expressed in the following [59];

$$\lambda_{\mathrm{D}} = \sqrt{\frac{\varepsilon_0 kT_{\mathrm{e}}}{n_e e^2}}, \tag{3.8}$$

where T_e is the electron temperature. Now we regard T_e as the potential energy of electrons which just overcome the potential minimum V_m. Then, T_e is equal to be (11600 K/V)$\times V_m$, and we assign $V_m = 1.16$V, the potential minimum at an anode current of 5mA in Table 3.2. Hence, λ_D is calculated to be 30.5μm. Assuming that L, which is expressed as the space charge region of the reference magnetron, is estimated to be at most 10% of the distance between the anode and the cathode, L =0.2525mm. Finally, we obtain $L \approx 8.28\lambda_D$.

It is a little bit difficult to state that the plasma condition $\lambda_D \ll L$ is satisfied in a magnetron. Moreover, L becomes gradually shorter and shorter as the anode current increases, from the relationship between the position of the potential minimum x_m and the anode current I_b shown in Table 3.2.

Finally we conclude that the ion plasma oscillation will hardly take place since the plasma conditions are hardly satisfied in a magnetron.

Relaxation oscillation

The ion relaxation oscillation is also described by Yamamoto *et al.* [4,6]. The ion relaxation oscillation is occurred by the trapped ions in the vicinity of the cathode. Since these ions are repeatedly ionized and neutralized, the vibration of the potential minimum takes place at frequencies from several hundred kHz to 1MHz.

The relaxation oscillation frequency f_r is given by

$$f_r = 2n_g\sigma v, \tag{3.9}$$

where n_g is the gas density, σ is the area of ionization and v is the velocity of electrons [6]. In their experimental results, f_r is calculated to be 1110Hz.

There is a possibility that the ion relaxation oscillation takes place since it is independent of the plasma conditions.

Type (2): noises generated in the transition region

The type (2) is the high frequency spurious noises and the low frequency line noises generated in the transition region between the constant voltage range and the non-constant voltage range of the magnetron.

The operating modes of the magnetron in the constant voltage range and the non-constant voltage range can be explained as follows. In the constant voltage range, the anode voltage is determined independently from the increase or decrease of the anode current. Therefore, there is a large amount of electrons in the space charge region when a magnetron oscillates in the constant voltage range. On the other hand, in the non-constant voltage range, the anode voltage rises with the increase of the anode current, due to gradual deficiency of electrons in the magnetron. In this range, the thermal electron emission is promoted by intensification of the electrostatic field. Hence, it is to be expected that the dynamic characteristics of the magnetron will change considerably in the transition stage. Candidates for noise sources

include the distortion of the microwave electromagnetic field, or the interaction between the microwave electromagnetic field and irregular motion of electrons in the space charge region when the magnetron characteristics change drastically in the transition region.

Since strong line noises are also generated at an anode current of around 0.4A even at low frequencies, sources of the line noises also include the distortion of the microwave electromagnetic field or the interaction between the microwave electromagnetic field and motion of electrons in the space charge region when the magnetron characteristics change drastically in the transition region. Also, the intermodulation between the low frequency line noises and the harmonics may be considered as another source of the magnetron noises.

Type (3): noises characterized by frequencies of 400MHz or 800MHz

The type (3) is the noises characterized by frequencies of 400MHz or 800MHz.

Although the generation mechanism of the noises assigned to the type (3) has not been clear yet, we found out no frequency pushing like that for the fundamental oscillation as a result of detailed time domain analysis. Since the type (3) noises are generated stronger than the other types, it is likely that the type (3) noises are extraordinarily generated by other resonant conditions and other oscillation conditions which are different from the fundamental oscillation. Now we discuss the electron motions and resonance conditions in a magnetron.

Electron motions and resonance conditions in a magnetron

Considering a magnetron with symmetrically-placed N resonant cavities, the resonance conditions are given by the following expression [60];

$$\omega = \tau\Omega_1 + (\sigma - \tau)\Omega_2, \qquad \tau = 0, 1, 2, \cdots, \sigma \tag{3.10}$$

$$\sigma = Z, Z + N, Z + 2N, \cdots, Z + \mu N, \qquad \mu = 0, 1, 2, \cdots,$$

$$Z \equiv \frac{\alpha N}{2\pi} \equiv 0, 1, 2, \cdots, N - 1 \tag{3.11}$$

where ω is the resonant angular frequency, α is the phase difference between the adjacent anode vanes, τ and μ are the integer numbers. Z is named the "number of oscillation types". Ω_1 and Ω_2 are the angular velocities expressed in Eq. (2.15), Eq. (2.16) and Eq. (2.17). In terms of τ and σ, there are selectional rules as the following [60];

(I) if $\tau = 0$, then electron spokes are generated independently of the initial phase of electrons, therefore there is a possibility that strong oscillation unconditionally takes place,

(II) if $0 < \tau/\sigma < \frac{1}{2}$, then there is a possibility that strong oscillation unconditionally takes place, as long as B is near the cutoff magnetic flux density B_c,

(III) if $\tau/\sigma > \frac{1}{2}$, then only electrons whose initial phase is matched to that of the electromagnetic field contribute to oscillation as long as B is near B_c, therefore there is a possibility that weak oscillation takes place,

(IV) if $\tau/\sigma = \frac{1}{2}$, no oscillation takes place,

where the cutoff magnetic flux density B_c is derived from the replacement of the Hull's cutoff equation [1];

$$B_c^2 = \frac{8m}{e} \frac{r_a^2 V}{(r_a^2 - r_c^2)^2}. \tag{3.12}$$

All of the modern cylindrical magnetrons are operated in the selectional rule (I) and the π-mode oscillation, in order to enhance the microwave power most efficiently; therefore τ=0 and $\alpha = \pi$, *i.e.* $Z = N/2$. In the reference magnetron case, $N = 10$, then the π-mode oscillation is carried out when $Z = N/2 = 5$.

However, the other resonance conditions described in the selectional rules still exist, although they hardly contribute to their strong oscillations.

Here, we numerically calculates the frequencies following the the selectional rules. Assuming the infinitely long cylinder as a magnetron tube, the external magnetic field B is constant and parallel to the axial direction. When we substitute 0.18T, which is the actual

Table 3.3: Frequency table following the the selectional rules of the reference magnetron. The Roman numbers in the parenthesis correspond to the selectional rules. (unit: GHz, $B = 0.18$T)

		τ									
$\sigma = Z$	α	0	1	2	3	4	5	6	7	8	9
0	0	0	—	—	—	—	—	—	—	—	—
1	$\pi/5$	0.448 (I)	4.59 (III)	—	—	—	—	—	—	—	—
2	$2\pi/5$	0.896 (I)	5.04 (IV)	9.18 (III)	—	—	—	—	—	—	—
3	$3\pi/5$	1.34 (I)	5.49 (II)	9.63 (III)	13.7 (III)	—	—	—	—	—	—
4	$4\pi/5$	1.79 (I)	5.93 (II)	10.1 (IV)	14.2 (III)	18.4 (III)	—	—	—	—	—
5	π	2.24 (I)	6.38 (II)	10.5 (II)	14.7 (III)	18.8 (III)	23.0 (III)	—	—	—	—
6	$6\pi/5$	2.69 (I)	6.83 (II)	11.0 (II)	15.1 (IV)	19.3 (III)	23.4 (III)	27.5 (III)	—	—	—
7	$7\pi/5$	3.18 (I)	7.28 (II)	11.4 (II)	15.6 (II)	19.7 (III)	23.8 (III)	28.0 (III)	32.1 (III)	—	—
8	$8\pi/5$	3.66 (I)	7.73 (II)	11.9 (II)	16.0 (II)	20.1 (IV)	24.3 (III)	28.4 (III)	32.6 (III)	36.7 (III)	—
9	$9\pi/5$	4.11 (I)	8.17 (II)	12.3 (II)	16.5 (II)	20.6 (II)	24.7 (III)	28.9 (III)	33.0 (III)	37.2 (III)	41.3 (III)

intensity of the magnetic field at the center of the reference magnetron, for B, the frequencies following the the selectional rules of the reference magnetron are calculated. Table 3.3 shows the frequency table following the the selectional rules. The π-mode oscillation takes places where $\sigma = Z$=5 and τ=0 in Table 3.3. The π-mode oscillation frequency is a little bit smaller than the actual fundamental frequency of the reference magnetron, since Eq. (3.11) is derived on the assumption that the charge density is uniform in the interaction space of the magnetron.

As shown in Table 3.3, the magnetron has a chance to satisfy the resonance conditions at various frequencies which meet the selectional rules of (I), (II) and (III), although these resonance modes are much weaker than the π-mode oscillation. Therefore, the resonance or the weak oscillation would be a noise source of the type (3) if these selectional rules are satisfied.

Type (4): the harmonics of the fundamental

The type (4) is the harmonics of the fundamental.

In general, the harmonics are generated by the distortion of the fundamental oscillation, hence the generation itself is essentially unavoidable. However, the harmonic levels of a magnetron are at most -60dBc [61,62], relatively low compared to solid state devices. This is because a resonance cavity of a present magnetron is formed of an annular-sector as its view is shown in Fig. 3.17.

When we take the angle ψ and the dimensions a and b as indicated in Fig. 3.17, the admittance $Y_r(\lambda)$ of the annular-sector resonator is given by the following equation [63];

$$Y_r(\lambda) = j\sqrt{\frac{\varepsilon_0}{\mu_0}}\frac{h}{\psi a}\frac{J_0(2\pi a/\lambda)N_1(2\pi b/\lambda) - J_1(2\pi b/\lambda)N_0(2\pi a/\lambda)}{J_1(2\pi a/\lambda)N_1(2\pi b/\lambda) - J_1(2\pi b/\lambda)N_1(2\pi a/\lambda)}, \tag{3.13}$$

where λ is the wave length, h is the height of the resonator, $J_n(x)$ is the Bessel function and $N_n(x)$ is the Neumann function. On the other hand, the admittance $Y_n(\lambda)$ of the interaction

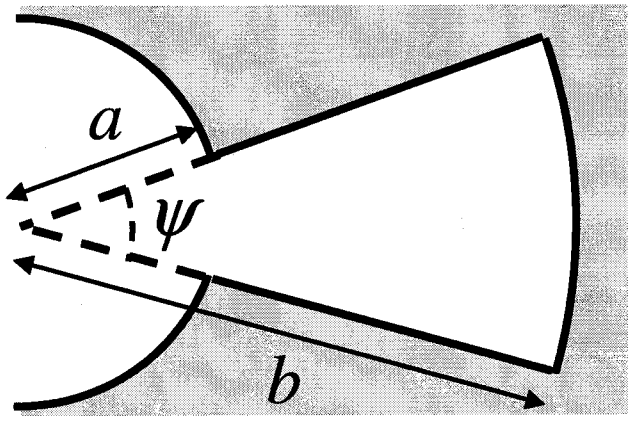

Figure 3.17: Annular-sector resonator.

space is given by the following equation [63];

$$
\begin{aligned}
Y_{\mathrm{n}}(\lambda) &= j\sqrt{\frac{\varepsilon_0}{\mu_0}}\frac{Nh}{2\pi r_{\mathrm{a}}}\sum_{m=-\infty}^{\infty}\left(\frac{\sin(\gamma\psi/2)}{\gamma\psi/2}\right)^2\frac{Z_\gamma(2\pi r_{\mathrm{a}}/\lambda)}{Z'_\gamma(2\pi a/\lambda)}, \qquad (3.14)\\
Z_\gamma(2\pi r_{\mathrm{a}}/\lambda) &= J_\gamma(2\pi r_{\mathrm{a}}/\lambda) - \frac{J'_\gamma(2\pi r_{\mathrm{c}}/\lambda)N_\gamma(2\pi r_{\mathrm{a}}/\lambda)}{N'_\gamma(2\pi r_{\mathrm{c}}/\lambda)},\\
Z'_\gamma(2\pi r_{\mathrm{a}}/\lambda) &= J'_\gamma(2\pi r_{\mathrm{a}}/\lambda) - \frac{J'_\gamma(2\pi r_{\mathrm{c}}/\lambda)N'_\gamma(2\pi r_{\mathrm{a}}/\lambda)}{N'_\gamma(2\pi r_{\mathrm{c}}/\lambda)},
\end{aligned}
$$

where $\gamma = n + mN$, $n = 0, 1, 2, \cdots, N/2$ and m is any integer. When $Y_{\mathrm{n}}(\lambda) + Y_{\mathrm{r}}(\lambda) = 0$, the field resonance of the cavities takes place [63]. Here, λ_0 is assumed to be the root satisfying the resonant condition $Y_{\mathrm{n}}(\lambda_0) + Y_{\mathrm{r}}(\lambda_0) = 0$. In this assumption, $\lambda_M = \lambda_0/(M+1)$ do not satisfy the field resonant condition $Y_{\mathrm{n}}(\lambda_M) + Y_{\mathrm{r}}(\lambda_M) = 0$ at all, where M is the counting number, because of the characteristics of the Bessel function and the Neumann function. Thus, the harmonics at frequencies of integral multiples of the carrier frequency do not resonate in the cavities, and then the harmonic levels are relatively low.

Type (5): line noises generated in synchrony with the electron circulation

The type (5) is the low frequency line noises generated in synchrony with the electron circulation.

The frequency of the noise generated in synchrony with the circulation motion of electrons is theoretically given by the following formula [54]:

$$
\begin{aligned}
f &= \frac{n}{2\pi}\Omega_2 = \frac{n}{2\pi}\left\{\frac{eB}{2m} - \sqrt{\left(\frac{eB}{2m}\right)^2 - \frac{2eV}{m(r_{\mathrm{a}}^2 - r_{\mathrm{c}}^2)}}\right\} \qquad (3.15)\\
n &= 0, 1, 2, \cdots, \frac{N}{2}.
\end{aligned}
$$

Here e is the electron charge, m is the electron mass, B is the magnetic field intensity, V is the anode voltage, r_{a} and r_{c} are the radii of the anode and the cathode, N is the number of anode vanes, and Ω_2 is given by Eq. (2.16). In general, N has an even integer. Eq. (3.15) is also derived from the resonance conditions Eq. (3.11) when we substitute $\tau = 0$ and $\sigma = 0, 1, 2, \cdots, N/2$ for Eq. (3.11).

Let us explain the generation mechanism of the noises in synchrony with the electron circulation. The usual magnetron oscillation is designed in such a way that the phase difference of the microwave electric field between adjacent anode vanes is 180° (this is called the π mode). However, there are other combinations of two anode vanes, not necessarily adjacent to each other, for which the phase difference of the microwave electric field is 180°. The total number of such combinations is $N/2$, including the π mode.

In the reference magnetron, the number of anode vanes N is 10, so that there are five frequencies at which the vibration of the anode vanes are in synchrony with the electron circulation excluding $f = 0$. It is known that a magnetron oscillates in the π mode at a frequency

corresponding to $n = N/2$. The oscillation frequency band (2.45GHz) of the magnetron used in the present experiments is the frequency corresponding to $n = 5$. In contrast, the noise at 487 MHz has a frequency corresponding to about $1/5$ of the oscillation frequency. Hence, this noise is considered to be the noise in synchrony with the electron circulation corresponding to $n = 1$. Noises in synchrony with the electron circulation may exist at other frequencies corresponding to n =2~4. In the present experiments, it is considered that these noises are buried in other noises generated by other causes.

3.5.3 Noises in the constant-voltage range

In the present time domain analysis, the relationship between the anode current and the maximum noise levels at the examined frequency has only focused on. However, spurious noises in various frequency bands are constantly generated with relatively high level in the interval from the start-up of the oscillation to the constant-voltage range, as seen in the video output signals shown in Fig. 3.6 and in Appendix A. As described, there is a large amount of electrons in the space charge region when a magnetron is operated in the constant-voltage range. Here we discuss sources of the noises generated in the constant-voltage range.

Anode current in the constant-voltage range

We assume that the magnetron is an infinitely long cylinder in the axial direction, the anode current I_b is given by

$$I_\mathrm{b} = |\boldsymbol{J}(r,\theta)|S = en\langle \boldsymbol{v}(r,\theta)\rangle S, \tag{3.16}$$

where e is the electron charge, n is the number of electrons reaching the anode, $\langle \boldsymbol{v}\rangle$ is the mean velocity of electrons when they reached the anode, and S is the surface area of the anode. Here, the axial velocity component $\langle v(z)\rangle$ is independent of I_b.

In terms of $\langle \boldsymbol{v}\rangle$, the azimuthal component $\langle v(\theta)\rangle$ is dominant, and $\langle v(\theta)\rangle$ is expressed in the simplest way [63] by the $\boldsymbol{E}\times\boldsymbol{B}$ drift velocity, then

$$|\langle v(\theta)\rangle| = \frac{|\langle E_\mathrm{r}\rangle|}{B}, \tag{3.17}$$

where $\langle E_\mathrm{r}\rangle$ is the mean electrostatic field in the radial direction and B is the external field in the axial direction. Also, $\langle v(\theta)\rangle$ is related to the π-mode oscillation frequency f expressed by

$$f = \frac{|\langle v(\theta)\rangle|}{2\pi r_\mathrm{a}}\frac{N}{2}, \tag{3.18}$$

where r_a is the anode radius, and N is the number of the anode vanes.

Here we approximate that f is expressed as a linear function of I_b from the experimental results of the frequency pushing shown in Fig. 3.7 and Fig. 3.8, then we can derive experimental formula

$$f = \begin{cases} (1.15\times10^7\ \mathrm{Hz/A})\times I_\mathrm{b} + (2.45\times10^9\ \mathrm{Hz}), & 0.186\mathrm{A} \le I_\mathrm{b} < \max\{I_\mathrm{b}\} \\ (6.55\times10^8\ \mathrm{Hz/A})I_\mathrm{b} + (2.33\times10^9\ \mathrm{Hz}), & 0 \le I_\mathrm{b} < 0.186\mathrm{A} \end{cases}. \tag{3.19}$$

Then, in the case of the reference magnetron, the relationship between I_b and $\langle v(\theta) \rangle$ is experimentally derived from Eq. (3.18) and Eq. (3.19),

$$\langle v(\theta) \rangle = \begin{cases} (6.50 \times 10^4 \text{ m/s/A}) \times I_b + (1.39 \times 10^7 \text{ m/s}) & 0.186\text{A} \leq I_b < \max\{I_b\} \\ (3.70 \times 10^6 \text{ m/s/A}) \times I_b + (1.32 \times 10^7 \text{ m/s}) & 0 \leq I_b < 0.186\text{A} \end{cases} \tag{3.20}$$

Note that Eq. (3.16) conflicts with Eq. (3.20) if I_b is a function of $\langle v(\theta) \rangle$, because I_b is proportional to $\langle v(\theta) \rangle$ in Eq. (3.16); on the other hand, I_b is dominantly determined by the constant on the right-hand side in Eq. (3.20). Therefore, it is verified that the anode current is mainly dependent on the number of electrons n, and independent of the velocity $\langle \boldsymbol{v} \rangle$ in Eq. (3.16).

Variation of the potential minimum in the constant-voltage range

Now we are considering that a magnetron is operated in the interval between the start-up and the constant-voltage range. In other words, the anode current varies from almost 0A up to 0.4A in this range. Then, the position of the potential minimum moves from about 7% of the distance between the anode and the cathode to nearly the cathode with changes in the potential minimum, as the anode current increases, shown in Table 3.2. Thus, the electric potential distribution in the radial direction drastically changes as well as the electron density, because an abundance of electrons flows from the space charge region to the interaction region in the constant-voltage range. Therefore, these drastic variations of both the potential and the electron density have a possibility to generate electrostatic noises by interaction with each other, independently of the microwave oscillation.

Axial oscillation of electrons

Here we suggest an axial oscillation of electrons, which is attributed to the axial electrostatic field E_z due to the existence of the end hats. The suggested axial oscillation is originally derived from the axial oscillation of nonneutral plasma in a Penning trap [64, 65]. First, the axial oscillation in a Penning trap is first described, then the axial oscillation in a magnetron is discussed by analogical extension of the Penning trap case.

A Penning trap is a device to trap charged particles by a static electromagnetic field. A typical cross-section view of a Penning trap in the $r - z$ plane is shown in Fig 3.18. In the Penning trap, the magnetic field is applied in the axial direction. Besides, there are two end caps and a ring electrode in the Penning trap, and the DC potential difference between the end caps and the ring electrode is V, then the electrostatic field in the Penning trap is depicted as shown in Fig 3.18. Thus, motion of particles, which are put around the origin of coordinates in Fig 3.18, is confined not only in the r direction by the axial magnetic field, but also in the z direction by the axial electrostatic field formed by the end caps and the ring electrode.

In an ideal Penning trap, both two end caps and a ring electrode have hyperbolic surfaces. Hence, the electric potential distribution $\phi(r, z)$ is approximately given by a quadrupole potential as the following expression;

$$\phi(r, z) = V\frac{2z^2 - r^2}{2L^2 + b^2}, \tag{3.21}$$

where $2L$ is the axial distance between the end caps and b is the radius of the ring electrode [64]. Therefore, the axial electrostatic field $E_z(z)$ at $r = 0$ is given by differentiating Eq. (3.21) with respect to z;

$$E_z(z) = \left.\frac{\partial\phi(r, z)}{\partial z}\right|_{r=0} = \frac{4zV}{2L^2 + b^2}. \tag{3.22}$$

Fig 3.19 shows a curve of the axial electrostatic field at $r = 0$.

Axial motion of a single electron is given by the equation of motion where $\boldsymbol{v} \times \boldsymbol{B} = 0$;

$$m\frac{d^2z}{dt^2} = -eE_z. \tag{3.23}$$

Then, substituting Eq. (3.22) for Eq. (3.23), we can obtain

$$\frac{d^2z}{dt^2} + \frac{4eV}{m(2L^2 + b^2)}z = 0. \tag{3.24}$$

Eq. (3.24) expresses the equation of simple harmonic motion, hence, the axial motion of the electron in the Penning trap is expressed as a bouncing motion with a harmonic frequency

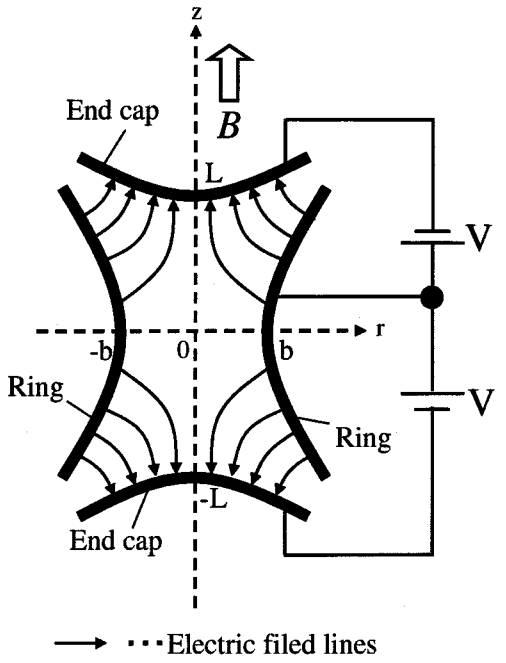

Figure 3.18: Cross-section view of a Penning trap in the $r - z$ plane.

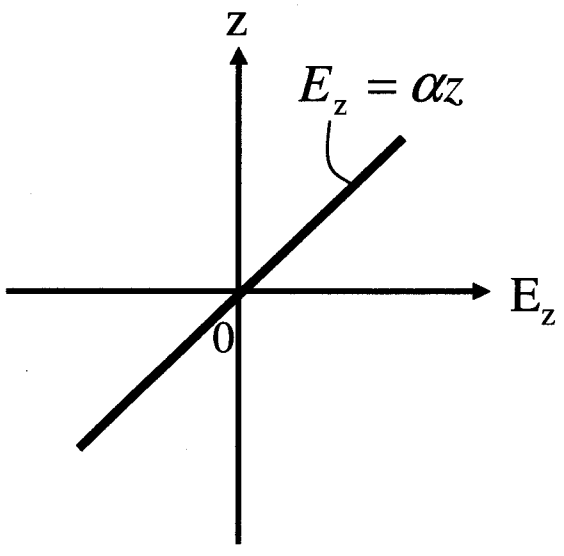

Figure 3.19: Axial electrostatic field at $r = 0$ in an ideal Penning trap. $\alpha = 4V/(2L^2 + b^2)$.

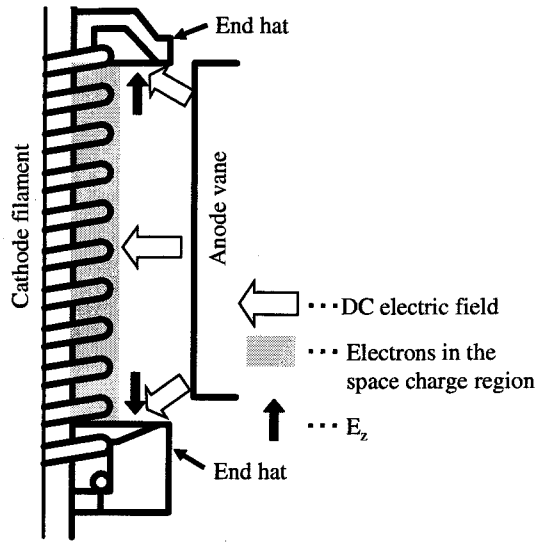

Figure 3.20: End hat effect on the DC electric field in a magnetron. The axial electrostatic field E_z begins to emerge near both the cathode filament ends.

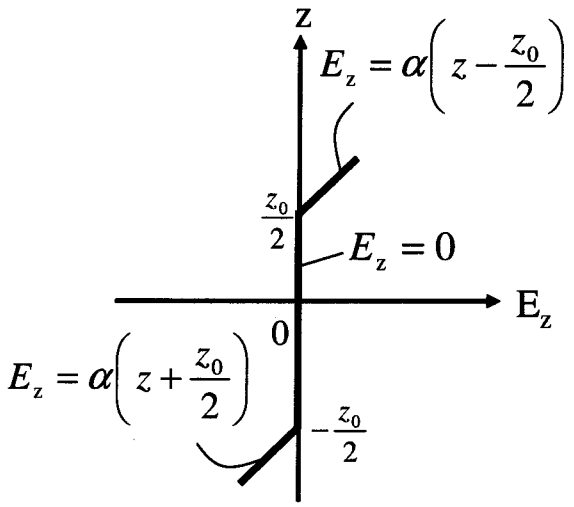

Figure 3.21: Hypothetical axial electrostatic field at $r = 0$ in a magnetron.

of f_z;

$$f_z = \frac{\omega_z}{2\pi} = \frac{1}{2\pi}\sqrt{\frac{4eV}{m(2L^2 + b^2)}}. \tag{3.25}$$

Now, we analogically expand the axial oscillation frequency in the Penning trap to that in a magnetron. Fig. 3.20 shows a typical cross-section view of a magnetron in the $r - z$ plane. A magnetron also has the axial magnetic field, two end hats and anode vanes instead of two end caps and a ring electrode in a Penning trap, respectively. Besides, the axial electrostatic field E_z begins to emerge near both the cathode filament ends due to the existence of the end hats, as shown in Fig. 3.20, when the anode voltage is applied. Hence, there is a possibility for an electron to oscillate in the axial direction in the magnetron as well as the Penning trap.

Here, we address only the axial motion of an electron, omit the radial and azimuthal motion, and we assume that the axial electrostatic field in a magnetron is expressed as the following

$$E_z(z) = \begin{cases} \alpha\left(z - \frac{z_0}{2}\right), & \left(z \geq \frac{z_0}{2}\right) \\ 0, & \left(-\frac{z_0}{2} \leq z \leq \frac{z_0}{2}\right) \\ \alpha\left(z + \frac{z_0}{2}\right), & \left(z \leq -\frac{z_0}{2}\right) \end{cases}, \tag{3.26}$$

as the curve of the axial electrostatic field is shown in Fig. 3.21.

Then, the axial motion of electrons is divided into two parts; simple harmonic motion and uniform linear motion. With regard to the simple harmonic motion, substituting $\sqrt{\alpha}$ for

$\sqrt{4V/(2L^2+b^2)}$ of Eq. (3.25), a time period of the simple harmonic motion T_z is given by

$$T_z = \frac{1}{f_z} = 2\pi\sqrt{\frac{m}{e\alpha}}. \tag{3.27}$$

With regard to the uniform linear motion, we assume that an electron travels back and forth between $-z_0/2$ and $z_0/2$ with a velocity of v_0, then a time period of the uniform linear motion T_u is equal to $2z_0/v_0$.

Finally, we obtain the axial oscillation frequency f'_z in a magnetron;

$$f'_z = \frac{1}{T_u + T_z} = \frac{1}{2z_0/v_0 + 2\pi\sqrt{m/e\alpha}}. \tag{3.28}$$

Now we roughly estimate the axial oscillation frequency f'_z with parameters of the reference magnetron. The electrostatic field intensity $|\boldsymbol{E}|$ in the reference magnetron is the order of 10^6V/m since the gap between the cathode and anode is the order of 10^{-3}m and the anode voltage is the order of kV. Then, the axial electrostatic field is expressed by $|\boldsymbol{E}|\cos\theta$, where θ is an angle between the vector $\boldsymbol{E}$ and the z axis. Hence, we can assume α as the order of $10^5 \sim 10^6$V/m unless θ is almost the right angle. Hence, T_z is calculated to be the order of 10^{-8}s. In terms of v_0, the velocity of the axial diffusive motion described in Sec. 2.2 is applied. The axial diffusive length and the traveling time of a single electron in the cylindrical diode are the order of 10^{-3}m and 10^{-10}s, respectively, so that v_0 is roughly estimated to be the order of 10^{-7}m/s. As z_0 is the order of 10^{-3}m, T_u is finally estimated to be the order of 10^{-10}s. Therefore, f'_z can be approximately rewritten by

$$f'_z \sim \frac{1}{T_z} = \frac{1}{2\pi}\sqrt{\frac{\alpha e}{m}}. \tag{3.29}$$

When $\alpha = 10^5 \sim 10^6$V/m^2, for example, f'_z is calculated to be $= 21 \sim 67$MHz. Therefore, the axial oscillation at a frequency of the order of several tens of MHz has a great possibility to take place in a magnetron, if the axial electrostatic field is expressed as Eq. (3.26). Although the axial electrostatic field in practice may be different from Eq. (3.26), some axial bouncing motion will take place in a magnetron since the axial electrostatic field is applied in the direction where electrons are trapped in both the space charge region and the interaction region.

In conclusion, the variation of the potential minimum and the axial oscillation of electrons could be regarded as one of noise sources in the constant-voltage range. Especially, the axial oscillation of electrons has a great possibility to take place in the low frequency bands.

3.6 Summary

In this chapter, a time domain analysis of magnetron noises is carried out. The results indicate that spurious noises generated from a magnetron are classified into the following five types;

(1) Side band noises around the carrier and low frequency line noises at frequencies below about 150MHz, generated at an anode current of less than 0.2A.

(2) High frequency spurious noises and low frequency line noises generated in the transition region between the constant voltage range and the non-constant voltage range at an anode current of around 0.4A.

(3) Low frequency line noises generated in the non-constant voltage range characterized by frequencies of 400MHz or 800MHz, and high frequency spurious noises generated at an anode current of around 0.6A, attributed to the intermodulation of the low frequency line noises and the harmonics.

(4) The harmonics generated in synchrony with the fundamental.

(5) Low frequency line noises generated in synchrony with the electron circulation.

The noises at frequencies below 150MHz assigned to the type (1) are generated in a low anode current operation. Ion relaxation oscillation might be a source of these noises. However, ion plasma oscillation is unlikely to take place because the neutral plasma conditions are hardly satisfied in a magnetron. The detailed time domain analysis suggests that sudden irregular motion of electrons and distortion of the microwave field due to discontinuity at the start-up of the oscillation are also possible noise sources of the type (1).

Most of the high frequency spurious noises other than the harmonics and most of the low frequency line noise are assigned to the type (2). Also, in the transition region, the operating characteristics of the magnetron change from the constant voltage range to the non-constant voltage range. Therefore, noise generation factors for the type (2) are likely to be irregular motion of electrons generated by changes in the space charge conditions in the magnetron and distortion of the microwave fields. An important subject for the future is a theoretical study on the characteristics of a magnetron, and investigation of a magnetron design that can suppress spurious noises in the transition region.

A generation mechanism of noises assigned to the type (3) has not been clear yet. Since these noise levels are higher than the other types, there is a strong probability that they are generated by satisfaction of resonance conditions or oscillation conditions other than the fundamental oscillation. If these resonance conditions or oscillation conditions are satisfied, spurious noises would be generated at frequencies following the selectional rules of the resonance conditions.

The generation of the noises assigned to the type (5) is unavoidable since these noises are generated by the primary behavior of a magnetron as well as the harmonics classified in the type (4).

In addition, relatively high level noise generation in the various frequency bands occurs continuously in the interval from the start-up of the oscillation to the constant voltage range, as seen in the video output shown in Fig. 3.6. These noises are considered to be generated

by the variation of the potential minimum vibration and the axial oscillation of electrons. Especially, the axial oscillation of electrons has a great possibility to take place in the low frequency bands.

As described above, it has been found possible to categorize the magnetron noises according to the generating frequencies. Also, the generation mechanisms of the categorized noises are likely to be different from each other. Hence, it will be a beneficial way to deal with these classified noises independently for the purpose of developing a low noise magnetron.

Note that some assumptions and approximations are employed in the discussions of noise sources of a magnetron for ease of explanation in this chapter. However, a practical magnetron has much more complexities of a structure, motion of electrons, charge density distribution, the static electromagnetic field and the RF electromagnetic field. Hence, it is near-impossible to derive noise sources of a magnetron analytically from mathematical formula in consideration of these complexities with three-dimensional aspects. Therefore, three-dimensional analysis of a magnetron with computer simulations will play an extremely important role in researching and identifying generation mechanisms of magnetron noises.

Chapter 4

Newly-Designed Low Noise Magnetrons

4.1 Introduction

In this chapter, we describe an experimental study of newly-designed low noise magnetrons for the purpose of the reduction of spurious noises even when it is operated in a microwave oven system. A development of a future low noise magnetron will contribute not only to cost reduction of a microwave oven by uninstalling filter circuits, but also to the realization of EMC with broadcast communications such as radio in the MF bands and television in the VHF and UHF bands, and IT communications such as wireless LAN, without installing the filter circuits. We have conducted two approaches for the reduction of the spurious noises by the newly-designed low noise magnetrons.

One approach is the modification of the interaction space and the anode voltage, described in Sec. 4.2. The interaction space means the gap between the cathode and the anode. With regard to the modification of the anode voltage, Brown has shown the experimental results that the signal to noise level was improved by decreasing the anode voltage when a magnetron is operated by a DC stabilized power supply [41]. In this thesis, we conducted experimental measurements not only for the fundamental spectrum but also for spurious noises in the high frequency bands and the low frequency bands.

The other approach is to mount cylindrical metallic cathode shields, which are axially installed on the ends of the cathode filament, to a magnetron, described in Sec. 4.3. With regard to the cathode shield, Kohsaka *et al.* [5] has suggested a magnetron with cathode shields on both the RF output side and the HV input side in order to suppress electron emission from the end portions of the cathode, although any details except schematics of the magnetron with cathode shields was not described. In this thesis, we have conducted experimental measurements of spurious noises generated from two types of magnetrons with cathode shields; a magnetron on both the RF output side and the HV input side, which is

similar to that of the Kohsaka's suggestion, and a magnetron which has a cathode shield only on the HV input side, which we originally design.

4.2 Modifications of the interaction space and the anode voltage

4.2.1 Configurations of magnetrons

In the present section, the interaction space and the anode voltage of a magnetron are treated as parameters. The interaction space means the gap between the cathode and the anode. Each parameter is set in three stages: the interaction space of 2.2mm, 2.4mm and 2.525mm and the anode voltage of 2.6kV, 3.6kV and 4.6kV. Hence, 9 types of modified magnetrons are manufactured for the experiments. The numbering table of the modified magnetrons is put in Table 4.1. The external magnetic field of each modified magnetron is adjusted by replacing permanent magnets, so as to conform the oscillating frequency to that of the reference magnetron 2M210M1F1.

Table 4.1: Numbering table of modified magnetrons. The reference magnetron 2M210M1F1 has the interaction space of 2.525mm and is operated at the anode voltage of 4.1kV.

Anode Voltage (e_{bm})	Interaction space		
	2.2mm (A)	2.4mm (B)	2.525mm (C)
4.6kV (1)	No.A-1	No.B-1	No.C-1
3.6kV (2)	No.A-2	No.B-2	No.C-2
2.6kV (3)	No.A-3	No.B-3	No.C-3

4.2.2 Measurement system

A schematic of a measurement system is shown in Fig. 4.1. It is almost the same as that for the measurement system of the time domain analysis, as described in Chapter 3. A magnetron is operated by a half-wave voltage doubler. The anode current and the filament voltage are fixed at 400mA and 3.3V, respectively, for all the modified magnetrons. The measurement is conducted in the condition that the feedthrough capacitor and the choke coil attached to the magnetron are removed, in order to detect all spurious noises generated from the magnetron itself as much as possible.

A measuring range of the spectrum is divided into three: 2.35GHz-2.55GHz for the fundamental, 4GHz-14GHz for high frequency spurious noises, and 100kHz-1GHz for low frequency line noises. In the fundamental frequency bands and the high frequency bands, leakage electromagnetic waves are measured with a spiral antenna and a horn antenna, respectively. In the low frequency bands, line noises on cables between the magnetron and the half-wave

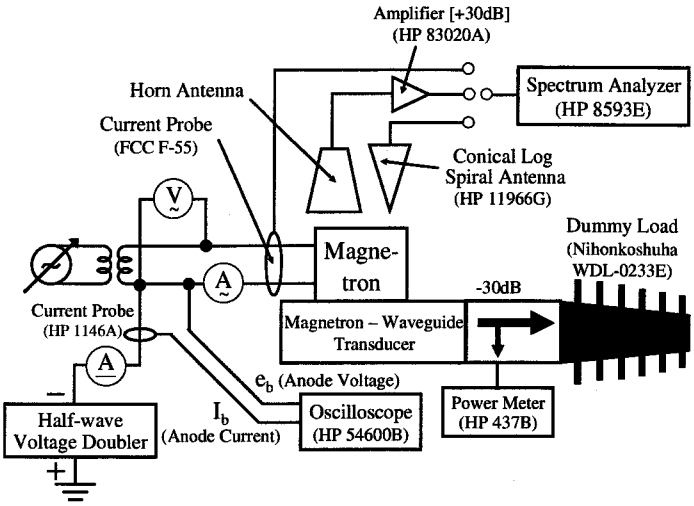

Figure 4.1: Schematic of a measurement system for newly-designed magnetrons.

voltage doubler are measured with a current probe. Since these measurements are not those for the spectrum radiated from the magnetron output, one cannot derive the absolute value of the spectral intensity radiated from the RF output. However, since the main objective of the present research is relative comparisons of the modified magnetrons with each other, an easier method shown in Fig 4.1 is adopted.

The spectrum in each frequency band is measured with a spectrum analyzer (HP 8593E). In the present experiment, the maximum value of the spectrum is held on the spectrum analyzer during a period of one minute when the magnetron and the waveguide are thermally stable. Thus, the spectrum analyzer displays the envelope of the maximum levels of the spectra generated from the measured magnetron. Settings of the resolution bandwidth and the video bandwidth of the spectrum analyzer are put in Table 4.2.

Table 4.2: Settings of the spectrum analyzer. RBW: resolution bandwidth, VBW: video bandwidth

Frequency span	RBW	VBW
4GHz-14GHz	1MHz	10kHz
2.35GHz-2.55GHz	10kHz	10kHz
100kHz-1GHz	100kHz	10kHz

4.2.3 Experimental results

Experimental results of the modified magnetrons in the fundamental bands (2.35GHz–2.55GHz), the high frequency bands (4GHz–14GHz), and the low frequency bands (100kHz–1GHz) are shown in Fig 4.2, Fig 4.3, and Fig 4.4, respectively.

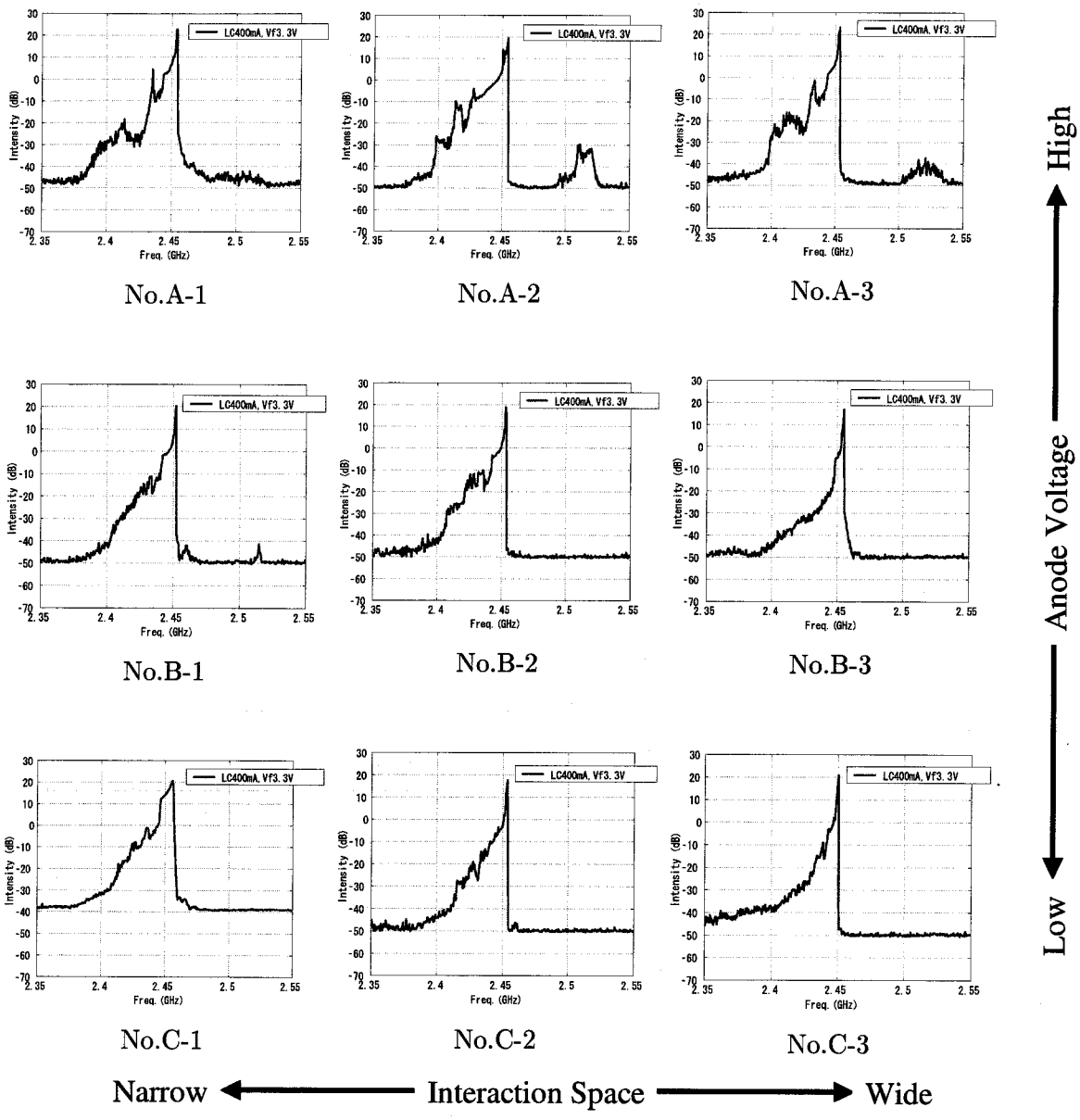

Figure 4.2: Measurement results of the magnetrons by the modifications of the interaction space and the anode voltage in the fundamental bands (2.35GHz–2.55GHz).

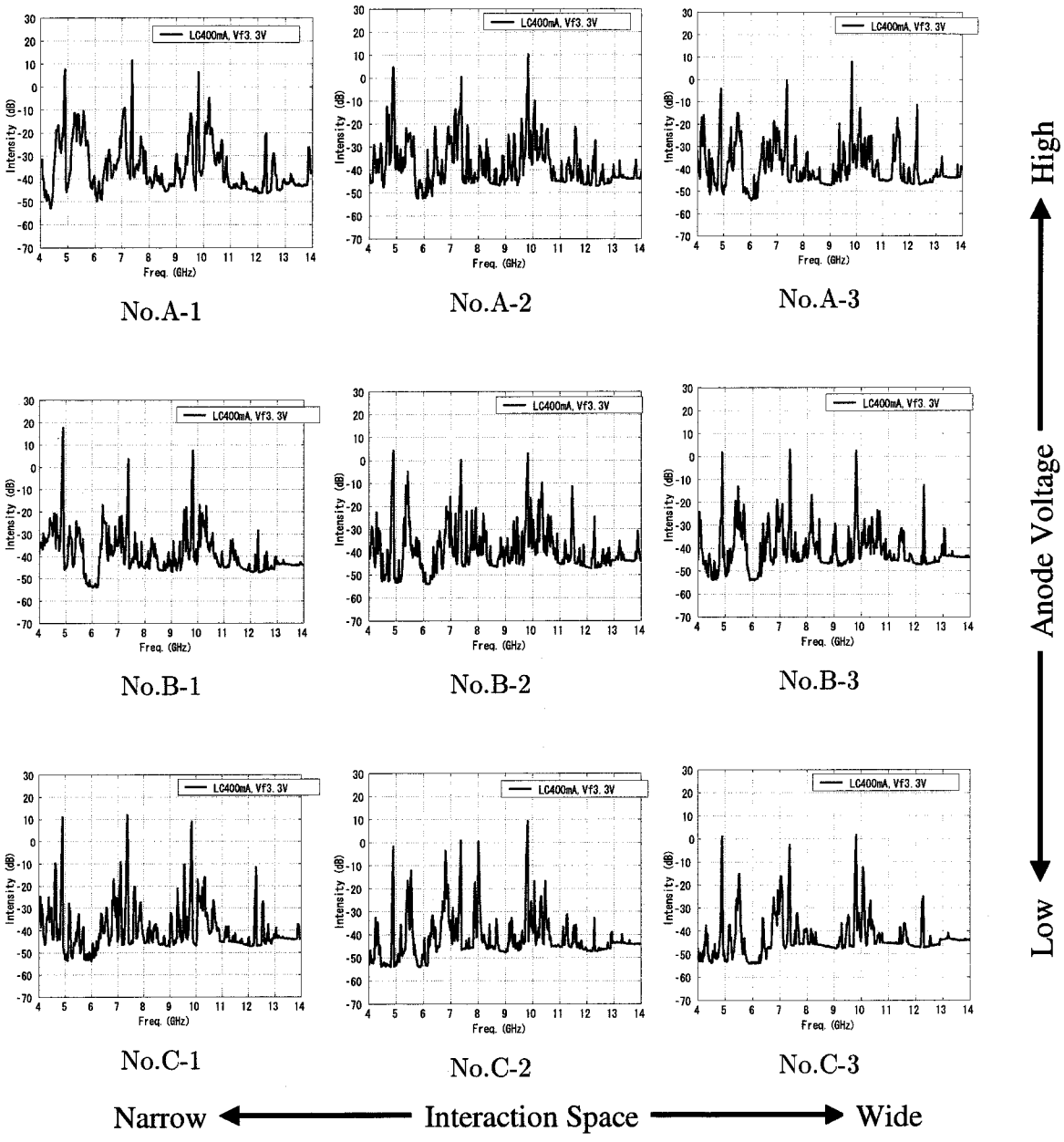

Figure 4.3: Measurement results of the magnetrons by the modifications of the interaction space and the anode voltage in the high frequency bands (4GHz–14GHz).

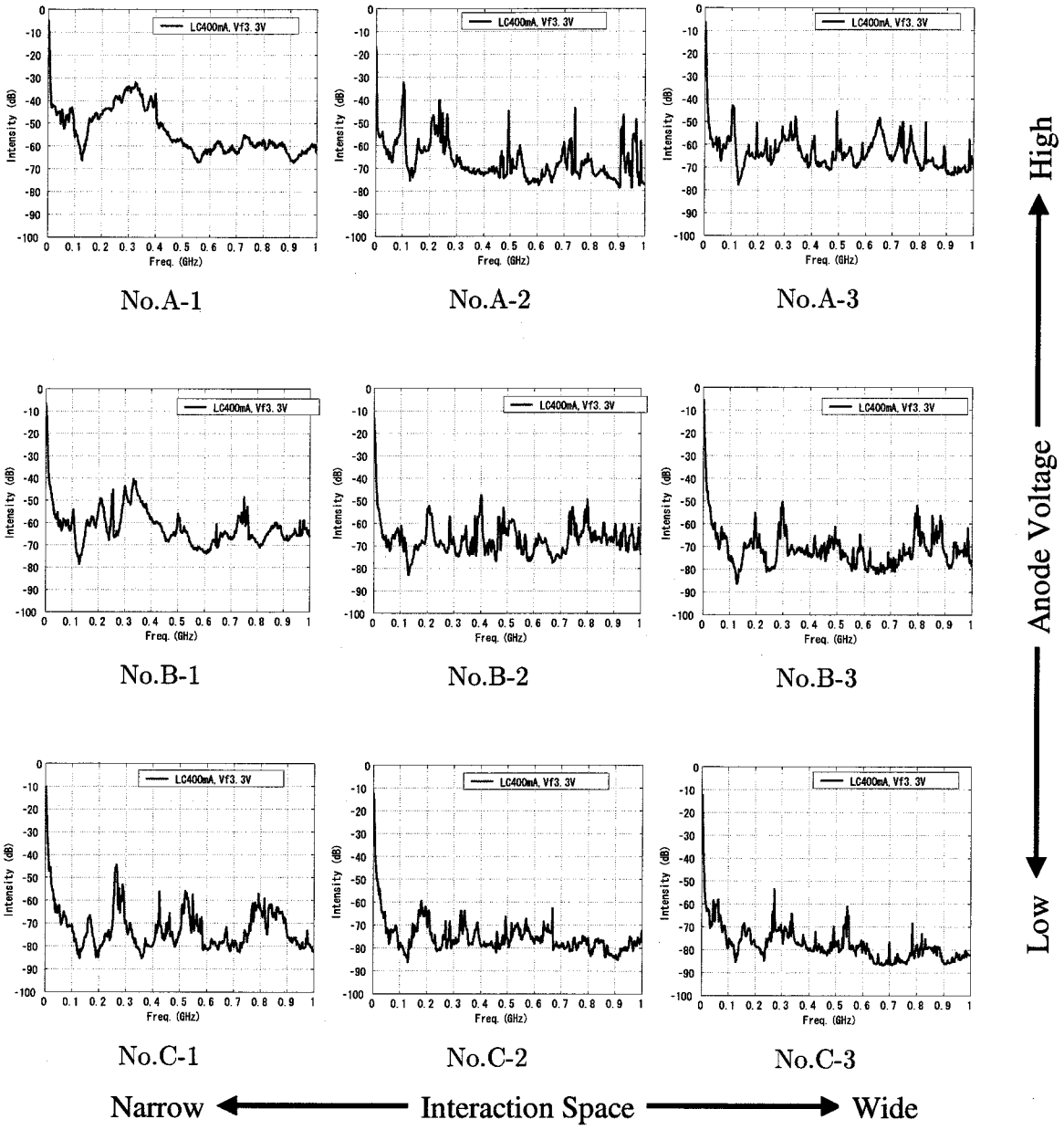

Figure 4.4: Measurement results of the magnetrons by the modifications of the interaction space and the anode voltage in the low frequency bands (100kHz–1GHz).

From the experimental results, there are two tendencies with respect to the reduction of spurious noises. One is that the lower the anode voltage, the lower the spurious noise levels. The other is that the wider the interaction space, the lower the spurious noise levels. The former tendency is more potent than the latter from the results.

4.2.4 Discussions

Now we discuss what causes the noise reduction or the noise enhancement by the modification of the interaction space and the anode voltage.

Position of the potential minimum

First, we consider the position of the potential minimum x_{m} from Eq. (3.3), which we have already described in Sec 3.5.

We substitute the Richardson-Dushman's equation Eq. (2.21) for Eq. (3.3), then

$$\begin{aligned} x_{\mathrm{m}} &= (2.78\times10^{-6}\ \mathrm{A^{\frac{1}{2}}K^{-\frac{3}{4}}})\sqrt{\frac{S_{\mathrm{a}}}{I_{\mathrm{b}}}}T^{\frac{3}{4}} \\ &\quad -(1.54\times10^{-6}\ \mathrm{A^{\frac{1}{2}}K^{-\frac{3}{4}}})\times\sqrt{\frac{I_{\mathrm{b}}S_{\mathrm{a}}}{SA}}T^{-\frac{1}{4}}\exp\left(\frac{e\phi}{2kT}\right). \end{aligned} \tag{4.1}$$

In these experiments, the anode current I_{b} is fixed to 400mAdc. S_{a} is equal to $2\pi r_{\mathrm{a}}h$, where h is the height of the anode, if a magnetron is assumed to be a perfect cylinder. Then we substitute $A = 0.97\times10^{4}\mathrm{A/m^2/K^2}$, $\phi = 2.18\mathrm{eV}$, $I_{\mathrm{b}} = 400\mathrm{mA}$ and the actual dimension of the reference magnetron $h = 9.5\mathrm{mm}$ for Eq. (4.1), then

$$\begin{aligned} x_{\mathrm{m}} &= (1.07\times10^{-6}\ \mathrm{m^{\frac{1}{2}}K^{-\frac{3}{4}}})\times\sqrt{r_{\mathrm{a}}}T^{\frac{3}{4}} \\ &\quad -(9.89\times10^{-9}\ \mathrm{mK^{\frac{1}{4}}})\times\sqrt{\frac{r_{\mathrm{a}}}{r_{\mathrm{c}}}}T^{-\frac{1}{4}}\exp\left\{\frac{(1.26\times10^{4}\ \mathrm{K})}{T}\right\}. \end{aligned} \tag{4.2}$$

Therefore, it is clear that x_m is independent of the anode voltage V.

Here we substitute $T = 2000\mathrm{K}$, the filament temperature at I_{b} =400mA from Table 3.2, as an example. Then Eq. (4.2) becomes

$$x_{\mathrm{m}} = (3.20\times10^{-4}\ \mathrm{m^{\frac{1}{2}}})\times\sqrt{r_{\mathrm{a}}} - (8.05\times10^{-7}\ \mathrm{m})\times\sqrt{\frac{r_{\mathrm{a}}}{r_{\mathrm{c}}}}. \tag{4.3}$$

In the magnetrons we examined in this section, the first term on the right-hand side of Eq. (4.2) is about ten times larger than the second term. Hence, Eq. (4.2) approximately becomes

$$x_{\mathrm{m}} \sim (3.20\times10^{-4}\ \mathrm{m^{\frac{1}{2}}})\times\sqrt{r_{\mathrm{a}}}. \tag{4.4}$$

Note that x_{m} is at most the order of 10^{-5}m because r_{a} is the order of 10^{-3}m. Besides, the variation of r_{a} is less than 10% in the magnetrons of which we modified the interaction space. Then, x_{m} is almost independent of r_{a}.

After all, it can be concluded that the position of the potential minimum is independent of both the interaction space and the anode voltage.

Relation with the interaction space

From the discussion above, it is obvious that the wider the interaction space, the wider the distance between the anode and the position of the potential minimum. From the discussion in Sec 3.5, one of the noise sources is the interaction between the RF electromagnetic field, which is generated on the anode vanes, and the motion of electrons in the space charge region. Therefore, noise reduction by expansion of the interaction space will be attributable to reduced interaction between the RF field and the electrons in the space charge region, for the anode vanes are away from the electrons in the space charge region.

Relation with the anode voltage

In the present experiments, the anode current is fixed at 400mA so that both the DC input power and the RF output power, *i.e.* the total energy systems in the magnetrons, depend on the anode voltage. The decreasing level of the total energy system is at most -3dB at an anode voltage of 2.6kV compared to 4.6kV. However, note that the peak values of the spectra in the fundamental bands shown in Fig 4.2 seem to be independent of the variation of the anode voltage. On the other hand, the noise reduction levels in various frequencies exceeds several times more than the energy decreasing levels, as shown in Fig 4.3 and Fig 4.4. Therefore, the noise reduction by the modification of the anode voltage is not attributed to the relative reduction of the total energy system. As a cause for the noise reduction, drastic changes of behaviors in the magnetrons are considered, such as the reduction of initial potential energy of electrons, the falloff of the filament temperature owing to the reduction of the back bombardment energy, and the electrostatic field in the magnetron which is described in the next paragraph, etc.

Relation with the electrostatic field and the external magnetic field

These tendencies can be simply put together in light of the electrostatic field. Assuming that a magnetron is a infinitely-long cylindrical diode, when the charge density λ per unit length is uniformly distributed at the cathode with a radius of r_c, the radial electrostatic field E_r at the radial position of r is derived from the Gauss's law;

$$E_r = \frac{\lambda}{2\pi\varepsilon_0 r}. \tag{4.5}$$

Then, the anode voltage V is given by

$$V = -\int_{r_c}^{r_a} E_r = \frac{\lambda}{2\pi\varepsilon_0} \log\frac{r_a}{r_c}, \tag{4.6}$$

where r_a is the anode radius. From Eq. (4.5) and Eq. (4.6),

$$E_r = \frac{V}{r\log(r_a/r_c)}. \tag{4.7}$$

Table 4.3: Theoretical radial electrostatic field on the cathode ($r = r_c$) when the modified magnetrons are assumed as infinitely-long cylindrical diodes. The numbers in the brackets are sorted in descending order of the radial electrostatic field.

$r = r_c$	Interaction space		
Anode Voltage (e_{bm})	2.2mm	2.4mm	2.525mm
4.6kV	7.4×10^6 V/m (1)	6.8×10^6 V/m (2)	6.5×10^6 V/m (3)
3.6kV	5.8×10^6 V/m (4)	5.3×10^6 V/m (5)	5.1×10^6 V/m (6)
2.6kV	4.2×10^6 V/m (7)	3.9×10^6 V/m (8)	3.7×10^6 V/m (9)

Table 4.4: Theoretical radial electrostatic field on the anode ($r = r_a$) when the modified magnetrons are assumed as infinitely-long cylindrical diodes. The numbers in the brackets are sorted in descending order of the radial electrostatic field.

$r = r_a$	Interaction space		
Anode Voltage (e_{bm})	2.2mm	2.4mm	2.525mm
4.6kV	3.3×10^6 V/m (1)	3.0×10^6 V/m (2)	2.9×10^6 V/m (3)
3.6kV	2.6×10^6 V/m (4)	2.4×10^6 V/m (5)	2.2×10^6 V/m (6)
2.6kV	1.9×10^6 V/m (7)	1.7×10^6 V/m (8)	1.6×10^6 V/m (9)

Then, the radial electrostatic fields of the modified magnetrons at the radii of the cathode $r = r_c$ and the anode $r = r_a$ are calculated from Eq. (4.7), as shown in Table 4.3 and Table 4.4. Note that the numbers in the brackets are sorted in descending order of the electrostatic field of the modified magnetrons. When the order of the number in the bracket in Table 4.3 and Table 4.4 is compared to the figures of the spectra as shown in Fig 4.2, Fig 4.3 and Fig 4.4, the spurious noises are likely to be relatively reduced as the radial electrostatic field weakens.

Note that the magnetrons we examined in this section oscillate at almost the same frequency as shown in Fig 4.2. Since the oscillating frequency is simply determined by the azimuthal $\boldsymbol{E} \times \boldsymbol{B}$ drift velocity $|\langle v_\theta \rangle| = |\langle E_r \rangle|/B$, $|\langle E_r \rangle|/B$ is almost the same in the modified magnetrons. Therefore, the order of the numbers in the brackets in Table 4.3 is also applicable to the external magnetic field B.

Now we consider the electron density in the space charge region from Eq. (3.6) described in Sec. 3.5. The radius r in Eq. (3.6) is comparable to r_c, since the width of the space charge region is only a few percent of the interaction space in the magnetron operation, as described in Sec. 3.5. Then, substituting $r \sim r_c$ for Eq. (3.6), the amount of the electron density $|\rho_e|$ approximately reduces to be

$$|\rho_e| \sim \left|\varepsilon_0 \frac{eB^2}{m}\right|. \tag{4.8}$$

Thus, the amount of the charge density is estimated to increase as the anode voltage increases and the interaction space decreases, since the magnetic field is also estimated to increase in the ascending order of the numbers in the brackets in Table 4.3 and Table 4.4. As described in Sec. 3.5, a large amount of electrons in the space charge region could be a noise source of a magnetron in the constant-voltage range. Therefore, noise levels will be enhanced as the amount of electrons increases in the space charge region.

In conclusion, spurious noises are suppressed as the anode voltage decreases and the interaction space widens. The reduction of the spurious noises is attributed to (1) the reduced interaction between the RF field and the motion of electrons in the space charge region, (2) the decrease of the total energy, (3) the reduction of noises generated by an abundance of electrons in the space charge region due to the reduced external magnetic field. Although the decrease of the external magnetic field also degrades the DC-RF conversion efficiency, which we will describe in Sec. 5.5, it is demonstrated that these modifications of the magnetrons work effectively for the reduction of the spurious noises.

4.3 Magnetrons with cathode shields

The experimental results of the axial filament temperature shown in Fig. 2.13 indicate that the temperature falloff was not so drastic at the center of the cathode; on the contrary it was quite drastic on both the filament ends, especially on the RF output side, when the filament current is turned off during the oscillation. Also, we briefly introduced in Sec 2.1 that spurious noises around the carrier frequency bands of a magnetron were suppressed by the internal feedback mechanism, which takes place most effectively when the filament current is turned off [41, 51]. Therefore, the spurious noises from the magnetron might be suppressed without turning off the filament current, if the same axial distribution of the filament temperature is artificially created as that in the oscillating state with the internal feedback mechanism, shown in Fig. 2.13 ($I_b = 400$mA, $I_f = 0$A).

As a method to make it, a magnetron proposed by Kohsaka *et al.* [5] is referred. The magnetron has cathode shields on both the RF output side and the HV input side in order to suppress the electron emission from the end portions of the cathode. Although any details except schematics of the magnetron with cathode shields was not described, the experimental results shown in Chapter 2 strongly support that Kohsaka's approach would be quite reasonable. Moreover, Fig. 2.4 and Fig. 2.13 point out that a cathode shield on the RF output side is not so effective to prevent electron emission because the electron emission there is essentially less than that at the center, or even the HV input side of the examined magnetron.

We have therefore designed a new type of a magnetron with a cathode shield only on the HV input side. Here we describe effects on the reduction of spurious noises generated from newly-designed low noise magnetrons with cathode shields.

4.3.1 Configurations of magnetrons

Fig. 4.5 shows inside schematics of the reference magnetron (Fig. 4.5 (a)), a magnetron with cathode shields on both the filament ends (Fig. 4.5 (b)), and a magnetron with a cathode shield only on the HV input side (Fig. 4.5 (c)). The structure of the magnetron (b) is almost similar to that of the magnetron depicted by Kohsaka *et al.* [5], and the metallic cathode shields are directly connected with both the end hats. The structure of the magnetron (c) is a newly-designed one based on the experimental results described in Chapter 2, and the metallic cathode shield is directly connected only with the end hat on the HV input side.

The electron emission areas of the cathode filament of the magnetron (b) and (c) are smaller than the reference magnetron (a), because parts of the cathode filament are covered with cathode shields. The axial length of the cathode shield fit in the magnetron (c) is the same as the sum of the axial lengths of two pieces of cathode shields fit in the magnetron (b), in order to conform the electron emission areas of the magnetron (b) to that of the magnetron (c). In terms of the other parameters, such as radii of both the anode and the cathode, the anode shape, the external magnetic field etc., there is no difference among the three types of the magnetrons.

With regard to the measurement system, we used the same system as that shown in Fig 4.1.

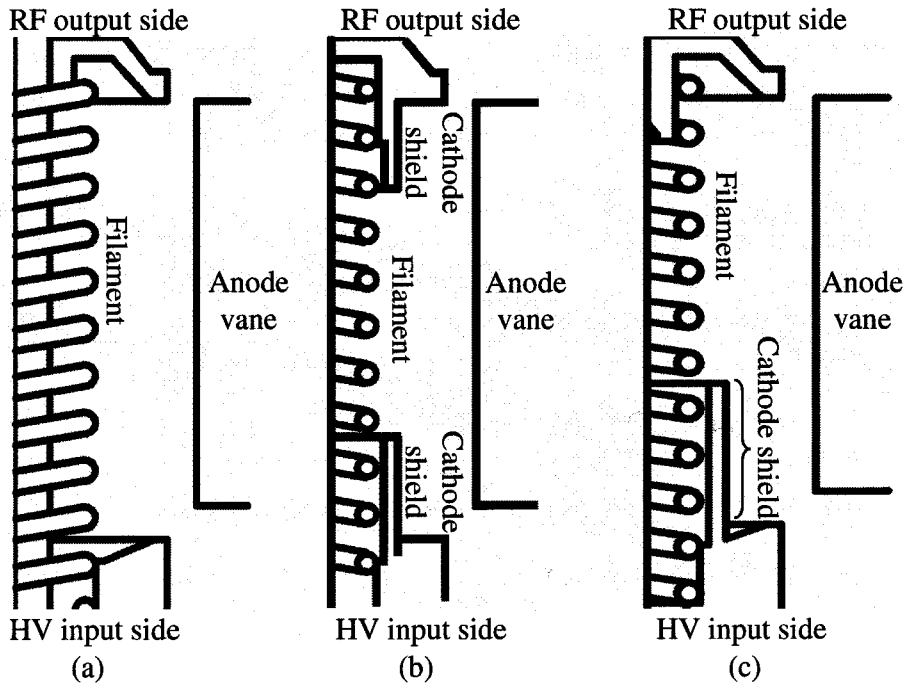

Figure 4.5: Inside schematics of (a) the reference magnetron, (b) a magnetron with cathode shields on both the filament ends and (c) a magnetron with a cathode shield on the HV input side.

4.3.2 Experimental results

Experimental results of the fundamental spectrum, high frequency spurious noises, and low frequency line noises are shown in Fig. 4.6. The spectra of the reference magnetron, the magnetron with cathode shields on both the filament ends, and the magnetron with a cathode shield on the HV input side are plotted in Fig. 4.6 (a), Fig. 4.6 (b) and Fig. 4.6 (c), respectively. The normal rated filament voltage of 3.3V remains to be applied and it is not cut back or turned off during the measurements.

It is obvious that both the high frequency spurious noises and the low frequency line noises are drastically reduced by the attachment of the cathode shields on both the filament ends, and a cathode shield on the HV input side of the magnetron, as shown in Fig. 4.6. The reduction level of the low frequency line noises of the newly-designed magnetron (c) is up to 30dB compared to the reference magnetron (a).

Furthermore, the results clearly specify that both the high frequency spurious noise levels

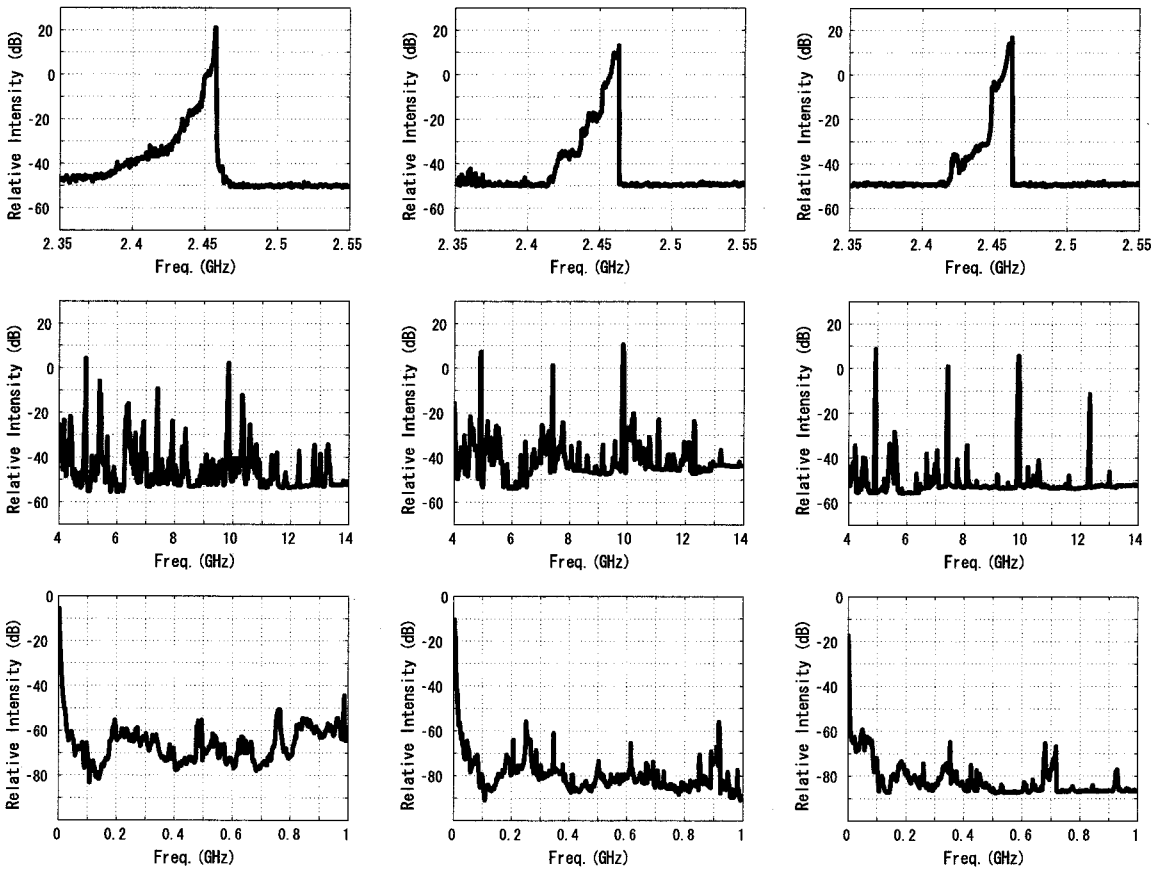

Figure 4.6: Experimental results of the fundamental spectrum (top), high frequency noises (center), and line noises (bottom) at I_b = 400mA and V_f = 3.3V. (a): the reference magnetron, (b): the magnetron with the cathode shields on both the filament ends, and (c): the magnetron with the cathode shield on the HV input side.

and the low frequency line noise levels of the magnetron (c) are lower than those of the magnetron (b). Therefore, they prove that shielding the cathode on the HV input side, where the amount of electrons is emitted more than the RF output side as described in Chapter 2, is more effective to suppress the spurious noises.

In terms of the fundamental spectrum, spurious noise levels below 2.43GHz were less than the noise floor levels of the spectrum analyzer when the cathode shields are attached to the magnetron. Hence, the cathode shields work well for the spurious noises in the fundamental frequency bands as well as in the high and low frequency bands. Moreover, the spurious levels from 2.43GHz to 2.45GHz of the magnetron (c) are less than those of the magnetron (a) and (b) by about 10dB. Therefore, shielding the cathode only on the HV input side is also effective to suppress the spurious noises around the carrier frequency.

4.3.3 Discussions

Here we first describe electron motion and resonance conditions in a magnetron [60], and then we discuss noise suppression mechanisms by the attachment of the cathode shields.

Suppression of electron motion on both the filament ends by attachment of the cathode shields

In two-dimensional analysis of a magnetron, the magnetic flux density can not vary in the axial direction at all. In a practical magnetron, in contrast, the nearer the magnetic pole formed by the external magnets, the larger the magnetic flux density becomes. In the case of the reference magnetron 2M210M1F1, the axial magnetic flux density B in the vicinity of the anode vanes on both the filament ends of the magnetron increases by a few percent compared to the center. Thus, the azimuthal $\boldsymbol{E}\times\boldsymbol{B}$ drift velocity $|\langle v(\theta)\rangle| = |\langle E_{\mathrm{r}}\rangle|/B$, which is the dominant velocity component of electrons, gradually increase when electrons are coming close to both the filament ends of the tube, where $\langle E_{\mathrm{r}}\rangle$ is the mean radial electrostatic field. Besides, both circulating motion with a radius $|R_2|$ and an angular velocity Ω_2, and rotating motion with a radius $|R_1|$ and an angular velocity Ω_1 expressed in Eq. (2.15), Eq. (2.16) and Eq. (2.17) in the center are different from those in both the filament ends.

In the case of the π-mode oscillation, the oscillation frequency f is expressed by the $\boldsymbol{E}\times\boldsymbol{B}$ drift velocity from Eq. (3.17) and Eq. (3.18),

$$f = \frac{|\langle v(\theta)\rangle|}{2\pi r_{\mathrm{a}}}\frac{N}{2} = \frac{N}{4\pi r_{\mathrm{a}}}\frac{|\langle E_{\mathrm{r}}\rangle|}{B}, \tag{4.9}$$

where r_{a} is the anode radius, N is the number of anode vanes.

As we mentioned above, the axial magnetic flux density B on both the filament ends increase by a few percent compared to the center in the reference magnetron. Hence, f on both the filament ends is lower than that at the center from Eq. (4.9), assuming $|\langle E_{\mathrm{r}}\rangle|$ is uniform in the axial direction. Note that the magnetrons with the cathode shields suppress

the spurious noises in the fundamental bands at frequencies below 2.43GHz, which is lower than the peak frequency by at least 1%, as shown in Fig. 4.6. This experimental result is therefore consistent with theoretical analysis.

Furthermore, the magnetron with the cathode shield on the HV input side suppresses the spurious noises in the fundamental bands up to 2.45GHz compared to the magnetron with the cathode shields on both the filament ends. This improvement takes place because the cathode shield of the magnetron (c) extends towards the center of the filament more than the magnetron (b), as shown in Fig. 4.5. In the magnetron (c), the cathode shield affects the azimuthal $\boldsymbol{E} \times \boldsymbol{B}$ drift motion of electrons near the center, so that the spurious noises near the peak frequency are suppressed.

In conclusion, the suppression of the spurious noises in the fundamental frequency bands is caused by the disappearance of the azimuthal $\boldsymbol{E} \times \boldsymbol{B}$ drift motion of electrons around the filament ends owing to the attachment of the cathode shields.

With regard to the spurious noises in high and low frequency bands, electron motion and resonance conditions in a magnetron are also adapted. Due to the axial variation of the magnetic flux density, the resonant angular frequency ω is a function of $B(z)$ to the axial direction, since both Ω_1 and Ω_2 is a function of B. Therefore, the π-mode oscillation has some bandwidth and there is a possibility of intermodulation between electrons in the center region and in the end regions. If the intermodulation occurs in practice, beat noises will appear continuously in some bandwidth, which is determined by the difference of ω between the center and the ends.

The other resonance conditions following the selectional rules described in Sec. 3.5 are also considered to be sources of the spurious noises, although they hardly contribute to their strong oscillations. If we assume the infinitely long cylinder as a magnetron tube, these resonance conditions will discretely exist since B is constant in the axial direction. In practice, however, the resonance conditions will easily change due to the variation of B in the axial direction.

Axial motion of electrons

Now we take the axial diffusive motion of electrons described in Sec. 2.2 into consideration. In a magnetron, we predicted the axial diffusion length to be the order of 10^{-2}m, ten times longer than the axial dimension of the reference magnetron. Therefore, some electrons emitted from both the filament ends axially move from the center to the outer sheaths easily. Although the end hats attached to the cathode ends manage to prevent them from reaching the outer sheaths, these electrons will not be regulated at all unlike other electrons in the center region of the filament. This is because the axial electrostatic field E_z begins to emerge on both the filament ends due to the existence of the end hats. Furthermore, the external magnetic field on both the filament ends is not perfectly parallel to the axial direction, and some radial magnetic field component B_r exists there. Therefore, the azimuthal drift velocity v_θ is composed of not only the dominant component of (E_r, B_z) but also the slight component

of (E_z, B_r) on both the filament ends. The drift velocity due to this slight component may accelerate or decelerate the regular motion of electron spokes.

Besides, the axial oscillation described in Sec. 3.5 will take place in a magnetron. Since the cathode shields prevent electrons from the axial motion, so that spurious noises caused by the axial oscillation are expected to be suppressed.

In conclusions, cathode shields also play an important role in suppressing noises due to preventing electrons from the axial motion towards both the filament ends.

Narrowness of the constant-voltage range

From the experimental results of the anode voltage, we have found out that the constant-voltage range were narrower in the magnetrons with the cathode shields than the reference magnetron, as shown in Fig. 4.7. The closeup of the anode voltage waveforms in the constant-voltage range, as shown at the bottom figures in Fig. 4.7, clearly indicates the fact which is mentioned above. According to the time domain analysis we describe in Chapter 3, spurious noises are widely and constantly generated in the constant-voltage range. In the cases of magnetrons with cathode shields, therefore, one of the contributing factors of the spurious noise reduction is that average energy of the spurious noises per a cycle of the half-wave voltage doubler is decreased by narrowness of the constant-voltage range.

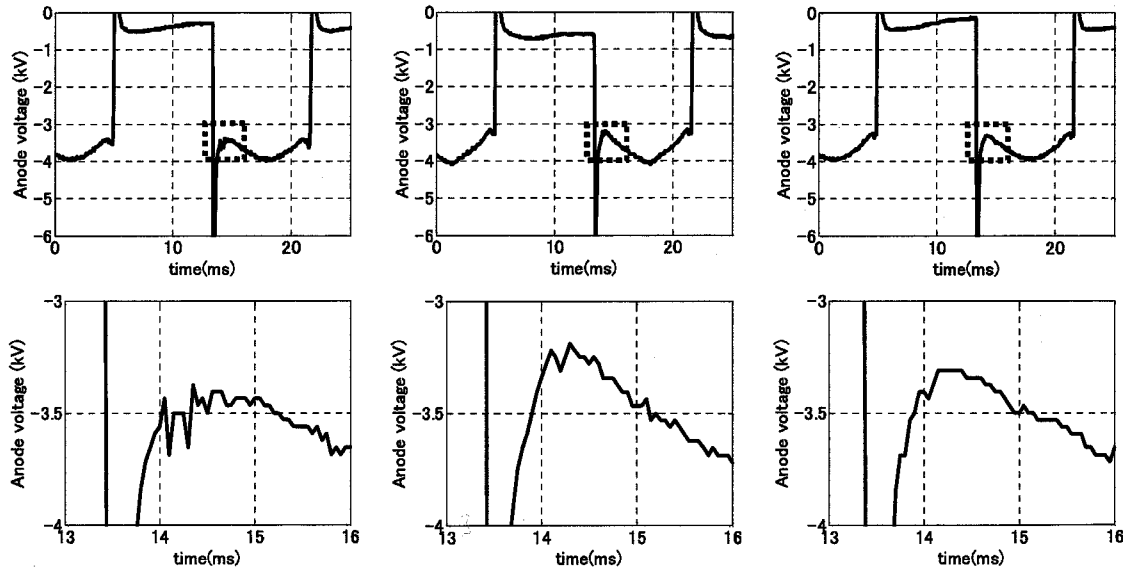

Figure 4.7: Anode voltage waveforms of the magnetrons (top), and the closeup of the anode voltage waveforms including the constant-voltage range (bottom), shown in the dotted boxes in the top figures. (a): the reference magnetron, (b): the magnetron with the cathode shields on both the filament ends, and (c): the magnetron with the cathode shield on the HV input side.

Here we discuss the causes why the constant-voltage range is reduced in the cases of the magnetrons with the cathode shields. As described above, cathode shields play a role in preventing electrons both from being emitted to the interaction space and from diffusing in the axial direction. Hence, the anode current begins to flow at a lower anode voltage, since the condensed electrons around the center of the cathode unavoidably contribute to the anode current with slight axial diffusive motion. Therefore, the constant-voltage range gets narrower when the cathode shields are attached to the magnetron than that of the reference magnetron.

4.4 Summary

The experimental measurements of the spurious noises for newly-designed low noise magnetrons were conducted in this chapter.

With regard to the modifications of the interaction space and the anode voltage, we have found that the wider the interaction space and the lower the anode voltage, the less the spurious noises are generated. Also we found out that the modification of the anode voltage was more effective than that of the interaction space.

With regard to magnetrons with cathode shields, we found out that a cathode shield only on the HV input side works more effectively for suppressing spurious noises than cathode shields on both the filament ends. The reduction levels of the low frequency line noises of the magnetron with the cathode shield on the HV input side are up to 30dB compared to the reference magnetron. This is because the cathode shield only on the HV input side corresponds to the axial distribution of the filament temperature better than the cathode shields on both the filament ends. Then, electron motions around the filament are suppressed more effectively. In conclusion, a cathode shield attached to the end of the cathode filament works well for suppressing spurious noises when it is designed to correspond to the axial distribution of the filament temperature.

In this chapter, we operated magnetrons by a half-wave voltage doubler, but not a DC stabilized power supply. Besides, the filament current was not cut back or turned off during the oscillation at all in the experiments. Therefore, it can be concluded that the newly-designed low noise magnetron with the cathode shield has a great possibility to be operated with reduced spurious noises even though they are mounted in a conventional microwave oven system.

Of great interest is that the "axially asymmetric" configuration of the cathode shield works more effectively than the "axially symmetric" configuration, although that depends on the axial distribution of the filament temperature. The relation between "axially asymmetric" and "axially symmetric" has been also observed in an experimental study on "magnetic priming" [66], which have reported that "axially asymmetric magnetic priming" has been more effective for noises and startup of magnetrons than "axially symmetric magnetic prim-

ing". Therefore, three-dimensional numerical simulations and theoretical analysis of the magnetrons' operation will be much more important future works to explore these "axially asymmetric" issues.

Chapter 5

Noise Features of Filament-off Magnetron

5.1 Introduction

A magnetron is one of the strong candidates as a DC-RF converter for WPT and SPS transmitting systems, because its DC-RF conversion efficiency is higher, it costs less and it has smaller weight/power ratio than solid state devices. On the other hand, a magnetron has a wide oscillation bandwidth and it generates spurious noises in various frequency bands. For the use of the WPT and SPS transmitting systems, the wide oscillation bandwidth will become a serious obstacle of obtaining a frequency allocation for a WPT system and a SPS. It also complicates the realization of a Phase-Controlled Magnetron (PCM), which is really required in order to design a phased array system with numerous elements in a SPS, as described in Sec. 1.4. Besides, spurious noises will interfere with other radio applications both in space and on the Earth, when they are radiated from the WPT and SPS transmitting systems. In order to produce the narrow bandwidth of the fundamental frequency and to reduce the spurious noises generated from a magnetron, we propose that the filament current should be turned off during the oscillation when the magnetron is operated by a DC stabilized power supply, in this chapter.

With regard to the fundamental frequency spectrum, Brown mentioned that the "internal feedback mechanism" [41, 51] contributes to a quiet magnetron operation, in the simplest terms. The internal feedback mechanism most effectively takes place by turning off the filament current during the oscillation. In this chapter, we describe experimental studies of noise features of a filament-off magnetron. The principle of the continuous oscillation of the filament-off magnetron is described in detail in Sec. 5.2.

In Sec. 5.3, we describe the effects for the oscillation bandwidth by turning off the filament current. We experimentally found as well as Brown that the oscillation frequency spectrum of the magnetron becomes narrower as a result of the internal feedback mechanism. An impor-

tant finding is that the cause of the reduced oscillation bandwidth is not only the reduction of the filament temperature described by Brown [41, 51], but also the disappearance of the disturbance in the anode current related to the anode current–anode voltage characteristic of the magnetron. The disturbance in the anode current takes place when the anode current is below a certain threshold value, and the disturbance does not occur when the anode current exceeds the threshold value. Even in such a case, the oscillation bandwidth becomes narrower when the filament current is turned off. This is because the cathode temperature is reduced by the internal feedback mechanism as well as Brown's discussions so that motion of electrons is less affected by the thermal effects in the filament-off magnetron.

Brown showed the experimental results of the oscillation frequency spectrum [41] , but not the spectra of the spurious noises in high frequency bands and low frequency bands. In Sec. 5.4, we describe that a filament-off magnetron has a beneficial effect for the reduction of spurious noises as well as the oscillation bandwidth.

In the present study, it was found experimentally that the DC-RF conversion efficiency degrades somewhat although noise features of the filament-off magnetron improves well. We describe the degradation of the DC-RF conversion efficiency and its causes when the magnetron is operated with turning off the filament current in Sec. 5.5.

5.2 Principle of the continuous oscillation of a filament-off magnetron

With regard to the continuous oscillation of a filament-off magnetron, Brown shortly expressed that this phenomena is due to the "internal feedback mechanism" of a magnetron [41, 51]. He mentioned that "when the external source of heating, the filament, is turned off and the control loop regulates the amount of electron back bombardment to keep the filament at the desired temperature". In the following paragraphs, we describe the principle of the continuous oscillation with the internal feedback mechanism in more detail with the two-dimensional linear magnetron model shown in Fig. 1.2.

Now we consider that an electron is passing from a negative RF potential to a positive RF potential, as the left-hand electron in the region (C) shown in Fig. 1.2. Then, it comes back to the cathode by drift motion in the y direction owing to the RF field in the x direction. This means that some of the RF electromagnetic energy in a magnetron is transformed to the kinetic energy of an electron moving toward the cathode, since work is done on the electron by the RF field. Hence, the energy of the electron when it arrives back to the cathode is considered larger than that at the time of the emission from the cathode. Finally the electron collides with the surface of the cathode, and it heats up the cathode filament, or it may become a primary electron and cause the emission of secondary electrons. These phenomena are called back bombardment. Due to the cathode self-heating and secondary electron emission by the back bombardment, electrons are continuously supplied from the cathode filament even if the

filament current is turned off during the oscillation of the magnetron.

Due to the process described above, the oscillation of the magnetron can be maintained without the cathode heating by the filament current once it starts. Moreover, turning off or cutting back the filament current is a well-known beneficial way for a magnetron to give a long life to the cathode, since this technique prevents the cathode filament from overheating due to the excessive back bombardment [38]. However, it is necessary for a magnetron to heat up the cathode filament in advance in order to start the oscillation, since the cathode temperature is so low that electrons are hardly emitted in the magnetron before the oscillation. Also, it is preferable to operate a magnetron by a DC stabilized power supply when the filament current is turned off, in order to supply somewhat stable back bombardment energy for the cathode filament to maintain the generation of thermal electrons or secondary electrons.

5.3 Measurements of the oscillation bandwidth

5.3.1 Measurement system

A schematic of a measurement system for obtaining the oscillation bandwidth is shown in Fig. 5.1. The reference magnetron 2M210M1F1 was used for the experiments. The operating power supply for the magnetron is a commercially available DC stabilized power supply (Glassman, PS/LT005R360-20). The magnetron is coupled to a waveguide so that the RF output is connected to an almost-matched termination of a high-power dummy load of 2.5kW (Nihon Koshuha, WDL-0233E). The oscillation spectrum of the magnetron is obtained by measuring the electromagnetic wave leakage with a spectrum analyzer (HP 8563E). This leak-

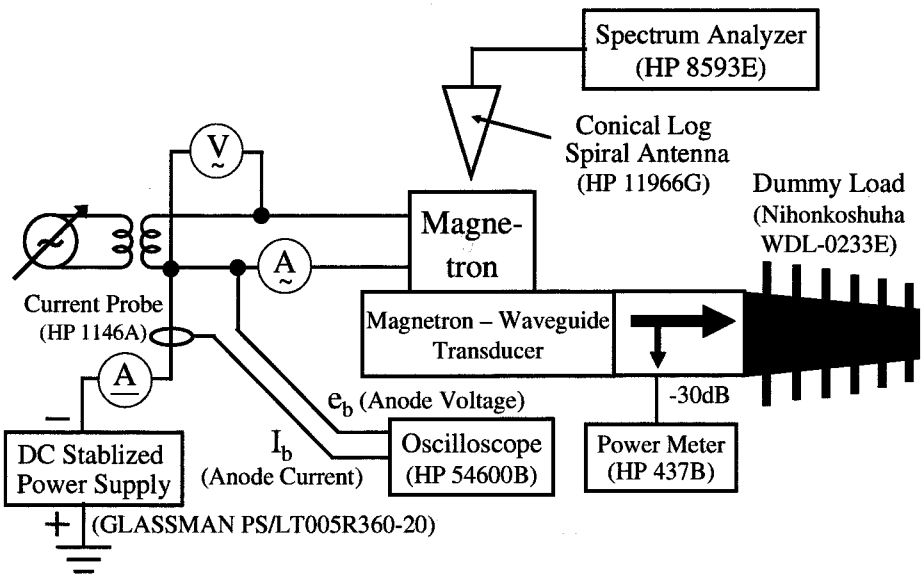

Figure 5.1: Schematic of a measurement system for obtaining the oscillation bandwidth of a magnetron.

age is received by a spiral antenna (HP 11966G), which is immediately above the magnetron. The choke coil and the feed-through capacitor on the input side of the magnetron are removed. It has already been confirmed that the spectrum of the leakage electromagnetic wave from the magnetron and the output spectrum radiated from the RF output are identical in spectral shape. Although they are not identical in spectral intensity, we can relatively compare the spectra displayed on the spectrum analyzer, when the measurements are conducted in the same measurement system.

The spectrum analyzer is set in such a way that the resolution bandwidth is 10kHz and the video bandwidth is 10kHz, with a frequency measurement range from 2.43 to 2.47GHz. In the present measurement, the maximum value of the spectrum is held on the spectrum analyzer during a period of one minute after the magnetron and the waveguide has been thermally stable. Thus, the spectrum analyzer displays the envelope of the maximum levels of the spectrum generated from the magnetron. Simultaneously with the spectral measurement, the anode current waveform is monitored with an oscilloscope (HP 54600B).

5.3.2 Experimental results

As experimental results, the oscillation frequency spectra of the reference magnetron at an anode current of 250mA are shown in Fig. 5.2. The thin line represents the oscillation spectrum when the filament current is the normal rated value of 10A, and the thick line represents the spectrum when the filament current is turned off to 0A. Fig. 5.3 shows the anode current waveforms measured at the same time. The thin line is the oscillation frequency spectrum at a filament current of 10A and the thick line is at a filament current of 0A.

The Q value of the spectrum is calculated by the following equation;

$$Q = \frac{f}{\Delta f}, \tag{5.1}$$

where f is the carrier frequency of a magnetron and Δf is the half-power bandwidth of the magnetron spectrum. From the experimental results, the Q value is 8.0×10^2 when the filament current is 10A, and 1.1×10^5 when the filament current is 0A.

It is clear from Fig. 5.2 that the oscillation frequency spectrum is broad and has two peaks when the filament current is 10A, but it is narrow and has only one peak when the filament current is 0A. A significant cause of this difference appears in the anode current waveforms shown in Fig. 5.3. It is evident from Fig. 5.3 that the anode current waveform is almost constant when the filament current is 0A but has a pulse shape when the filament current is 10A.

In general, a magnetron exhibits phenomena called frequency pushing and frequency pulling. In each case, the oscillation frequency is changed by variations of the anode current and the load impedance. In the present experiment, since the measurements were performed after the magnetron and the waveguide had reached a stable temperature, the variation of the load impedance in temperature is considered negligible. Therefore, the bandwidth

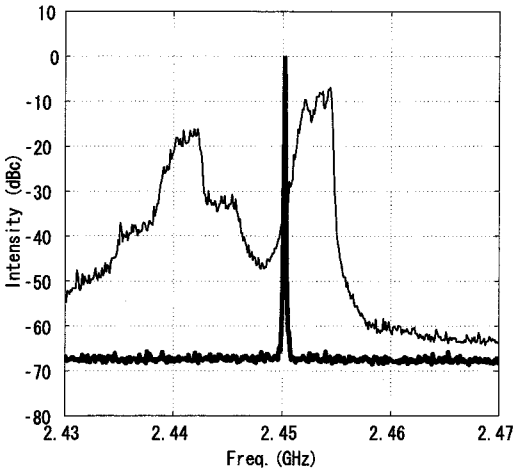

Figure 5.2: Oscillation spectra of the reference magnetron when I_b=250mA. Resolution bandwidth: 10kHz. Thin line: I_f=10A, and thick line: I_f=0A. The Q values are 8.0×10^2 when I_f=10A and 1.1×10^5 when I_f=0A.

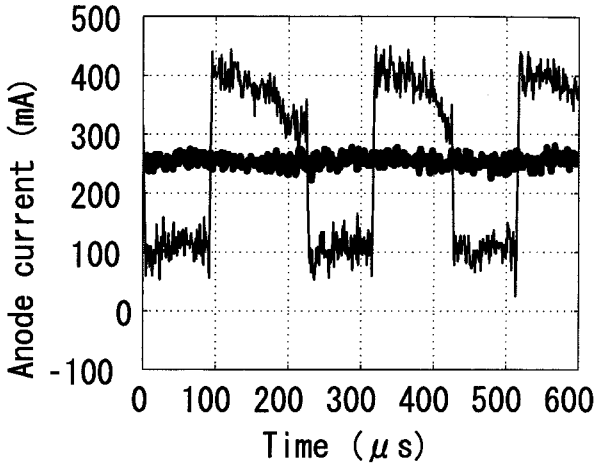

Figure 5.3: Anode current waveforms when I_b=250mA. Thin line: I_f=10A, and thick line: I_f=0A.

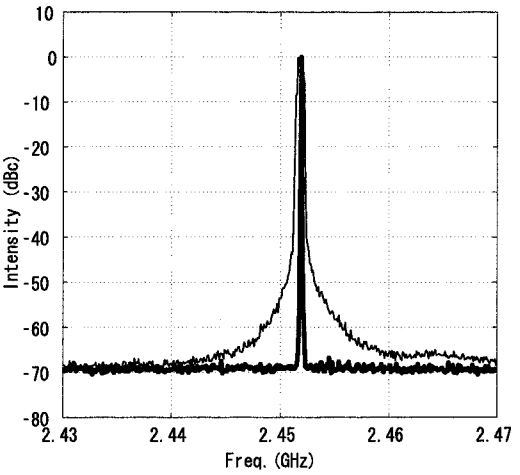

Figure 5.4: Oscillation spectra of the reference magnetron when I_b=400mA. Resolution bandwidth: 10kHz. Thin line: I_f=10A, and thick line: I_f=0A. The Q values are 8.2×10^3 when I_f=10A and 1.2×10^5 when I_f=0A.

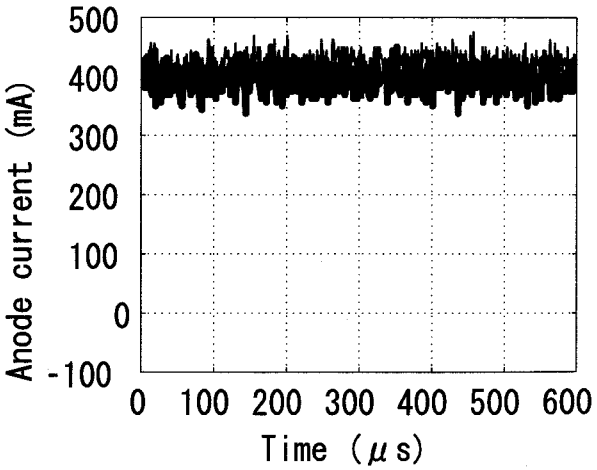

Figure 5.5: Anode current waveforms when I_b=400mA. Thin line: I_f=10A, and thick line: I_f=0A.

reduction of the oscillation bandwidth due to turning off the filament current is caused by the stabilization of the anode current whose disturbance is eliminated in the filament-off magnetron.

In terms of the frequency pushing, experimental formula has been already expressed in Eq. (3.19). Note that the bottom value and the peak value of the pulse waveforms seen in the case of a filament current of 10A in Fig. 5.3 are about 100mA and 350mA, respectively. When substituting these values of the anode current for Eq. (3.19), the frequencies are derived to be 2.396GHz at an anode current of 100mA and 2.454GHz at an anode current of 350mA, respectively. At an anode current of 350mA, the derived frequency is almost equal to the peak frequency on the right-hand side of the spectrum in Fig. 5.2, although it diverges from the peak frequency on the left-hand side by -1.9% at an anode current of 100mA.

The anode current disturbance at a filament current of 10A is generated in the magnetron used here when the anode current is less than 350mA, but not above this value. Hence, the relationship between the filament current and the frequency spectrum is described in the case of no disturbance in the anode current. Fig. 5.4 and Fig. 5.5 show the oscillation frequency spectra and the anode current waveforms, respectively, when the anode current is 400mA. The thin line represents the oscillation frequency spectrum at a filament current of 10A and the thick line is at a filament current of 0A. As can be seen in Fig. 5.5, the anode current is not disturbed when the filament current is 10A. It is seen that the oscillation bandwidth is narrower at a filament current of 0A than 10A, even without the anode current disturbance. The Q values of the spectra are 8.2×10^3 for a filament current of 10A and 1.2×10^5 for a filament current of 0A.

In summary, the experimental results show that a filament-off magnetron improves the oscillation bandwidth narrower.

5.3.3 Discussions

Influence of the AC magnetic field due to the AC filament current

First, we discuss influence of the AC magnetic field due to the AC filament current as an improvement factor of the oscillation bandwidth of a filament-off magnetron. The effect may cause ham noises to appear as the modulation of the signal.

The cathode filament was heated by an AC current in the present experiments. Hence, there is a possibility that the effect of the AC magnetic field generated in the magnetron by the AC current may have caused the anode current disturbance, since the magnetron filament has a shape of a coil. Assuming that the cathode filament is a solenoidal coil, the magnetic field in the center of the cathode generated by the filament current is equal to nI_{f}, where n is the number of turns. As $n = 9$ in the reference magnetron, the AC magnetic field of $(90\sqrt{2}\ \mathrm{H}) \times \sin\omega t$ could be generated in the center of the cathode filament, where ω is the commercial frequency.

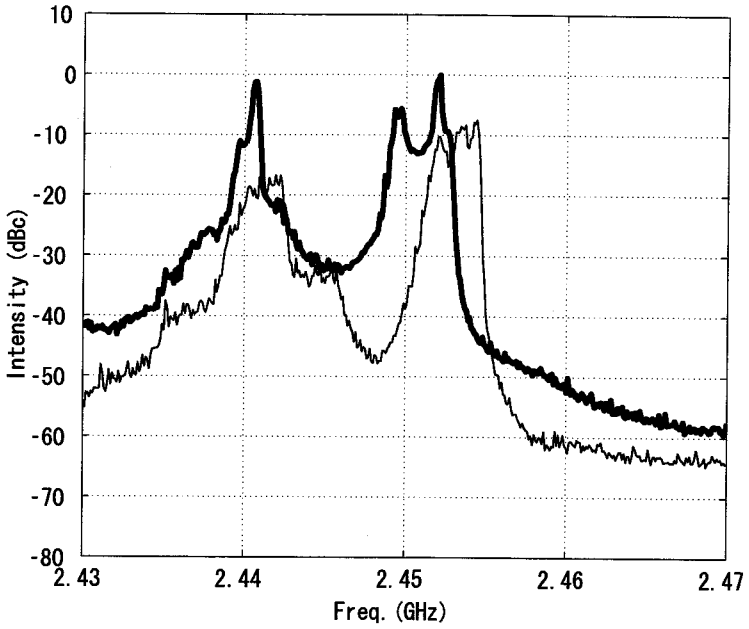

Figure 5.6: Comparison of oscillation spectra by the difference in power supplies for the filament when I_b=250mA and I_f=10A. Thin line: AC power supply, and thick line: DC power supply.

Here, we compare the spectra when the power supply of the filament is AC and DC. When the DC filament current is applied, the magnetic field generated by the filament current is static. Hence, we can investigate, from the comparison, whether the alternation of the magnetic field affects the anode current disturbance. For the DC supply of the filament, a commercial DC stabilized power supply (KENWOOD PS20-18) is used. Note that the DC stabilized power supply is connected to the commercial power source via 1:1 transformer for the purpose of insulation because the DC power supply for the filament itself is included in a part of the high voltage circuit of the measurement system.

Fig. 5.6 shows comparison of the spectra between the AC and DC filament currents at an anode current of 250mA and a filament current of 10A. From Fig. 5.6, no dramatic spectral change, such as the one in Fig. 5.2, is observed between the two filament current sources. Hence, it is concluded that the reduced oscillation bandwidth is not related to the AC magnetic field generated around the filament.

Cause of the anode current disturbance

Next, we discuss the cause of the disturbance in the anode current. From several experiments it is found that the disturbance is related to the oscillation characteristics of the magnetron. Here we analytically explain the relationship between the anode current disturbance and the oscillation characteristics.

Fig. 5.7 shows the measured results of the anode current–anode voltage characteristics of

the magnetron when the filament current is 10A and 0A.

As one can see from Fig. 5.3, the bottom value and the peak value of the pulse waveforms seen in the case of a filament current of 10A are about 100mA and 350mA, respectively. When we pay attention to Fig. 5.7 on the basis of this information, the anode current–anode voltage characteristic for the filament current of 10A is clearly flatter than that for a filament current of 0A in the anode current range from 100mA to 350mA. From the measurement results in Fig. 5.7, the curves between anode currents of 100mA and 350mA are expressed by

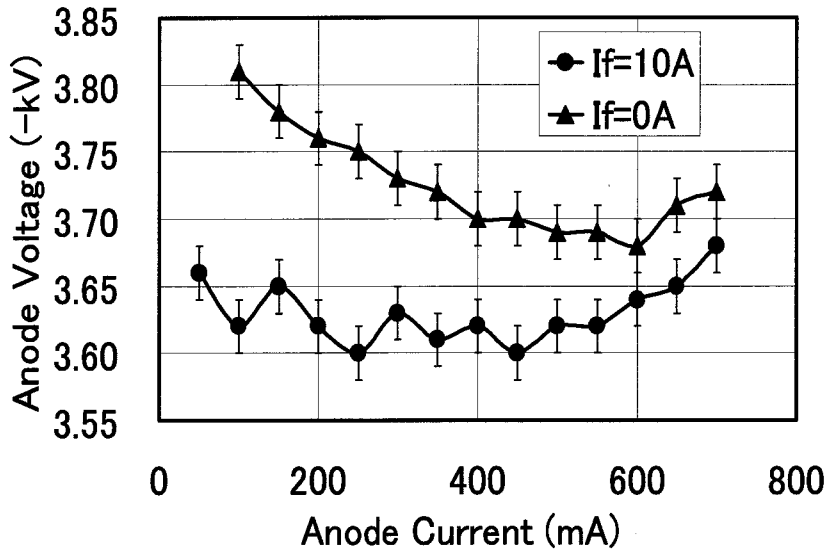

Figure 5.7: Anode current I_b vs. anode voltage e_b curves when the filament current I_f= 10A and 0A.

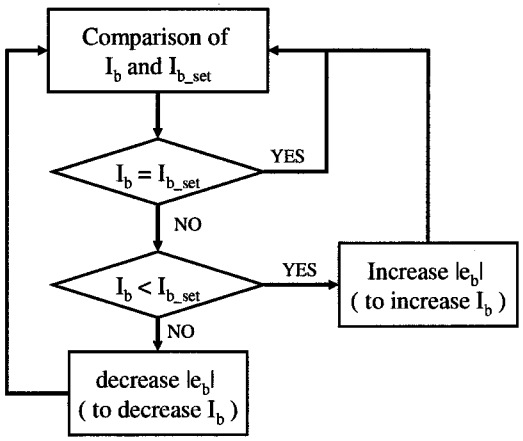

Figure 5.8: Flowchart of a prospective current controlling system of a DC stabilized power supply.

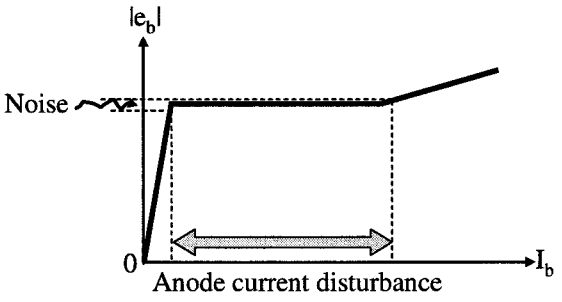

Figure 5.9: Anode current I_b disturbance by a small ripple noise on the anode voltage $|e_b|$.

linearization;

$$e_{\mathrm{b}} = \begin{cases} -(3.49 \times 10^2 \text{ V/A}) \times I_{\mathrm{b}} + (3.84 \times 10^3 \text{ V}), & I_{\mathrm{f}} = 0\mathrm{A} \\ -(7.42 \times 10 \text{ V/A}) \times I_{\mathrm{b}} + (3.62 \times 10^3 \text{ V}), & I_{\mathrm{f}} = 10\mathrm{A} \end{cases}, \tag{5.2}$$

where e_{b} is the anode voltage, I_{b} is the anode current, and I_{f} is the filament current. Note that the variation of the curve at a filament current of 10A falls within the measurement error. Moreover, the characteristic of the constant-voltage region is also observed in the experimental results when a magnetron is operated by a half-wave voltage doubler, as described in Chapter 3.

In order to explain the pulse-shaped anode current waveform, it is assumed that the anode voltage value is constant in the anode current range from 100mA to 350mA for a filament current of 10A, and assumed that a flowchart of a current controlling system of a DC stabilized power supply is expressed as shown in Fig. 5.8. When the anode current is set in the range from 100mA to 350mA, the anode current–anode voltage characteristic of the magnetron becomes a constant-voltage type in this range. The DC stabilized power supply used in the present experiments has a setup to control the anode current when the magnetron starts its oscillation.

When the anode voltage is increased to make this DC stabilized power supply produce an anode current, a large current suddenly flows due to this constant-voltage property, and then it exceeds the specified anode current. However, since in practice the DC stabilized power supply tries to control the anode current, it tries to decrease the anode voltage to make the excessive anode current return to the original value. In spite of the current control, however, the anode current now falls below the specified anode current due to this constant-voltage characteristic again. The undulation of the anode current control is repeated in this manner and the anode current eventually becomes pulse-shaped.

In practice, the anode current–anode voltage characteristic has a slight slope. Nevertheless, it is sufficiently possible that similar undulation of the anode current control could take place and that the disturbance of the anode current could be triggered by a slight change in the anode voltage owing to a small ripple noise on the anode voltage, as shown in Fig 5.9.

On the other hand, the slope of the anode current–anode voltage characteristic for a filament current of 0A is clearly recognized, and the anode current is controlled without the occurrence of the undulations such as those occurring at a filament current of 10A, even if there are variations in the anode voltage caused by noises and ripples. Therefore, the almost constant anode current is obtained when a magnetron is operated with turning off the filament current.

Causes of the anode current–anode voltage curve when $I_{\mathrm{f}} = 0\mathrm{A}$

Next, we discuss the causes of the anode current–anode voltage characteristic shown in Fig. 5.7 when the filament current is 0A. The subject of the discussion here is why the gradient $de_{\mathrm{b}}/dI_{\mathrm{b}}$

is negative as if a magnetron has a negative resistance. Discussion in the following paragraphs also explains the internal feedback mechanism in detail when the filament current is turned off.

When the filament current is 0A, there is no external cathode heating. Therefore, oscillation continues as a result of the internal feedback mechanism; cathode self-heating and secondary electron emission due to the back bombardment effect. Here, the reduction of the anode current implies the reduction of the electrons flowing in the anode from Eq. (3.16). At the same time, the numbers of electrons returning to the cathode under the influence of the RF electric field, described in Sec. 5.2 also decrease in a relative sense. Then, due to the reduction of the back bombardment energy, the filament temperature falls off, as described in Sec. 2.3. Finally, the amount of electron emission from the cathode decreases and the number of electrons in the magnetron is also reduced due to the decrease of the saturation current I_{th} given by the Richardson-Dushman's equation Eq. (2.21). In summary, the number of electrons flowing in the anode is further reduced, and then the anode current is further decreased.

If this cycle continues, the anode current continues to decrease and the oscillation finally stops. However, since the DC stabilized power supply in practice controls the anode current, the anode voltage is increased for an increased anode current, when the anode current falls below a set value. Because of this increase of the anode voltage, $|R_1|$ in Eq. (2.17), namely, the rotation radius of the electrons becomes larger, and the rotating electron clouds approach the anode. At the same time, the number of electrons which take energy from the microwave oscillation also increases relatively. Therefore, contrary to the previous case, the number of electrons returning to the cathode increases and the back bombardment energy grows. Eventually, the anode current increases and comes back to the set value.

In another case, if the anode current is being increased, the number of electrons flowing into the anode increases and the back bombardment energy grows, so that the anode current exceeds the set value. Hence, the anode voltage is reduced, lowering the anode current to the set value.

On the other hand, when the filament current is 10A, a sufficiently large amount of electrons exists in the magnetron due to the thermal emission by the filament heating, as shown in Fig. 2.12. Therefore, no change in the anode voltage occurs in response to a change of the anode current, unlike the case of a filament current of 0A. In practice, the anode voltage changes as a result of the anode current change. However, if such a change is slight, it is sufficiently possible, as shown in Fig. 5.7, that the anode current–anode voltage characteristic has a constant-voltage range.

The above discussion can be summarized as follows. The difference in the frequency spectra shown in Fig. 5.4 is caused by the presence or the absence of the disturbance in the anode current. The disturbance in the anode current for a filament current of 10A is caused by an anode current–anode voltage characteristic that is almost a constant-voltage

type, shown in Fig. 5.7. The slope of the anode current–anode voltage characteristic obtained for a filament current of 0A is attributed to the change in the number of electrons in the magnetron corresponding with the variations of the anode current.

Way to prevent the anode current disturbance

Next, we discuss a way to prevent the anode current disturbance when the filament current of a magnetron is applied to the normal rated value during the oscillation. Although the filament current should be turned off for a quiet magnetron operation, a demerit of a filamen-off magnetron is that the oscillation has a possibility to stop at a very low anode current of several tens of mA, in the examined magnetron case. Hence, it is beneficial to find out a prevention method of the anode current disturbance in order to operate a magnetron with narrow oscillation bandwidth at a low anode current.

The frequency of the pulse waveform of the anode voltage shown in Fig. 5.3 is about 5kHz. This frequency is attributed to the time constant of the DC stabilized power supply used here.

One method of preventing this disturbance may be the insertion of a low-pass filter between the DC stabilized power supply and the magnetron. However, for the oscillation of the magnetron used here, a voltage on the order of kV is needed. Since the undulation frequency is almost 5 kHz, it is difficult to design a low-pass filter with good performance robust to high voltage.

Also, the anode current–anode voltage characteristic shown in Fig. 5.7 is that of the magnetron itself. The responsivity of the magnetron was considered to be the order of MHz from an experimental measurement [50]. Therefore, when the magnetron is operated by a constant-voltage power supply while a filament current is applied, a narrow oscillation bandwidth cannot be obtained unless the variation of anode current is controlled extremely well.

Hence, in the present stage, the method of the anode current stabilization by turning off the filament current is an extremely effective way to make the frequency spectrum of the oscillation narrow.

Causes of improvement of the oscillation bandwidth in the absence of the anode current disturbance

The anode current disturbance at a filament current of 10A is generated in the examined magnetron when the anode current is less than 350mA, but not above this value. Lastly, we discuss causes of improvement of the oscillation bandwidth in the absence of the anode current disturbance.

When the anode current disturbance disappears, improvement of the oscillation bandwidth is caused by difference of the filament temperature between turning on and off the

filament current. The relationship between the filament current and the filament temperature has already been shown in Fig. 2.12.

From Fig. 2.12, it is found that the filament temperature decreases as the filament current decreases. Hence, one of the causes of the narrow-band oscillation in this case is the reduction of the filament temperature by turning off the filament current so that the thermal effects in the magnetron tube are reduced as well as Brown has mentioned the phenomenon as the internal feedback mechanism [41, 51].

In conclusion, it is considerably effective to turn off the filament current even where there is no disturbance of the anode current, from the point of view of the narrow-band oscillation.

5.4 Measurements of spurious noises

In the previous section, we verified that the oscillation bandwidth of a filament-off magnetron becomes narrow by the internal feedback mechanism. Here we describe the experimental measurements of spurious noises generated from a filament-off magnetron, in order to investigate the effects of the internal feedback mechanism on the spurious noises.

5.4.1 Measurement systems

Measurement system for radiation noise from the RF output

We also conducted experiments in the present section with the reference magnetron 2M210M1F1. The measurement is conducted in the condition that the feedthrough capacitor and the choke coil attached to the magnetron are removed, in order to detect all spurious noises generated from the magnetron itself as much as possible.

A schematic of a measurement system for spurious noises is shown in Fig. 5.10. The reference magnetron is also operated by a DC stabilized power supplies, which can control the anode current. The filament current is controlled by a variable transformer. The magnetron is attached to a magnetron-waveguide transducer. The microwave energy is radiated from a 2.45GHz horn antenna and received by a 5.8GHz horn antenna. The distance between two antennas is 4m. High frequency spurious noises are measured through the 5.8GHz horn antenna with a spectrum analyzer. At the same time, low frequency line noises are measured with another spectrum analyzer. The low frequency line noises are picked up from the DC input lines with a current probe. In the present measurements the maximum values of the spurious noises are held on the spectrum analyzers during a period of one minute, after the magnetron and the waveguide have become stable in temperature. Thus, the spectrum analyzers display the envelopes of the maximum levels of the spectra generated from a magnetron. Waveforms of the anode voltage and the anode current are also measured with an oscilloscope in parallel with the frequency spectrum measurements.

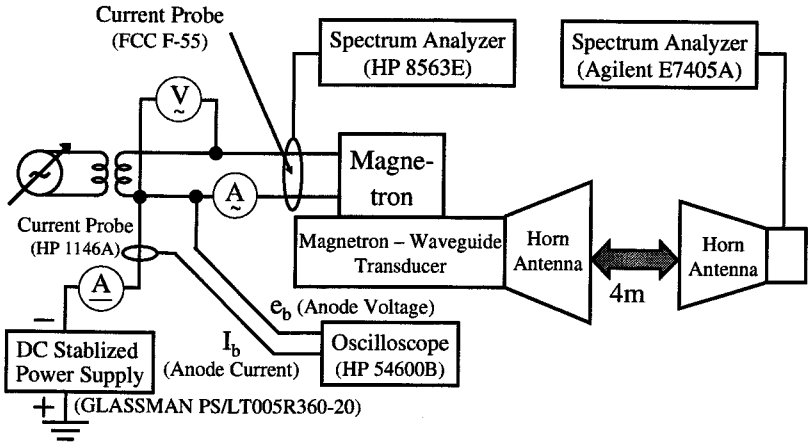

Figure 5.10: Schematic of a measurement system for spurious noises generated from a magnetron.

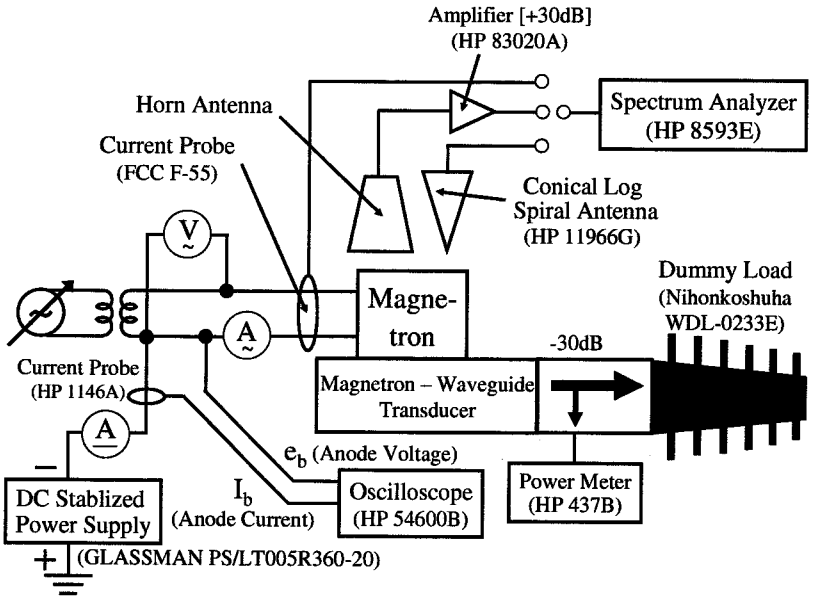

Figure 5.11: Schematic of a leakage measurement system. The measurement system is easier to set up than Fig. 5.10.

The frequency characteristics of the 5.8GHz horn antenna, a 5.8GHz waveguide-coaxial transducer and free space losses were calibrated in frequency, in order to obtain the spurious noise levels roughly. The means of the calibration in the present measurement system is as follows. First, the propagation characteristics from 1GHz to 10GHz are measured with a network analyzer, under the same condition as shown in Fig. 5.10, except the difference of the transmitting system, from the 2.45GHz horn antenna and the magnetron-waveguide transducer mounting the magnetron, to a standard conical log spiral antenna mounted on Port 1 of the network analyzer. The standard antenna covers the frequency from 1GHz

to 10GHz. Port 2 of the network analyzer is attached to the 5.8GHz coaxial-waveguide transducer with the 5.8GHz receiving horn antenna. Then, the calibration curve is derived by subtracting the directional gain of the standard antenna. Hence, the spectrum levels, which are propagated from the aperture of the 2.45GHz horn antenna, are calibrated by the curve. The deviation error from the calibration curve is ± 5dB. Note that this calibration, however, neglects the frequency characteristics due to the difference of the directional gain and the polarization between the standard antenna and the transmitting system as shown in Fig. 5.10. Besides, the error or the uncertainty is essentially inevitable by means of this calibration because the measurement is conducted in the near-field region and beyond the standard of these coaxial-waveguide transducers and horn antennas.

The measurement of the low frequency line noises, on the other hand, is not calibrated because the noise levels are varied by the setting position of the current probe. For this reason, the measured spectra are relatively compared only in a figure with respect to the low frequency line noises. From this point of view, the unit of the spectral intensity is dB when the low frequency line noises are measured, in contrast with dBc when the high frequency spurious noises are measured.

Measurement system for relative comparison of spectra

We set up another measurement system for measuring spurious noises, as shown in Fig. 5.11. It is almost the same as that for measuring spurious noises with easy set-up, as described in Subsec 4.2.2 and depicted in Fig. 4.1. In this system, the spurious noises generated from the magnetron are obtained by measuring the electromagnetic wave leakage. Although the calibration of the spectra is too difficult to obtain the absolute value in dBc in contrast to the measurement system in Fig. 5.10, the measurement system is easy to set up and sufficient for our purpose: the comparison of the spectra.

5.4.2 Experimental results

Radiation noises in the high frequency bands

Fig. 5.12 shows the spectra from 4GHz to 10GHz at I_b=250mA. The thin line and the thick line in Fig. 5.12 show the spectra at I_f=10A and I_f=0A, respectively. Note that the anode current is set to be 250mA instead of the rated value of 300mA as shown in Table 1.1. This is not only because we focus on the comparison of the spurious noises when the anode current is disturbed at a filament current of 10A, but also because we have utilized a magnetron around 250mA of the anode current in the present PCM system [49].

From Fig. 5.12, it is obvious that the high frequency spurious noises are drastically improved as well as the oscillation bandwidth when a magnetron is operated with turning off the filament current during the oscillation. The spurious noise levels of the filament-off magnetron are reduced below the noise floor levels of the spectrum analyzer in various frequency

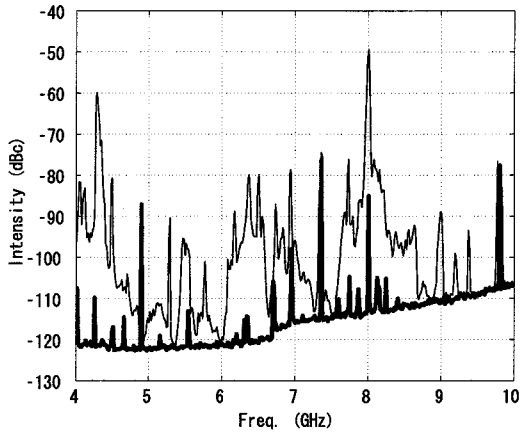

Figure 5.12: High frequency spurious noise spectra at I_b=250mA. The span of the measurement is from 4GHz to 10GHz. Thin line: I_f=10A, and thick line: I_f=0A. Resolution bandwidth: 100kHz.

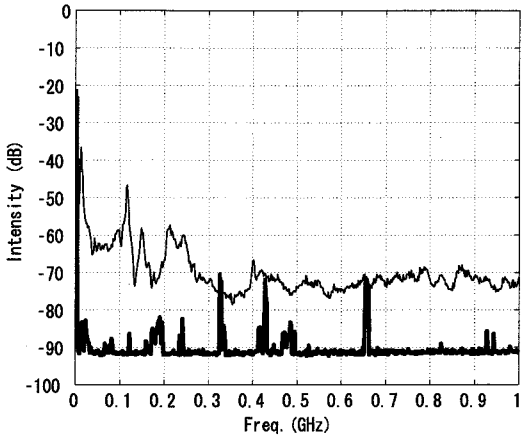

Figure 5.13: Low frequency line noise spectra at I_b=250mA. The span of the measurement is from 100kHz to 1GHz. Thin line: I_f=10A, and thick line: I_f=0A. Resolution bandwidth: 100kHz.

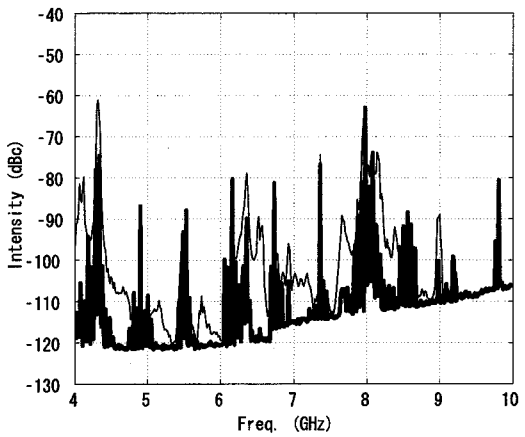

Figure 5.14: High frequency spurious noise spectra at I_b=400mA. The span of the measurement is from 4GHz to 10GHz. Thin line: I_f=10A, and thick line: I_f=0A. Resolution bandwidth: 100kHz.

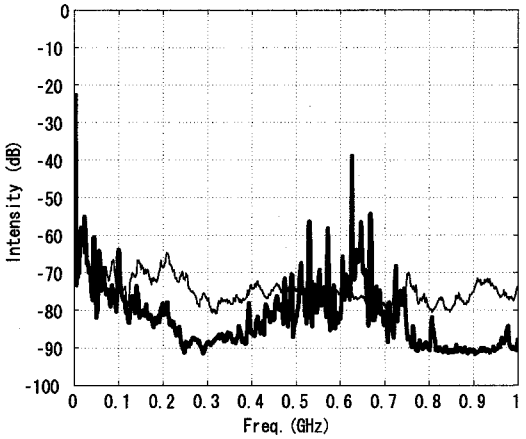

Figure 5.15: Low frequency line noise spectra at I_b=400mA. The span of the measurement is from 100kHz to 1GHz. Thin line: I_f=10A, and thick line: I_f=0A. Resolution bandwidth: 100kHz.

bands. The reduction levels of the spurious noises of the filament-off magnetron are up to 50dB compared to the magnetron with the normal rated filament current.

Harmonics, however, do not have the great improvement between turning on the filament current and turning it off. This is because the harmonics of the magnetron are caused by the distortion of the fundamental, and the distortion is independent on the effect of the filament current. In spite of the fact, the harmonics levels at I_f=0A are lower than -70dBc in the present measurement system, as shown in Fig. 5.12. These levels are comparable to or better than those of some semiconductor amplifiers. The reason why the harmonic levels of a magnetron are not so high has already been described in Sec. 3.5.

Line noises in the low frequency bands

We have also observed the line noises on cables between the magnetron and the DC stabilized power supply. Fig. 5.13 shows the low frequency line noises from 100kHz to 1GHz at I_b=250mA. The thin line and the thick line in Fig. 5.13 show the spectrum at I_f=10A and I_f=0A, respectively. The experimental results show that the low frequency line noises of the filament-off magnetron are also suppressed below the noise floor levels of the spectrum analyzer in various frequency bands. The reduction levels of the spurious noises of the filament-off magnetron are up to 40dB compared to the magnetron with the normal rated filament current.

Spurious noises in the absence of the anode current disturbance

Fig. 5.14 and Fig. 5.15 show the spectra of the high frequency spurious noises and the low frequency line noises, respectively, at I_b=400mA, where the anode current was not disturbed even if the filament current was turned on. The thin line and the thick line in both Fig. 5.14 and Fig. 5.15 show the spectrum at I_f=10A and I_f=0A, respectively.

In the case of I_b=400mA, the spurious noises of the filament-off magnetron are somewhat reduced than the magnetron with the normal rated filament current. However, the reduction effects are less drastic when the magnetron does not have the anode current disturbance at I_f=10A than when it does.

5.4.3 Discussions on sources of spurious noises

Influence of the anode current disturbance

We showed that the narrow oscillation bandwidth was caused by the stabilization of the anode current in Sec. 5.3. Experimentally, the disturbance in the anode current was not observed when I_b is over about 350mA at I_f=10A in the case of the examined magnetron. First, in order to verify the effect of the the anode current disturbance, we discuss influence of the anode current disturbance.

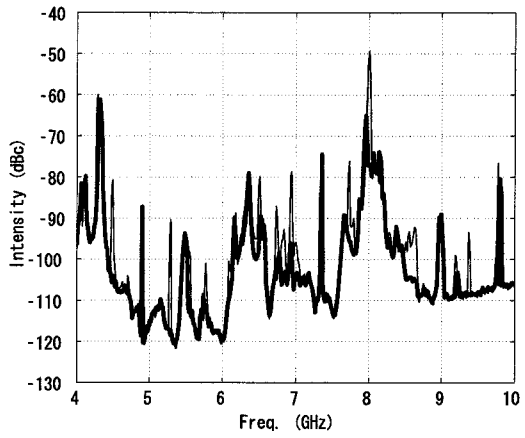

Figure 5.16: Relationship between the spurious noises and the anode current disturbance at I_f=10A. Thin line: I_b=250mA, and thick line: I_f=400mA, Resolution bandwidth: 100kHz.

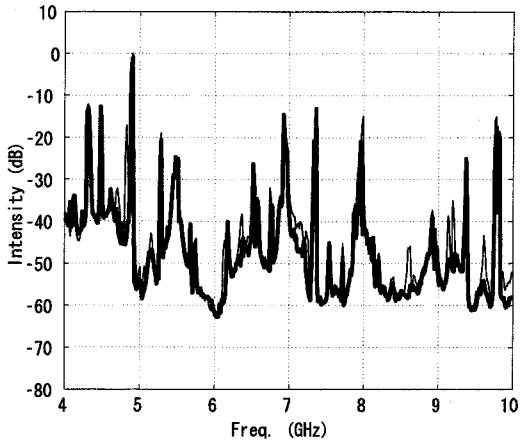

Figure 5.17: Relationship between the spurious noises and the influence of the AC magnetic field at I_b=250mA and I_f=10A. Thin line: AC power supply, and thick line: DC power supply, Resolution bandwidth: 100kHz.

Fig. 5.16 shows the comparison of the high frequency spurious noises at I_f=10A. The thick line in Fig. 5.16 shows the spectrum at I_b=400mA, which is the same as that of the thin line in Fig. 5.14, where the anode current disturbance dose not take place. The thin line in Fig. 5.16 shows the spectrum at I_b=250mA, which is the same as that in Fig. 5.12, where the anode current disturbance takes place. From Fig. 5.16, the spurious noise levels at I_b=400mA was almost comparable with those at I_b=250mA, although some noises are reduced in some frequency bands. The result shows that the spurious noises in the high frequency bands are generated when the filament current is turned on, whether or not the anode current disturbance is observed.

Influence of the AC magnetic field due to the AC filament current

Next, we researched on the effect of the magnetic flux generated by the AC filament current. The effect may cause ham noises to appear as the modulation of the signal, although we concluded that there was no drastic spectral change of the fundamental frequency spectrum whether the power supply of the filament was AC or DC.

Fig. 5.17 shows the comparison of the spurious noises in the high frequency bands between the AC filament current and the DC filament current at I_b=250mA and I_f=10A. Note that the vertical unit in Fig. 5.17 is dB normalized by the maximum value of two lines, and that the thin line and the thick line show the spectrum when the power supply of the filament is AC and DC, respectively. Fig. 5.17 shows that there is also no drastic spectral change whether the power supply of the filament was AC or DC. Therefore, the effect of the magnetic flux due

to the AC filament current has no relevance to the spurious noises as well as the oscillation bandwidth.

From the discussions above, neither the anode current disturbance nor the influence of the AC magnetic field due to the AC filament current are causes of the noise reduction of the filament-off magnetron.

Causes of the noise reduction of the filament-off magnetron

Now, we discuss causes of the noise reduction of the filament-off magnetron.

As described in Sec. 2.3, thermal electrons are emitted from the center of the cathode filament enough to maintain the oscillation of the magnetron; in contrast they are much less emitted from the RF output side when the magnetron is operated with turning off the filament current. We have also demonstrated that cathode shields on the filament ends work exceedingly well for suppressing spurious noises due to preventing electrons from axial motion towards both the filament ends, as described in Sec. 4.3. Therefore, we conclude that the dominant cause of the noise reduction is suppression of the electron motion around the filament ends due to the falloff of the filament temperature, throughout the experimental measurements of the various magnetrons described in the previous chapters.

Relationship between spurious noises in the high frequency bands and line noises in the low frequency bands

From the experimental results shown in Fig. 5.12 and Fig. 5.13, it is considered that the improvement of the high frequency spurious noises is related to the improvement of the low frequency line noises. We have found out that some low frequency line noises shown in Fig. 5.13 at I_f=0A were probably related to some high frequency spurious noises at I_f=0A shown in Fig. 5.12. For examples, the discrete noise at 660MHz in Fig. 5.13 seems to have some kind of relationship with the discrete noises at 4.9GHz (the second harmonics) $\pm$ 660MHz. This relationship is probably the intermodulation effect between the low frequency line noises and the fundamental or the harmonics. Therefore, the high frequency spurious noises were improved greatly at I_f=0A because of the improvement of the low frequency line noises.

Also, the relationship between the spurious noises in the high frequency bands and the low frequency bands is also seen in Fig. 5.14 and Fig. 5.15. The line noises are widely generated in 600MHz band shown in Fig. 5.15, and the spurious noises are observed in the bands of the 2nd harmonic (4.9GHz) $\pm$ 600MHz, the 3nd harmonic (7.35GHz) $\pm$ 600MHz, and the 4th harmonic (9.8GHz) $-$600MHz, which seem to correspond to the line noises. Therefore, the generation of these noises in the high frequency bands is caused by the intermodulation between the line noises in the low frequency bands and the harmonics.

Cause of excessive line noises at I_b=400mA and I_f=0A

As shown in Fig. 5.15, the low frequency noise levels observed larger in some frequency bands at I_f=0A than I_f=10A. Here we discuss this contradictory phenomena to the effects described in Sec. 5.3 and by Brown [41,51].

We consider that these excessive line noises are caused by the magnitudes of the filament temperature and the electrostatic field. It is experimentally known that the more the anode current increases, the more the filament temperature increases, as described in Sec. 2.3. Also, it is experimentally observed that the absolute value of the anode voltage increases as the filament current is turned off, as shown in Fig. 5.7. Combining these experimental results and the discussion described in Sec. 4.2, the excessive line noises at I_b=400mA and I_f=0A may be caused by superposing the effects of both the increase of the filament temperature and the increase of the anode voltage.

5.5 Measurements of DC-RF conversion efficiency

The DC-RF conversion efficiency of the reference magnetron was also measured with the measurement system shown in Fig. 5.1. In terms of the input DC power P_i, the anode voltage e_b and the anode current I_b are measured with an oscilloscope via a high voltage probe and an ampere meter, respectively. The output RF power P_o is measured with a power meter (HP 437B) via a power sensor. The filament power P_f is measured with an voltmeter for the filament voltage V_f and an ampere meter for the filament current I_f. Then, the DC-RF conversion efficiency η is expressed in the following;

$$\eta = \frac{P_o}{P_i + P_f} = \frac{P_o}{e_b I_b + V_f I_f}. \tag{5.3}$$

5.5.1 Experimental results and discussions

Fig. 5.18 shows the filament current versus the DC-RF conversion efficiency when the anode current is 250mA and 400mA. From the measurement results, it is found that the DC-RF conversion efficiency deteriorates as the filament current decreases at both the anode current values.

There are two causes of the degradation of the DC-RF conversion efficiency due to reduction of the filament current. One is the increase of the input power to the magnetron. The other is the decreased microwave output power. The former cause results from the increase in the anode voltage, as shown in Fig. 5.7, in order to compensate for lack of electron emission in the magnetron. The latter is attributed to an increased amount of work, performed by the RF electromagnetic energy in the tube, on the electrons moving toward the cathode. As results, the DC-RF conversion efficiency of the magnetron is degraded in the filament-off operation. Combining these two causes above, we can conclude that the degradation of

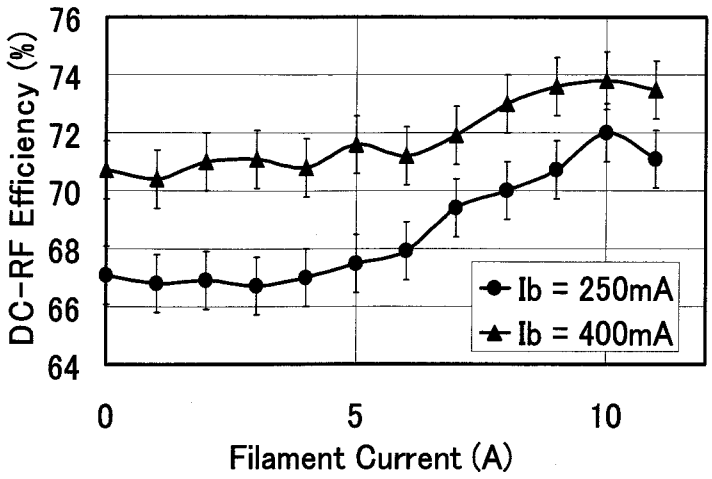

Figure 5.18: Filament current vs. DC-RF efficiency when a magnetron is operated by a DC stabilized power supply. I_b: anode voltage.

DC-RF conversion efficiency results from the energy consumption for the internal feedback mechanism.

5.5.2 Relation between DC-RF conversion efficiency and noise levels

In terms of the DC-RF conversion efficiency of a magnetron, the equation of the electron efficiency is utilized in the following steps. First, the DC input energy corresponds to the potential energy of an electron eV. Next, the RF output energy is given by subtracting the kinetic energy $mv^2/2$ from the potential energy when the electron arrives at the anode. Hence, the equation of the electron efficiency η is expressed as the following;

$$\eta = \frac{eV - (mv^2/2)}{eV} = 1 - \frac{mv^2}{2eV} \tag{5.4}$$

The electron velocity v is derived from differentiating Eq. (2.15) with respect to t, then

$$\begin{aligned} v = \frac{d\xi}{dt} &= \frac{d}{dt}(|R_1|e^{j\Omega_1 t} + |R_2|e^{j\Omega_2 t}) \\ &= j|R_1|\Omega_1 e^{j\Omega_1 t} + j|R_2|\Omega_2 e^{j\Omega_2 t}, \end{aligned} \tag{5.5}$$

where $|R_1|$ and $|R_2|$ is introduced instead of R_1 and R_2, in order to express a radii of the electron trajectory. Here we define the initial velocity of the electron as zero when $t = 0$, then Eq. (5.5) becomes

$$v = \left.\frac{d|\xi|}{dt}\right|_{t=0} = |R_1|\Omega_1 + |R_2|\Omega_2. \tag{5.6}$$

Then, Eq. (5.4) becomes

$$\eta = 1 - \frac{m(|R_1|\Omega_1 + |R_2|\Omega_2)^2}{2eV}. \tag{5.7}$$

Here Ω_2 shows the azimuthal velocity of the circulating motion of the electron. When a magnetron has N anode vanes and it is operated in the π-mode oscillation, the oscillating

angular frequency ω is equal to $\Omega_2 N/2$. Therefore, we substitute $|R_1|$,$|R_2|$, Ω_1 and Ω_2 of Eq. (2.16) and Eq. (2.17) for Eq. (5.7), finally the equation of the electron efficiency is express as the following;

$$\eta = 1 - \frac{r_a + r_c}{r_a - r_c} \frac{1}{(eNB/2\omega m) - 1}. \tag{5.8}$$

Eq. (5.8) means that DC-RF conversion efficiency theoretically increases as the magnetic field B increases when we assume the steady oscillation in frequency.

However, note that the experimental results and discussion described in Sec. 4.2 indicated that spurious noises are generated more and more as the magnetic field B and/or the electrostatic field $|\langle E_r \rangle|$ increase. When the magnetic field B increases, the electrostatic field $|\langle E_r \rangle|$ has to increase in order to realize the steady oscillation in frequency, since the electron velocity is basically determined by the $\boldsymbol{E} \times \boldsymbol{B}$ drift velocity $|\langle E_r \rangle|/B$.

In conclusion, the DC-RF conversion efficiency and the noise features of a magnetron may be caught in a dilemma in the present magnetron configurations.

5.6 Summary

In this chapter, we have experimentally demonstrated that both the oscillation bandwidth and the spurious noises generated from a magnetron highly improved by turning off the filament current during the oscillation when the magnetron was operated by a DC stabilized power supply. Although the harmonics of the carrier frequency was not improved even though the filament current was turned off, the reduction levels of the filament-off magnetron are up to 50dB in the high frequency bands and 40dB in the low frequency bands, respectively, compared to the magnetron with the normal rated filament current. In conclusion, the demerits of a magnetron, which has a wide oscillation bandwidth and spurious noises in various frequency bands, are possible to overcome with the following method; a magnetron is operated by a DC stabilized power supply and the filament current is turned off during the oscillation.

With regard to the oscillation bandwidth, we have found out that there are two main causes that the oscillation bandwidth become narrower; one is the disappearance of the anode current disturbance, and the other is the decrease of thermal effects by reduction of the filament temperature. Especially, we have first found out that the mechanism of the former cause. The anode current disturbance at a filament current of 10A takes place due to the anode current–anode voltage characteristic that is almost a constant-voltage type. The constant-voltage range is caused by the abundance of electron emission when the filament current is turned on. On the other hand, the slope of the anode current–anode voltage characteristic at a filament current of 0A is attributed to the variation of the electrons in the tube, therefore the anode current–anode voltage characteristic has no constant-voltage range.

This improvement of the oscillation bandwidth has enabled the development of Phase-Controlled Magnetrons (PCM) [43–45] by the injection locking method and the phase locked loop feedback, as described in Sec. 1.4. By means of PCM systems, the high power microwave transmission system with PCM array, which is called SPORTS (Space POwer Radio Transmission System), was also developed [12,45,67], as described also in Sec 1.4.

With regard to the spurious noises, we conclude that the dominant cause of the noise reduction is suppression of electron motions around the filament ends due to the falloff of the filament temperature, throughout the experimental measurements of the various magnetrons. We have also found out that there is the intermodulation effect between the low frequency line noises and the fundamental or the harmonics, and that the high frequency spurious noises are suppressed greatly when the filament current is turned off because of the suppression of the low frequency line noises.

In terms of DC-RF conversion efficiency, when a magnetron is operated with the internal feedback mechanism, the degradation of the DC-RF conversion efficiency occurs. This is because the energy consumption for the sustainment of the internal feedback mechanism increases in order to maintain the oscillation. From the numerous experimental measurements, there seems to be a trade off between the noise features and the DC-RF conversion efficiency, and the trade-off problem has not been solved yet in the present study. However, the DC-RF conversion efficiency is essentially important to realize a totally efficient WPT system from DC to DC. Therefore, the realization of a WPT system with both low noises and high conversion efficiency comes up for future works.

Chapter 6

Concluding Remarks

6.1 Summary

In this thesis, we have experimentally studied on noise features of a magnetron, and low noise WPT, in order to develop both a magnetron and a WPT system which are compatible with other radio applications.

In order to obtain necessary data for discussing generation mechanisms of noises from a magnetron, we have conducted two experimental measurements of electron emission from the filament cathode in Chapter 2; one is the measurements of the anode current with axially-segmented anode blocks, the other is the measurements of the filament temperature. As the former experimental results, we observed that half of the electrons arrived at the center region of the anode, and that the amount of the electrons arriving at the HV input side of the anode was twice as much as that arriving at the RF output side of the anode. We also analyzed the trajectory and the diffusive motion of an electron in the cases of both a cylindrical diode and a magnetron. From the analysis, the axial travel distance of an electron by the diffusive motion was comparable with the size of the tube in the cylindrical diode case, and it was about ten times larger than the size of the tube in the magnetron case, when it was calculated at a position of the anode radius. Therefore, the axial diffusive motion of an electron is not negligible in a magnetron operation. We have also found out that the axial diffusive motion is caused by the charge density gradient, and that it is hardly linked to the initial velocities of thermal electrons. As the latter experimental results, we have found out that the filament temperature is high enough to sustain the oscillation, and that the filament temperature falls much more on both the filament ends, especially on the RF output side than at the center, when a magnetron is operated by a DC stabilized power supply and the filament current is turned off. Summarizing these experimental results above from the viewpoint of electron emission from the cathode filament, we concluded that the examined magnetrons denoted the tendency that electrons are estimated to be emitted most in the center region, next on the HV input side, and least on the RF output side.

In Chapter 3, we have conducted a time domain analysis of magnetron noises. From the

analysis, we have found out that spurious noises generated from a magnetron are classified into the following five types; (1) side band noises around the carrier and low frequency line noises at frequencies below about 150MHz, generated at an anode current of less than 0.2A, (2) high frequency spurious noises and low frequency line noises generated in the transition region between the constant voltage range and the non-constant voltage range at an anode current of around 0.4A, (3) low frequency line noises generated in the non-constant voltage range characterized by frequencies of 400MHz or 800MHz, and high frequency spurious noises generated at an anode current of around 0.6A, attributed to the intermodulation of the low frequency line noises and the harmonics, (4) the harmonics generated in synchrony with the fundamental, and (5) low frequency line noises generated in synchrony with the electron circulation. We also discussed generation mechanisms of spurious noises with respect to each classification. The generation mechanisms of the categorized noises are likely to be different. Hence, it will be a beneficial way to deal with these classified noises independently for the purpose of developing a low noise magnetron to fulfill EMC with other radio applications in specified frequency bands. Besides, we discussed spurious noises in constant-voltage range generated constantly in various frequency bands. We concluded that the variation of the potential minimum and the axial oscillation of electrons could be regarded as one of the noise sources in the constant-voltage range. Furthermore, we analytically verified that the axial oscillation of electrons has a great possibility to take place at frequencies of several tens of MHz.

In Chapter 4, we have studied newly-designed low noise magnetrons. With regard to the modifications of the interaction space and the anode voltage, we have found that the wider the interaction space and the lower the anode voltage, the less the spurious noises are generated. Also, we found out that the modification of the anode voltage was more effective than that of the interaction space. With regard to the magnetrons with cathode shields, we conclude that a cathode shield attached to the end of the cathode filament works effectively for suppressing spurious noises when it is designed to correspond to the axial distribution of the filament temperature. The reduction levels of the low frequency line noises of a magnetron with a cathode shield on the HV input side are up to 30dB compared to the reference magnetron. In the experiments in Chapter 4, we operated a magnetron by a half-wave voltage doubler, but not a DC stabilized power supply. Besides, the filament current was not cut back or turned off during the oscillation at all. Therefore, this achievement means that the newly-designed magnetron with a cathode shield has a great possibility to be operated with reduced spurious noises even though they are mounted in a conventional microwave oven system.

In Chapter 5, we have studied noise features of a filament-off magnetron for the use of WPT. We have experimentally found out that turning off the filament current effectively works not only for making the oscillation bandwidth narrower but also for suppressing spurious noises generated from a magnetron. With regard to the oscillation bandwidth, we have verified that there are two main causes that the oscillation bandwidth of the filament-off mag-

netron becomes narrower when a magnetron is operated by a DC stabilized power supply; one is the disappearance of the disturbance in the anode current, and the other is the decrease of the thermal effects. Especially, we have first verified that the mechanism of the former cause. The disturbance in the anode current takes place when the filament current is turned on, due to the anode current–anode voltage characteristic that is almost a constant-voltage type. With regard to the spurious noises, the reduction levels of the filament-off magnetron are up to 50dB in high frequency bands and 40dB in low frequency bands, respectively, compared to the magnetron with the normal rated filament current. We conclude that the dominant cause of the noise reduction is suppression of electron motions around the filament ends due to the falloff of the filament temperature, throughout experimental measurements of the various magnetrons. We have also found out that there is the intermodulation effect between the low frequency line noises and the fundamental or the harmonics, and that the high frequency radiation noises of the filament-off magnetron are suppressed greatly because of the suppression of low frequency spurious noises.

6.2 Future works

For future works, three-dimensional analysis of a magnetron with computer simulation will play an extremely important role in developing a low noise magnetron aimed at a low noise WPT system and EMC with other radio applications. This is because we have verified, in this thesis, that a study of a magnetron from a three-dimensional perspective was absolutely necessary, although many previous studies of a magnetron were conducted from a two-dimensional perspective. However, theoretical three-dimensional analysis is near-impossible since we have to consider all elements in a magnetron, such as lines of the electric and magnetic force, distribution of the charge density, diffusive motion of electrons, the structure of a magnetron etc., as equivalent circuits. Our research group has successively been conducting computer simulations on a magnetron with the electromagnetic particle code called KEMPO (Kyoto University ElectroMagnetic Particle cOde) [68–73], and the latest study [73] has been succeeded in three-dimensional computer simulations with KEMPO. Also, three-dimensional computer simulations of an oven magnetron are ongoing with commercially available electromagnetic particle-in-cell codes called MAGIC [74], in several countries [66, 75, 76]. These numerous three-dimensional studies on a magnetron with powerful computers are expected as a design support tool for realizing a development of a noiseless magnetron, a low noise WPT system and EMC with other radio applications in the future.

With respect to WPT and SPS applications, EMC with other radio applications is an inevitable problem. A study of EMC of a future SPS transmitting system at a frequency of 2.45GHz with other radio applications such as satellite communication services, wireless communication systems, radio astronomy etc. is described in Appendix B. We conducted numerical simulation on one-dimensional microwave beam pattern with random phased arrays,

and found out that the 1GW-class 2.45GHz SPS transmitting system satisfied the EMC with a 5GHz-band microwave relay system or a fixed satellite service when the phases of antenna elements have a random distribution at the harmonics of the carrier frequency. EMC of a WPT and SPS transmitting system with other radio applications should be thoroughly investigated for future works. Especially, EMC with radio applications at the carrier frequency of a WPT and SPS transmitting system will be quite difficult problem, but needing to be solved.

Also, improvement of the DC-RF conversion efficiency of a magnetron will be quite important especially for the use of WPT. From our numerous experimental measurements, there seems to be a trade off between the noise features and the DC-RF conversion efficiency, and the trade-off problem has not been solved yet in the present study. However, the DC-RF conversion efficiency is vitally important to realize a totally efficient WPT system from DC to DC. Therefore, the realization of WPT with both low noise and high conversion efficiency comes up for future works.

Appendix A

Experimental Results of Time Domain Analysis

In this appendix, we show the experimental results of the time domain analysis, described in Chapter 3, at all the frequencies of the time domain analysis points.

A.1 Time domain analysis in the fundamental bands

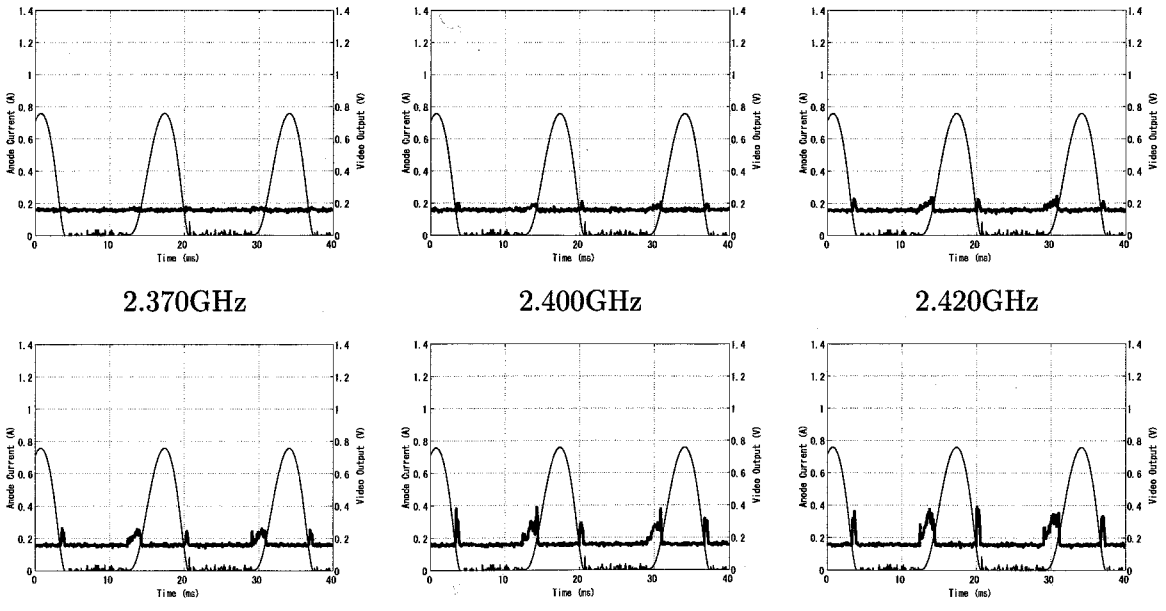

2.370GHz 2.400GHz 2.420GHz

2.430GHz 2.440GHz 2.445GHz

Figure A.1: Experimental results of the time domain analysis in the fundamental bands (1). Thick line and right axis: video output signal from the spectrum analyzer, thin line and left axis: the corrected anode current waveform of the reference magnetron.

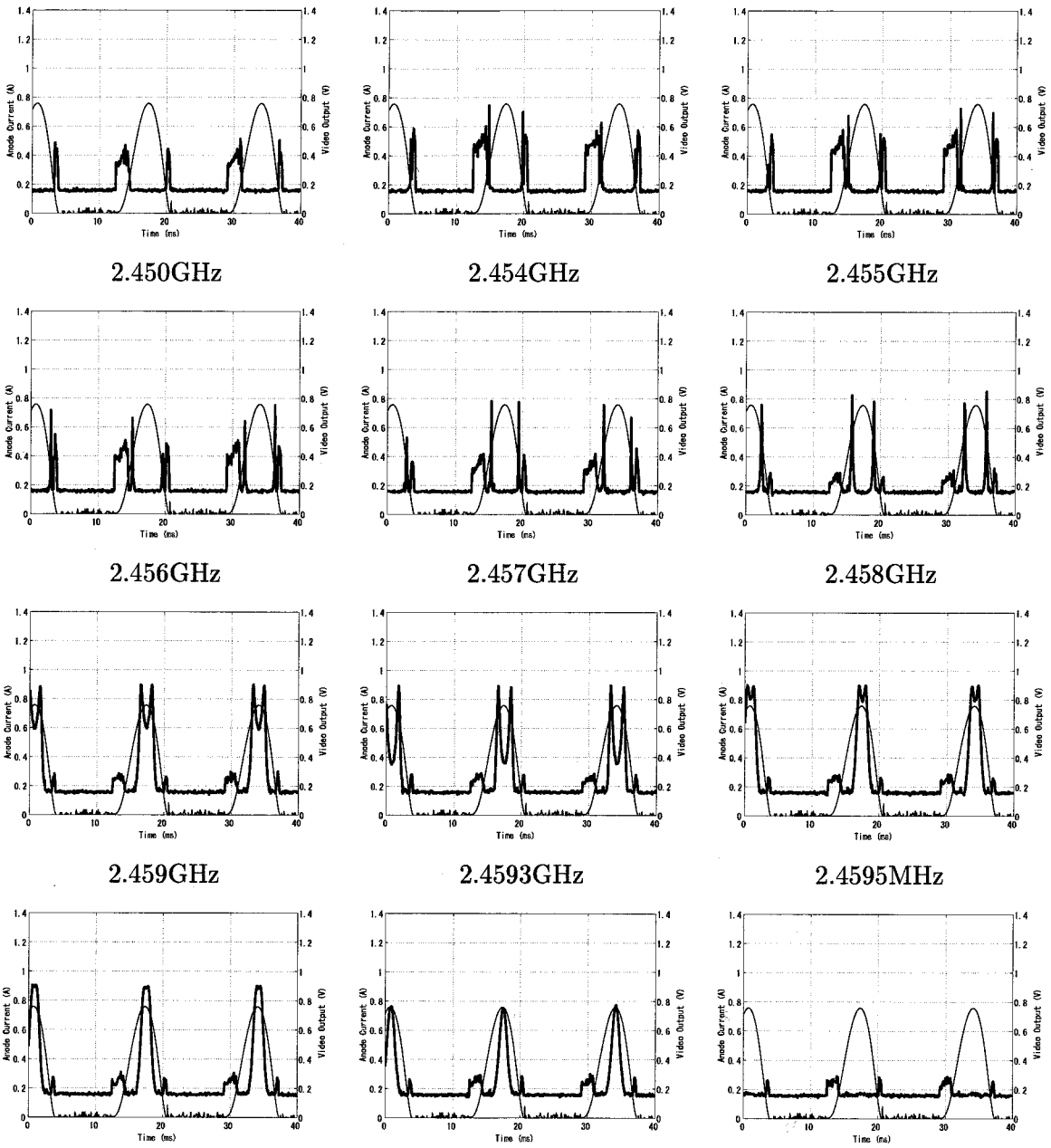

Figure A.2: Experimental results of the time domain analysis in the fundamental bands (2). Thick line and right axis: video output signal from the spectrum analyzer, thin line and left axis: the corrected anode current waveform of the reference magnetron.

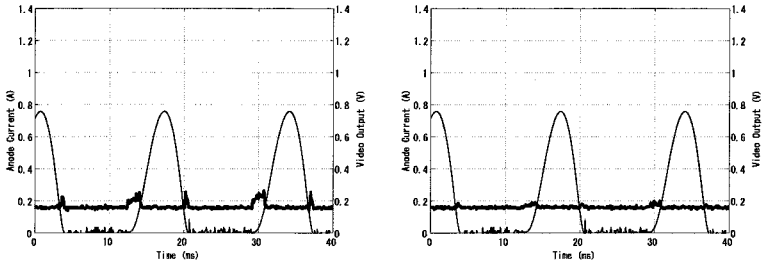

2.461GHz 2.465GHz

Figure A.3: Experimental results of the time domain analysis in the fundamental bands (3). Thick line and right axis: video output signal from the spectrum analyzer, thin line and left axis: the corrected anode current waveform of the reference magnetron.

A.2 Time domain analysis in the high frequency bands

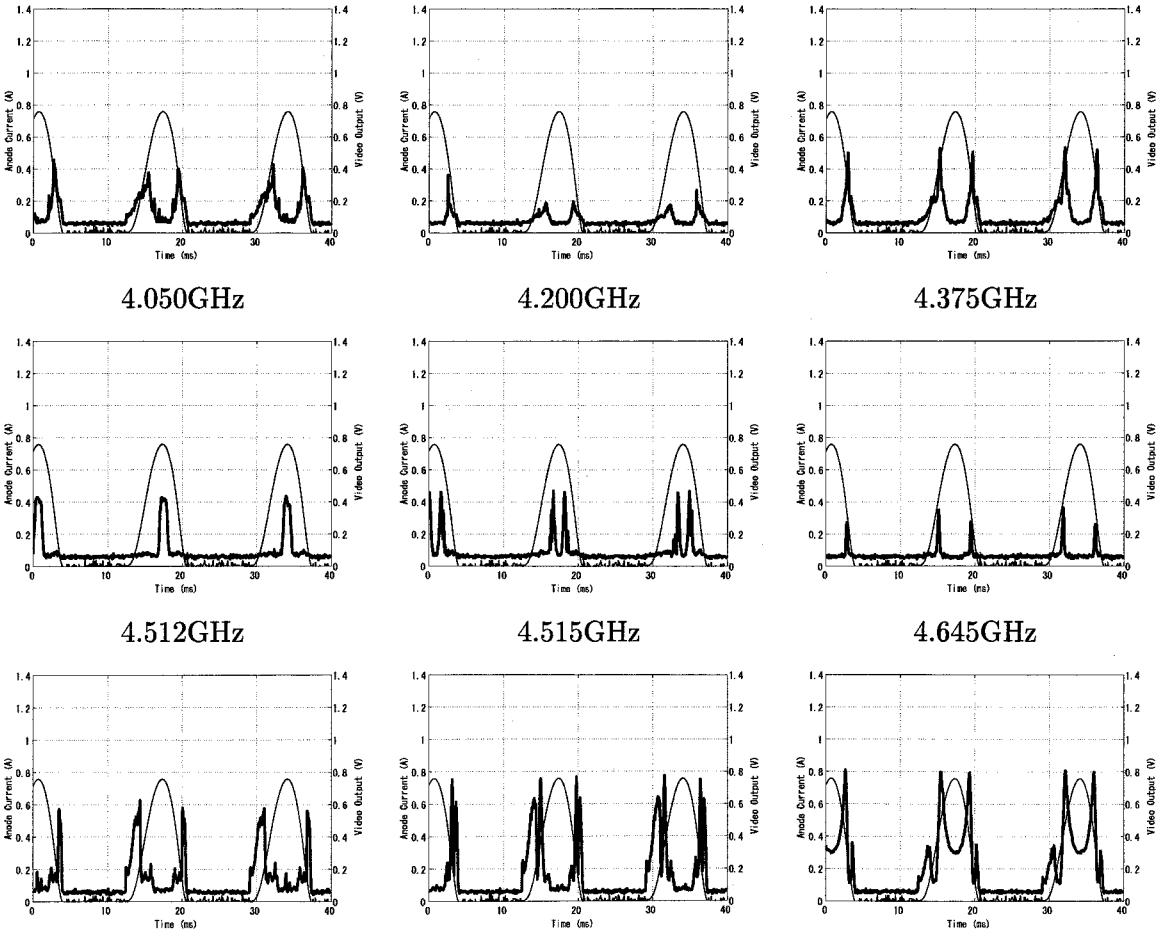

4.050GHz 4.200GHz 4.375GHz

4.512GHz 4.515GHz 4.645GHz

4.900GHz 4.910GHz 4.915GHz

Figure A.4: Experimental results of the time domain analysis in the high frequency bands (1). Thick line and right axis: video output signal from the spectrum analyzer, thin line and left axis: the corrected anode current waveform of the reference magnetron.

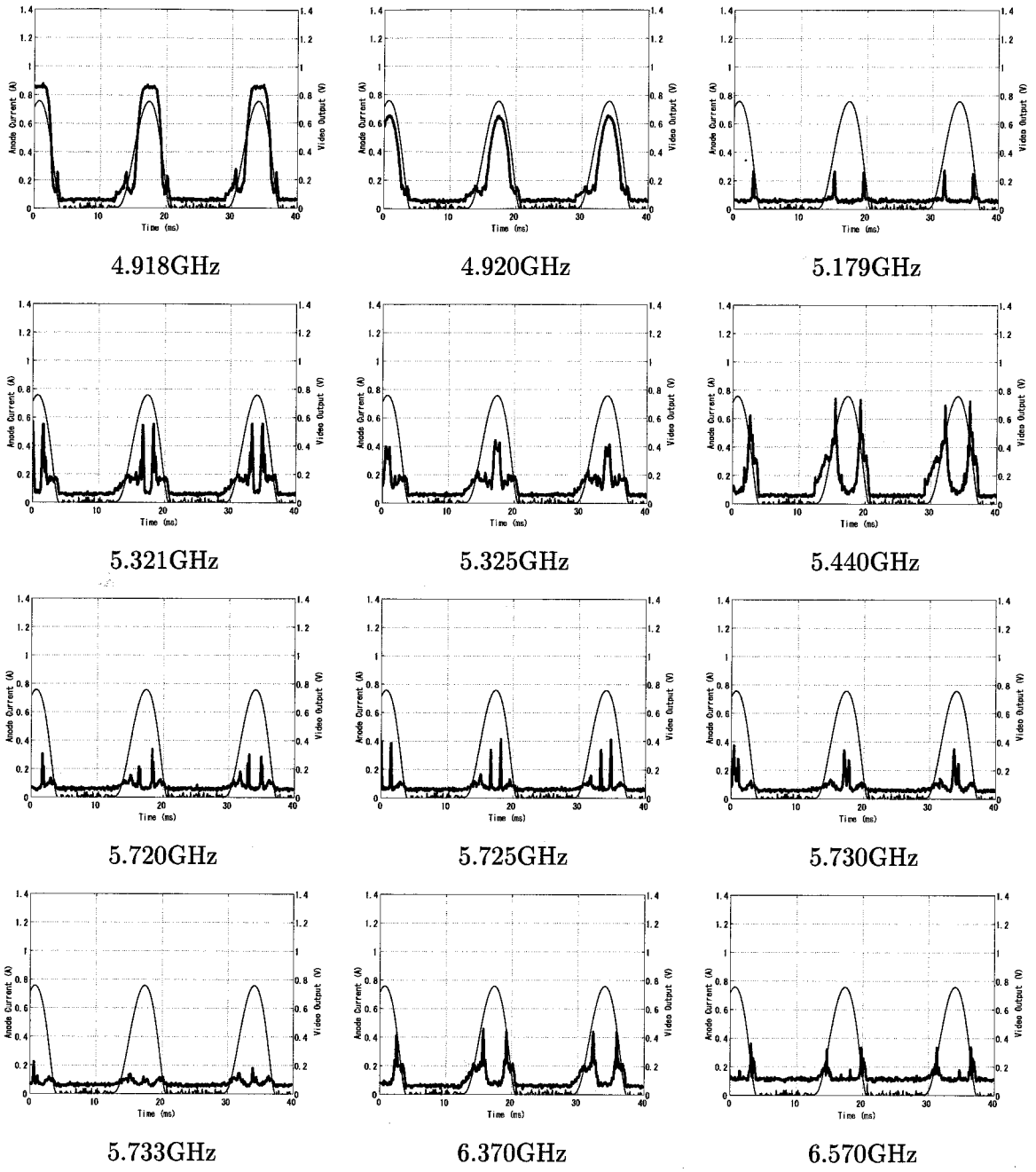

Figure A.5: Experimental results of the time domain analysis in the high frequency bands (2). Thick line and right axis: video output signal from the spectrum analyzer, thin line and left axis: the corrected anode current waveform of the reference magnetron.

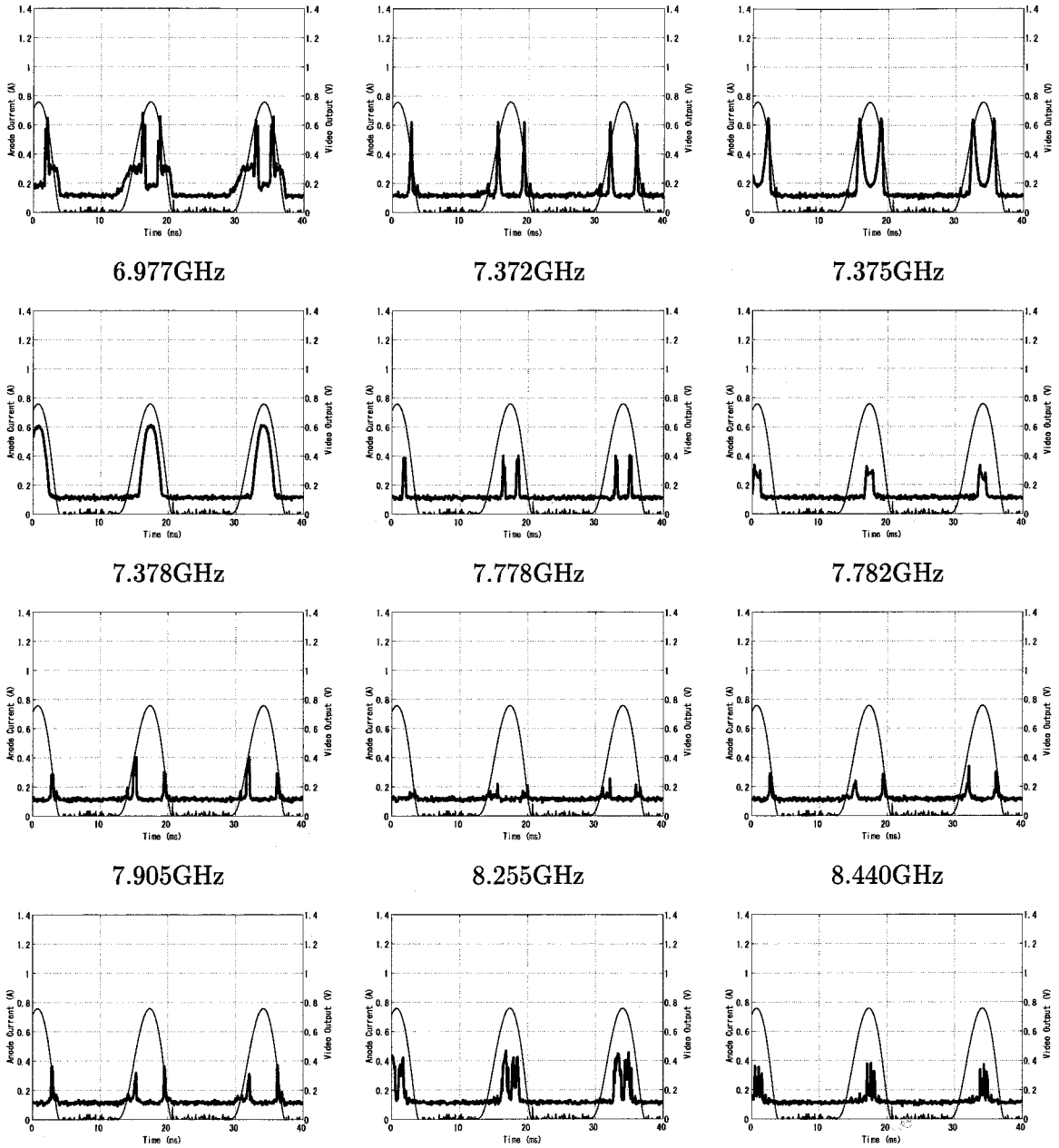

Figure A.6: Experimental results of the time domain analysis in the high frequency bands (3). Thick line and right axis: video output signal from the spectrum analyzer, thin line and left axis: the corrected anode current waveform of the reference magnetron.

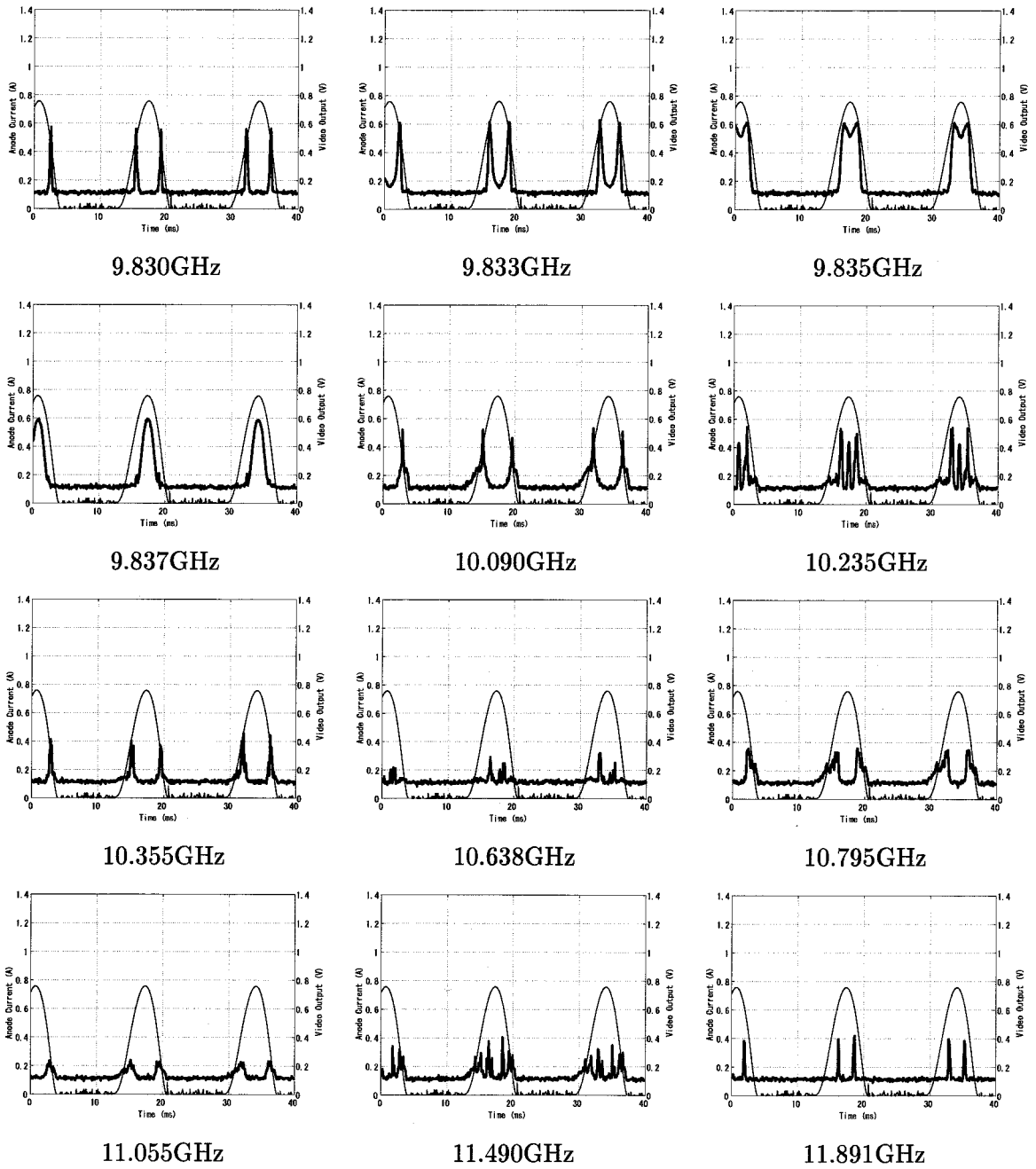

Figure A.7: Experimental results of the time domain analysis in the high frequency bands (4). Thick line and right axis: video output signal from the spectrum analyzer, thin line and left axis: the corrected anode current waveform of the reference magnetron.

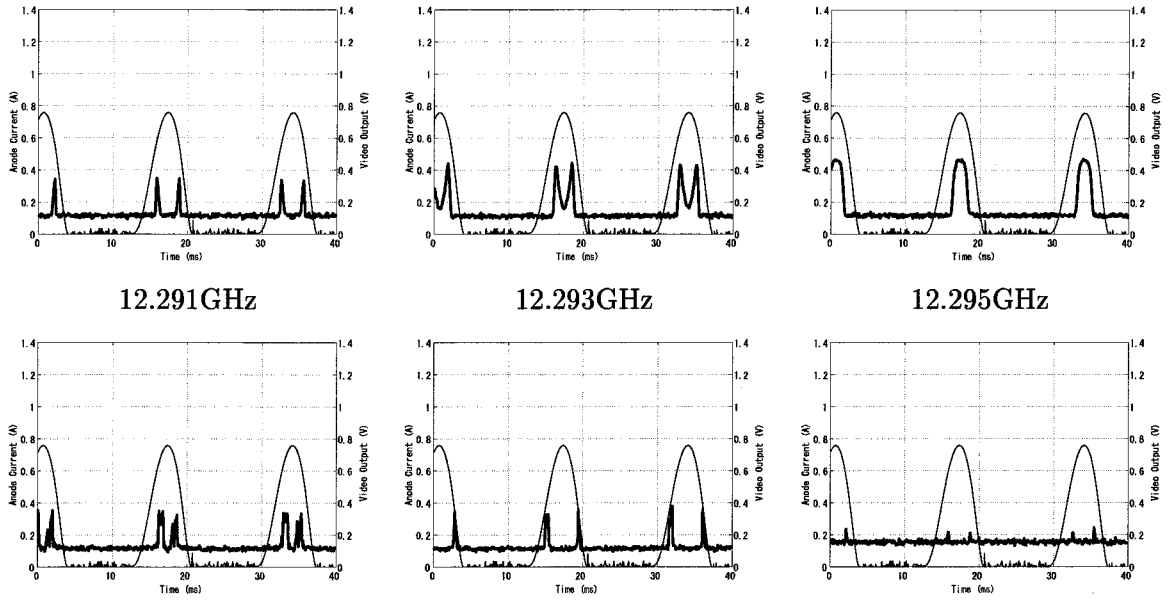

12.291GHz 12.293GHz 12.295GHz

12.695GHz 12.815GHz 13.225GHz

Figure A.8: Experimental results of the time domain analysis in the high frequency bands (5). Thick line and right axis: video output signal from the spectrum analyzer, thin line and left axis: the corrected anode current waveform of the reference magnetron.

A.3 Time domain analysis in the low frequency bands

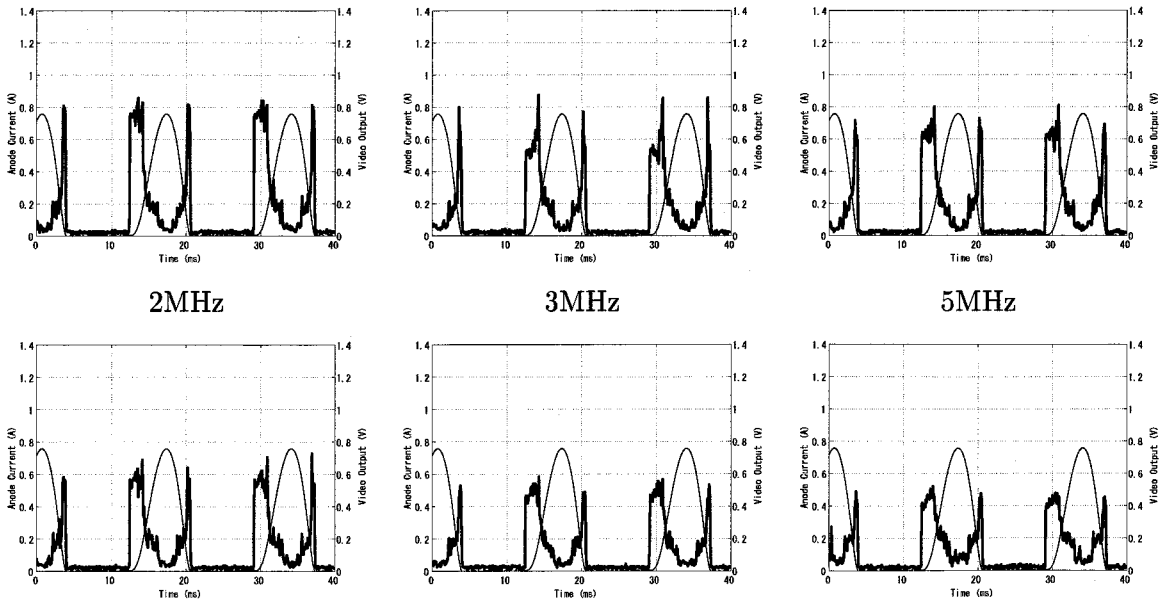

2MHz 3MHz 5MHz

7MHz 10MHz 15MHz

Figure A.9: Experimental results of the time domain analysis in the low frequency bands (1). Thick line and right axis: video output signal from the spectrum analyzer, thin line and left axis: the corrected anode current waveform of the reference magnetron.

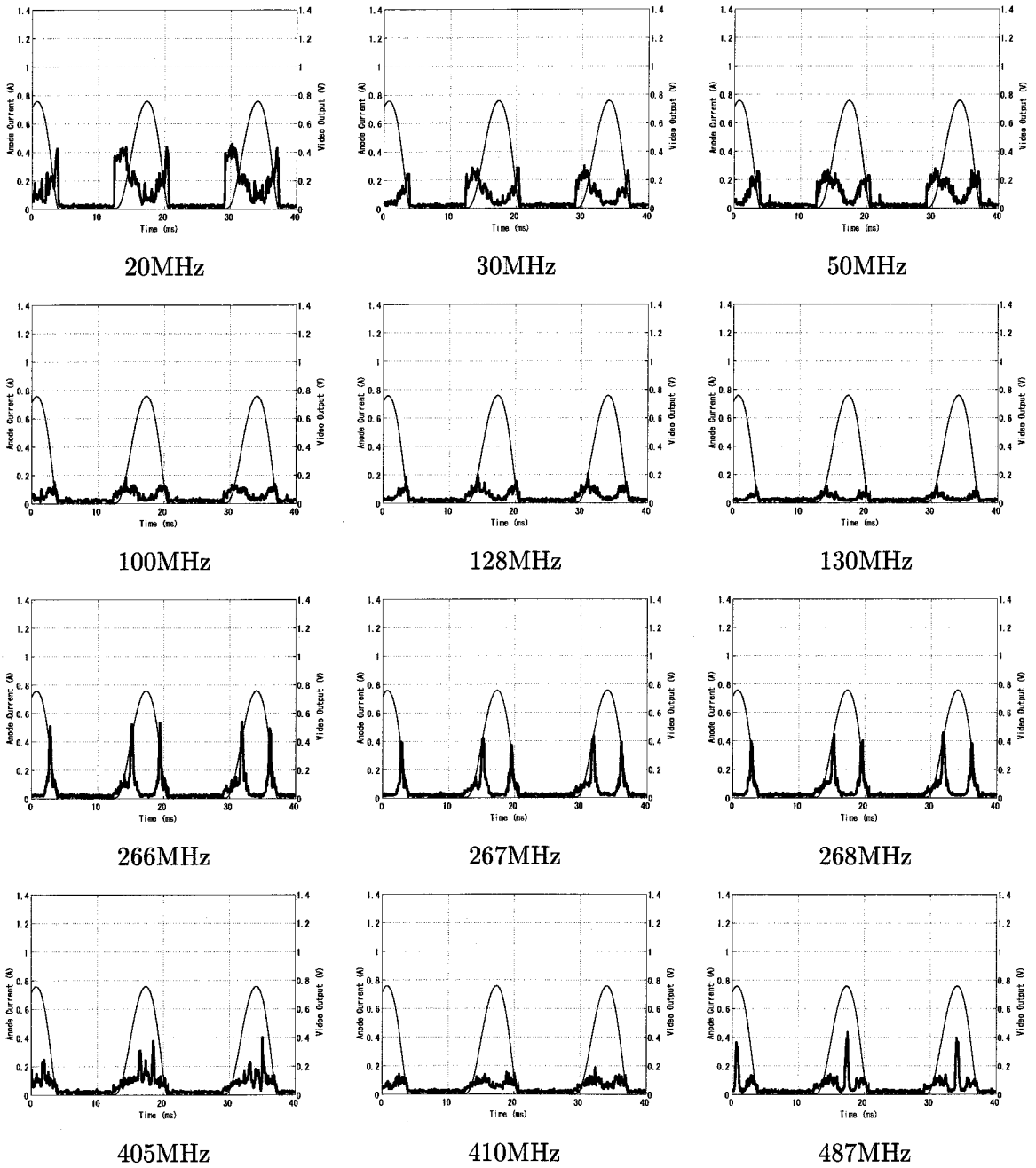

Figure A.10: Experimental results of the time domain analysis in the low frequency bands (2). Thick line and right axis: video output signal from the spectrum analyzer, thin line and left axis: the corrected anode current waveform of the reference magnetron.

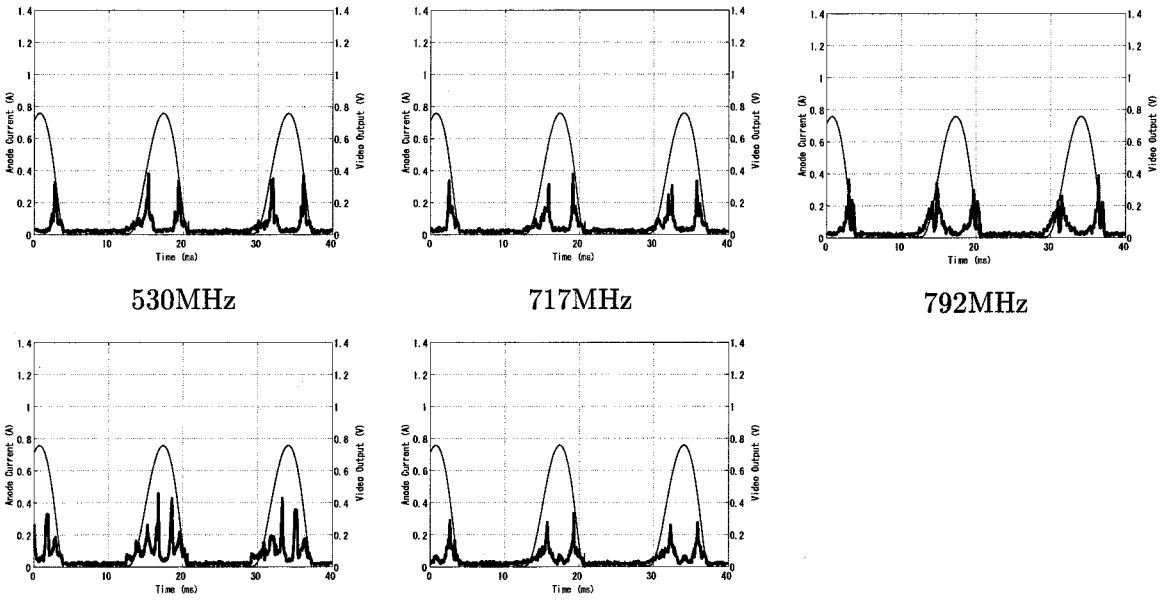

Figure A.11: Experimental results of the time domain analysis in the low frequency bands (3). Thick line and right axis: video output signal from the spectrum analyzer, thin line and left axis: the corrected anode current waveform of the reference magnetron.

Appendix B

EMC of a SPS Transmitting System with Other Radio Applications

Electromagnetic compatibility (EMC) between a SPS transmitting system and other radio applications such as satellite communication services, wireless communication systems, radio astronomy etc. is an important problem that has to be solved for the practical use of the SPS. In this appendix, we describe the EMC between a 1GW-class 2.45GHz SPS transmitting system and other radio applications, with numerical investigations on radiation levels from a SPS transmitting system.

In the present investigation, a magnetron is adopted as a transmitter of a 2.45GHz SPS. The harmonic levels generated from the 2.45GHz magnetron when it is operated by a DC stabilized power supply are put in Table B.1 [61,62]. The figures put in Table B.1 is seemingly low as an element, however in the case of 1GW-class 2.45GHz, the harmonics totally radiate a microwave power from several hundreds watt to the order of 10kW.

In the following sections, the higher level at the harmonics put in each row of Table B.1 is defined as the harmonic levels generated from the 2.45GHz magnetron. These harmonic levels are also adopted in previous EMC studies between a SPS and other radio applications [61, 77, 78], which we review in the next section.

Table B.1: Harmonic levels of a 2.45GHz magnetron [61,62].

Harmonics	Filament current: on	Filament current: off
2nd	-62.6dBc	-64.6dBc
3rd	-81.2dBc	-75.0dBc
4th	-74.6dBc	-82.9dBc
5th	-77.1dBc	-78.5dBc
6th	-72.1dBc	-72.1dBc
7th	-78.3dBc	-77.1dBc

In terms of the spurious noises excluding the harmonics, these levels are lower than those of the harmonics when the magnetron is driven in the filament-off operation, as shown in Fig. 5.12, and described in Sec. 5.4. Hence, the spurious noise levels excluding the harmonics are expected to be below -62.6dBc, which is the highest level of the harmonics as shown in Table B.1.

B.1 Preliminary study of EMC between a SPS and other radio applications

B.1.1 Reviews of previous studies

A study of EMC between a 2.45GHz or a 5.8GHz SPS and other radio applications has been conducted by Matsumoto *et al.* [61]. One of their discussions was EMC between the 2nd harmonic (4.9GHz) and a 5GHz-band microwave relay system. In their study, the radiation pattern of the 2nd harmonic from a SPS transmitting system is expected to be omnidirectional. The compatibility level of the 5GHz-band microwave relay system is considered to be $-193.6\text{dBW/m}^2/4\text{kHz}$, and they have concluded that the 2nd harmonic from a 1GW-class SPS met the compatibility level considering the attenuation of -67.3dB by the directivity of the 5GHz-band microwave relay system.

A study of EMC between a 2.45GHz SPS and a fixed satellite service (FSS) has been conducted by Hatsuda *et al.* [77,78]. They have mentioned that "We have found that interference constraints in the 12.25-GHz bands are relatively severe". According to the interference budget calculation between the 5th harmonic of a SPS transmitting system and a FSS satellite for 12.25GHz conducted by Hatsuda *et al.* quoted in Fig. B.1 [77], their quantitative conclusion is shown in the column of "Required improvement value" in Fig. B.1; 28.8dB suppression of the 5th harmonic from the SPS transmitting system is necessary to meet the compatibility level of the FSS satellite.

Hatsuda *et al.* [77] have also mentioned EMC between the 2nd harmonic of a 2.45GHz SPS and 4.95GHz-band radio astronomy. Although the allocated frequency to the 4.95GHz-band radio astronomy is slightly different from the 2nd harmonic *i.e.* 4.9GHz-band, the required level is estimated to be 94.20dB, if the 2nd harmonic of a 2.45GHz SPS come close to the allocated frequency to the 4.95GHz-band radio astronomy. In this case, a phase-controlled magnetron (PCM) described in Sec. 1.4 is the key technology for satisfying the EMC with 4.95GHz-band radio astronomy. When the carrier frequency of a PCM is locked, the n-th harmonics of the PCM are also locked to the n-fold frequencies of the carrier frequency. Therefore, we conclude that a stable PCM in frequency is indispensable for satisfying the EMC with the 4.95GHz-band radio astronomy.

Table 2. Interference budget (*D/U*) calculation between SPS (*U*) and FSS satellite (*D*), for *f* = 12.25 GHz.

Items	Units	SPS (*U*)	FSS(*D*)
Frequency	GHz	12.25	12.25
Transmitter power	dBW	98.3 – 77.1[1] = 21.2	15.0
Branching loss	dB	10.0	1.0
Back off	dB		–22.0
Transmitting antenna gain	dB	40.0	46.5
Transmitting EIRP	dBW	51.2	38.5
Free space loss	dB	205.3	205.3
Rain attenuation loss	dB	0.0	–10.0[2]
(FSS) Receiving antenna gain	dB	21.5[3]	45.4
Branching loss	dB	1.0	1.0
(FSS) Receiver input level	dBW	–133.6	–132.4
D/U	dB	1.2	
Required *D/U*	dB	30.0	
Required improvement value	dB	28.8	

[1]*Fifth harmonics value –77.1 dBc.*
[2]*Worst case, i.e., FSS is suffered by rain att.*
[3]*Satellite separation angle is 2°.*

Figure B.1: Interference budget (D/U) calculation between a SPS (U) and a FSS satellite (D) for 12.25GHz [77].

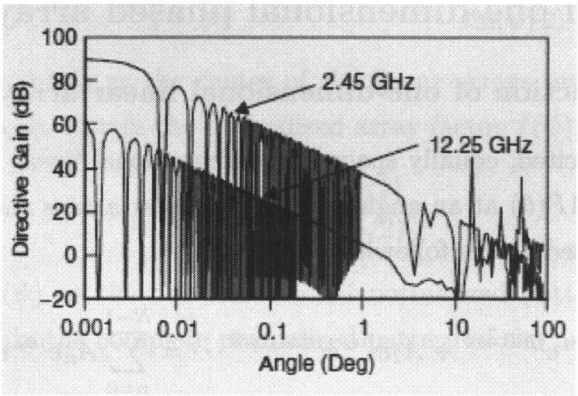

Figure B.2: Sidelobe characteristics of a fundamental (2.45GHz) patch array ,TM110, at the fundamental frequency and the 5th harmonic (12.25GHz) [77].

B.1.2 Phase control of the harmonics

In the calculation by Hatsuda *et al.*, the 5th harmonic has been also beam-controlled by a phased array system of the SPS transmitting system as well as the carrier frequency, as shown in Fig. B.2 [77]. Then, they have considered service area separation between the FSS Earth-stations and the SPS, and finally they have estimated 40.0dB as "Transmitting antenna gain" in the 12.25GHz band.

Their thorough investigations are significantly valuable since they deal with the worst case of the SPS transmitting system interfering with radio applications. In practice, however, the harmonics are unlikely to be focused to a particular direction with phased arrays, owing to the following reasons;

- Even if each electric length from an oscillator to an antenna is adjusted within an error of $a\%$ to the carrier frequency, errors of the electric lengths to the n-th harmonics spread to $na\%$.

- Features of a phase shifter, which is necessary for a SPS transmitting system to control and focus a microwave beam by active phased arrays, will not be guaranteed against the frequency bands of the n-th harmonics.

Therefore, in the present study, we introduce a concept that microwave power of the harmonics is not focused to a particular direction, as a realistic estimation. A method for realizing the concept above can be easily imagined; each antenna element has a random phase, that is to say, the SPS transmitting antennas consist of random phased arrays. In the next section, one-dimensional linear arrays with uniformly excited, equally spaced, and random phased antennas are adopted as a simulation model, and numerical simulations of radiation patterns of the harmonics from a SPS transmitting system are conducted.

B.2 Expressions of one-dimensional phased arrays

B.2.1 General introduction of one-dimensional linear arrays

A schematic of uniformly excited, equally spaced, one-dimensional linear arrays is shown in Fig. B.3. The array factor $AF(\theta)$ at an angle of θ of the linear arrays shown in Fig. B.3 in the far-field region is expressed as the following [79];

$$AF(\theta) = A_0 e^{j\alpha_0} + A_1 e^{j\alpha_1} e^{j\beta d\cos\theta} + A_2 e^{j\alpha_2} e^{j\beta 2d\cos\theta} \cdots = \sum_{n=0}^{N-1} A_n e^{j\alpha_n} e^{j\beta nd\cos\theta}, \qquad \text{(B.1)}$$

where α_n is the phase of the element n, and A_n is the amplitude of the element n, N is the number of elements, and β is the wave number $\beta = 2\pi/\lambda$ where λ is the wave length. Considering uniformly excited linear arrays, $A_0 = A_1 = A_2 = \cdots = A_n = A$, then Eq. (B.1)

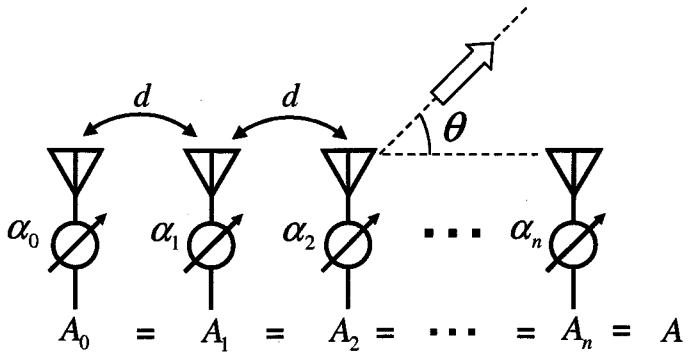

Figure B.3: Uniformly excited, equally spaced, one-dimensional linear arrays. d: distance between the elements, α_n: phase of the element n, and A_n: amplitude of the element n. Considering uniformly excited linear arrays, $A_0 = A_1 = A_2 = \cdots = A_n$.

becomes

$$AF(\theta) = A \sum_{n=0}^{N-1} e^{j\alpha_n} e^{j\beta n d \cos\theta}. \tag{B.2}$$

In the case of the carrier frequency of the SPS transmitting system, the microwave beam should be focused on the SPS receiving site accurately. One of the easiest ways to focus the beam on the SPS receiving site is to introduce linear phase progression. Then, α_n is equal to be $n\alpha$, therefore Eq. (B.2) becomes

$$AF(\theta) = A \sum_{n=0}^{N-1} e^{jn(\beta d \cos\theta + \alpha)} = A \sum_{n=0}^{N-1} e^{jn\psi}, \tag{B.3}$$

where we define $\psi = \beta d \cos\theta + \alpha$. Then, multiplying Eq. (B.3) by $e^{j\psi}$ and subtracting this from Eq. (B.3), the array factor is expressed in the following;

$$AF(\theta) = A\frac{1 - e^{jN\psi}}{1 - e^{j\psi}} = Ae^{j(N-1)\psi/2}\frac{\sin(N\psi/2)}{\sin(\psi/2)}. \tag{B.4}$$

Defining the coordinate origin as the center of the linear arrays, we can neglect the phase factor $e^{j(N-1)\psi/2}$. Thus, we obtain the normalized array factor $f(\psi)$;

$$f(\psi) = \frac{\sin(N\psi/2)}{N\sin(\psi/2)}. \tag{B.5}$$

When we define $g_a(\psi)$ as the one-dimensional normalized pattern of a single element antenna, finally we obtain the complete normalized pattern of the array $F(\psi)$;

$$F(\psi) = g_a(\psi) f(\psi). \tag{B.6}$$

Eq. (B.6) also expresses the normalized beam pattern of a typical SPS transmitting system at the carrier frequency, because a SPS transmitting system is considered to be uniformly

excited, equally spaced linear arrays with linear phase progression, except that the transmitting system consists of two-dimensional arrays. Even in the case of the two-dimensional arrays, the generality is maintained by expanding the process on the one-dimensional arrays described above into the two-dimensional arrays.

B.2.2 Beam pattern formed by random phased linear arrays

Now we analyze the beam pattern of the harmonics which is formed by random phased linear arrays.

Let us start from Eq. (B.2), the array factor of uniformly excited, equally spaced one-dimensional linear arrays. Note that $e^{j\alpha_n}e^{j\beta nd\cos\theta}$ in the summation on the right-hand side of Eq. (B.2) only has the phase factor. The term $e^{j\beta nd\cos\theta}$ expresses the regular phase rotation by increasing the element number n. On the other hand, the term $e^{j\alpha_n}$ can be independently set up as an active phase term of the phased arrays.

Here we assume that α_n is defined as a value in uniform random numbers between $0 \sim 2\pi$ in order to implement random phased arrays. Then, we can replace $e^{j(\alpha_n+\beta nd\cos\theta)}$ by $e^{j\gamma_n}$,where γ_n is also defined as a value in uniform random numbers between $0 \sim 2\pi$.

In the complex plane, $e^{j\gamma_n}$ is expressed as a vector line from the coordinate origin to unit circle with a complex argument of $\arg(\gamma_n)$. When we assume the number of antennas N goes to infinity, $\sum e^{j\gamma_n}$ means that the summation of vectors with unit length and uniformly-random complex arguments, therefore

$$\lim_{N\to\infty}\sum_{n=0}^{N} e^{j\gamma_n} = 0.$$

Finally, Eq. (B.2) becomes

$$AF(\theta) = \lim_{N\to\infty} A\sum_{n=0}^{N-1} e^{j\alpha_n}e^{j\beta nd\cos\theta} = A\lim_{N\to\infty}\sum_{n=0}^{N} e^{j\gamma_n} = 0. \tag{B.7}$$

The value 0 of the array factor shown in Eq. (B.7) has no physical meaning, since Eq. (B.7) directly means that any electromagnetic waves are not propagated from antenna arrays at all. That is inconsistent with energy conservation law in an arbitrary closed surface including antenna arrays. Therefore, Eq. (B.7) will be interpreted as an expression that the beam pattern is omnidirectional and independent of the beam angle θ, the distance of the elements d and even the wave length λ. The generality is maintained in the case of two-dimensional arrays.

Therefore, if we manage to set up random phased arrays for the spurious noises form a SPS transmitting system, the beam pattern will ideally be omnidirectional in no matter what frequency bands the spurious noises radiate.

B.3 Simulation parameters

Table. B.2 shows simulation parameters for the calculation of radiation patterns of the harmonics from a 1GHz-class and 2.45GHz SPS transmitting system.

The equations described in the previous section are valid when the SPS transmitting system is employed in the far-field region. The far-field condition is expressed in the following;

$$r_{\mathrm{ff}} = \frac{2D^2}{\lambda},$$

where r_{ff} is the minimum path length we can treat as the far-field region and D is the length of the line source [79].

In the case of the 2.45GHz SPS system put in Table. B.2, D is replaced to the diameter of the transmitting system. Then r_{ff} is calculated to be 1.63×10^7m and it is less than the transmission distance of 36000km, which is the distance from the GEO to the Earth. Therefore, the assumption on the far-field region above is reasonable.

A beam pattern of a single antenna is not considered in the simulations, since the main subject is to investigate only the array factor which is created by random phased arrays. The number of antenna elements is defined by the diameter of the SPS transmitting system divided by the distance between the elements.

Table B.2: simulation parameters for the calculation of radiation patterns of the harmonics from the SPS transmitting system. λ: wavelength at the carrier frequency ($\lambda \approx 0.1224$m).

Carrier Frequency	2.45GHz
Transmission distance	36,000km
Diameter of SPS transmitting system	1km
Distance between the elements	0.5λ
Number of antenna elements	16,333
Amplitude of each antenna	uniform
Phase of each antenna	random
Beam pattern of a single antenna	omnidirectional
Number of trials	60

B.4 Simulation results of radiation pattern with random phased arrays

Fig. B.4 shows a simulation result of the radiation pattern with random phased arrays normalized by the omnidirectional antenna gain.

The radiation pattern seems to be almost uniform; however, there are some peaks as one can be seen in Fig. B.4. This is because the number of antenna elements is finite and the

distribution of uniform random numbers which are given by software is not perfectly uniform, compared to the ideal case as expressed in Eq. (B.7).

From 60 simulation trials, the mean value and the standard deviation of the maximum radiation levels in the patterns is calculated to be 9.46dBi and 0.66dB, respectively. Therefore, the directivity of random phased array is estimated to about 10dBi, and we define 10dBi as the "worst" directional gain for the random phased arrays. (We use the word "worst" here because the purpose of the random phased arrays is to realize the omnidirectional beam pattern.) The peaks dose not always appear to the direction of the Earth *i.e.* the angle of 0 degree in Fig. B.4, and one can not predict their directions at all, because they randomly appear.

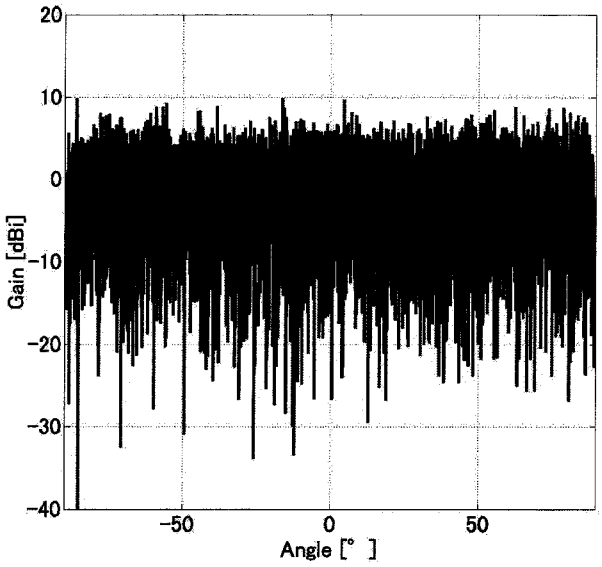

Figure B.4: A simulation result of the radiation pattern with random-phased array antennas.

B.5 Discussions

In this section, numerical calculations of the compatibility conditions at the frequency of the 2nd and the 5th harmonics are discussed. In the discussions, the 2.45GHz SPS transmitting power is 1GW (90dBW).

B.5.1 Case of the 2nd harmonic

The noise level of the 2nd harmonic is -62.6dBc as indicated in Table B.1. Then, the power density of the 2nd harmonic radiated from the SPS to the Earth is calculated in the following:

$$\frac{90\text{dBW} - 62.6\text{dBc}}{2\pi \times (36,000\text{km})^2} = -131.7\text{dBW/m}^2,$$

assuming the 2nd harmonic isotropically radiates in the hemisphere of the Earth's side owing to the random phased arrays.

Then, the bandwidth Δf of the carrier frequency f is derived from the Q value of the magnetron spectrum $Q = f/\Delta f$. As described in Sec. 5.3, $Q = 1.1 \times 10^5$ in the case of the filament-off magnetron, hence Δf is calculated to be 22kHz. Then, the bandwidth of the 2nd harmonic is estimated to be twice as wide as that of the carrier frequency *i.e.* 44kHz, since the harmonics are generated by the distortion of the fundamental, and the 2nd harmonic is estimated to be twice as wide as that of the carrier frequency. Besides, considering the worst directional gain of 10dBi for the random phased arrays, and the attenuation of -67.3dB by the directivity of the 5GHz-band microwave relay system, the received power density on the 5GHz-band microwave relay system from the SPS transmitting system is calculated in the following;

$$(-131.7\text{dBW/m}^2 + 10\text{dBi} - 67.3\text{dB}) \times \frac{4\text{kHz}}{44\text{kHz}} = -199.4\text{dBW/m}^2/4\text{kHz}.$$

In conclusion, the 2nd harmonic from the SPS meets the compatibility level against $-193.6\text{dBW/m}^2/4\text{kHz}$, the 5GHz-band microwave relay system, when random phased arrays are applicable to the harmonic components of the SPS transmitting system.

B.5.2 Case of the 5th harmonic

With regard to the EMC between the 5th harmonic from a 1GW-class SPS transmitting system and a FSS, the figures in Fig. B.1 are adopted for discussions. It was mentioned that the "Transmitting antenna gain" have been estimated to be 40.0dB [77, 78]. On the other hand, the transmitting antenna gain is estimated to be 10dB even in the worst case form the simulation results of the radiation pattern with random phased arrays. That means the transmitting antenna gain is subtracted from 30dB, and then the "Required improvement value" of 28.8dB in the calculation of Fig. B.1 can be compensated.

What we carefully take into consideration is that the "Transmitting antenna gain" includes the directional gain of a microstrip patch antenna [77, 78]; in contract, a beam pattern of a single antenna is omnidirectional *i.e.* 0dBi in the present simulations as shown in Table B.2. With respect to the antenna gain of the harmonics, an experimental study [80] has shown the antenna gain of the circular microstrip antenna (CMSA) for the 5th harmonic when the fundamental mode TM_{110} of the CMSA was designed at 2.45GHz. The experimental results have indicated that the resonance mode of the CMSA in the vicinity of the 5th harmonic was TM_{130}, and that its antenna gain was measured to be a few dBi. Hence, the directional gain of the CMSA for the 5th harmonic will have less impact on the complete pattern of the SPS transmitting arrays. Besides, power loss at a frequency of the 5th harmonic in a SPS transmitting system will compensate the difference or it will reduce the 5th harmonic level away from the compatibility level against the FSS.

In conclusion, the 5th harmonic from the SPS also satisfies the compatibility level against the FSS, when random phased arrays are applicable to the harmonic components of the SPS transmitting system.

B.6 Summary

From the numerical simulations and calculations, we conclude that the 2nd and 5th harmonic from the SPS both meet the compatibility levels against the 5GHz-band microwave relay system and the FSS, respectively, when random phased arrays are applicable to the harmonic components of the SPS transmitting system. Although we discuss only two cases of EMC, the worst directional gain of 10dBi indicated in Sec. B.4 is applicable to the spurious noises from the SPS transmitting system in any frequency bands, when the phases of antenna elements in the SPS transmitting system are deemed to be set at random. Therefore, works in this appendix will be effectively utilized as a means of estimating the radiation levels of the spurious noises from the SPS transmitting system.

EMC of a SPS transmitting system with other radio applications should be of course investigated more thoroughly for future works. Especially, EMC with radio applications at the carrier frequency of a SPS transmitting system is quite important and difficult problem, because the method of the random phased arrays can not be applied to the carrier frequency at all. In the case of a 2.45GHz SPS, EMC with 2.4GHz-band WLAN such as Bluetooth and IEEE 802.11b will be one of the most serious problems, which has also been pointed out by Matsumoto *et al.* [61] and Hatsuda *et al.* [77, 78]. Hatsuda *et al.* [77] has mentioned that "required improvement value" of a 2.45GHz SPS is almost 80dB. In the case of a 5.8GHz SPS, EMC with the ETC (Electronic Toll Collection) system has been a serious problem in Japan. Matsumoto *et al.* [61] has mentioned that a 5.8GHz SPS is required to let the sidelobe levels lower than 30dB than its present design to satisfy the EMC of the present 5.8GHz SPS transmitting system with ETC. Therefore, both the effective beam focusing and the suppression of sidelobes which satisfies EMC with other radio applications have to be established by the use of various techniques and algorithms for future works.

References

[1] A. W. Hull, "Effect of uniform magnetic field on the motion of electrons between co-axial cylinder," *Physical Review*, vol. 18, no. 1, pp. 31–57, 1921.

[2] S. Okamura, *History of Electronic Tubes (in Japanese).* Tokyo, Japan: Ohmsha, 1987.

[3] H. Saito, M. Kume, and T. Kawaguchi, "Improvement of Performance of Magnetron (in Japanese)," Toshiba Review, pp. 768–771, 1982.

[4] K. Yamamoto, H. Kuronuma, T. Koinuma, and N. Tashiro, "A Study of Magnetron Noise," *IEEE Transactions on Electron Devices*, vol. 34, no. 5, pp. 1223–1226, May 1987.

[5] A. Kohsaka, H. Saitoh, and T. Kawaguchi, "Low Profile and Clean Spectrum Magnetron," *Journal of Microwave Power and Electromagnetic Energy*, vol. 24, no. 1, pp. 3–13, 1989.

[6] K. Yamamoto, H. Kuronuma, T. Koinuma, and N. Tashiro, "Experimental Study of the Noise Generated from a Magnetron for Microwave Oven (in Japanese)," Technical Report of IEICE, MW80-33, pp. 23–28, 1980.

[7] Y. Matsumoto, M. Takeuchi, K. Fujii, A. Sugiura, and Y. Yamanaka, "A Time-Domain Microwave Oven Noise Model for the 2.4-GHz Band," *IEEE Transactions on Electromagnetic Compatibility*, vol. 45, no. 3, pp. 561–566, Oct. 2003.

[8] Y. Matsumoto, "Wireless LAN (in Japanese)," *Special Section: Electromagnetic Compatibility in the Ubiquitous Network Age in the Journal of the IEICE*, vol. 87, no. 10, pp. 832–834, Oct. 2004.

[9] N. Tesla, "The transmission of electric energy without wires," in *The 13th Anniversary Number of the Electrical World and Engineer*, 1904.

[10] ——, *Experiments with Alternate Current of High Potential and High Frequency.* New York: McGraw Pub. Co., 1905.

[11] W. C. Brown, "The history of power transmission by radio waves," *IEEE Transactions on Microwave Theory and Techniques*, vol. 32, no. 9, pp. 1230–1242, Sept. 1984.

[12] H. Matsumoto, "Research on Solar Power Station and Microwave Power Transmission in Japan: Review and perspectives," *IEEE Microwave Magazine*, vol. 3, no. 4, pp. 36–45, Dec. 2002.

[13] N. Kaya, H. Matsumoto, S. Miyatake, I. Kimura, M. Nagatomo, and T. Obayashi, "Nonlinear Interaction of Strong Microwave Beam with the Ionosphere MINIX Rocket Experiment," *Space Power*, vol. 6, pp. 181–186, 1986.

[14] H. Matsumoto and T. Kimura, "Nonlinear Excitation of Electron Cyclotron Waves by a Monochromatic Strong Microwave: Computer Simulation Analysis of the MINIX Results," *Space Power*, vol. 6, pp. 187–191, 1986.

[15] N. Kaya, H. Matsumoto, and R. Akiba, "Rocket Experiment METS Microwave Energy Transmission in Space," *Space Power*, vol. 11, no. 3&4, pp. 267–274, 1992.

[16] N. Shinohara and H. Matsumoto, "Experimental study of large rectenna array for microwave energy transmission," *IEEE Transactions on Microwave Theory and Techniques*, vol. 46, no. 3, pp. 261–268, Mar. 1998.

[17] A. Celeste, "Overview of French Activities including Réunion Microwave Power Transmission (presentation slides)," in *Proc. of 4th SPS Symposium*, Kobe, Japan, Nov. 2002, pp. 9–13.

[18] N. Kaya, T. Matsushima, N. Marzwell, and J. Mankins, "Hawaii Project for Microwave Power Transmission (in Japanese)," in *Proc. of 4th SPS Symposium*, Kobe, Japan, Nov. 2002, pp. 137–142.

[19] T. Itoh, Y. Fujino, and M. Fujita, "Fundamental Experiment of a Rectifier Circuit of Rectenna Array for Microwave Power Reception," *IEICE Transactions on Communications*, vol. E76-B, no. 12, pp. 450–1513, Dec. 1993.

[20] V. Vanke and V. Savin, "Cyclotron wave converter for SPS energy transmission system," in *Proc. of International Symposium SPS '91 Power from Space*, Paris, France, 1991, pp. 515–520.

[21] V. Vanke, H. Matsumoto, N. Shinohara, and A. Kita, "Cyclotron wave converter of microwaves into dc," *IEICE Transactions on Electronics*, vol. E81-C, no. 7, pp. 1136–1142, 1987.

[22] R. Y. Miyamoto and T. Itoh, "Retrodirective Arrays for Wireless Communications," *IEEE Microwave Magazine*, vol. 3, no. 1, pp. 71–79, Mar. 2002.

[23] F. E. Little, S. J. Kokel, C. T. Rodenbeck, K. Chang, G. D. Arndt, and P. H. Ngo, "Development of a Retrodirective Control Transmitter for Wireless Power Transmission," *The Radio Science Bulletin*, no. 311, pp. 38–46, Dec. 2004.

[24] K. Hashimoto, K. Tsutsumi, H. Matsumoto, and N. Shinohara, "Space Solar Power System Beam Control with Spread-Spectrum Pilot Signals," *The Radio Science Bulletin*, no. 311, pp. 31–37, Dec. 2004.

[25] K. Hirayama, "Study on Wireless Power Transmission System for a Search Rbot in a Gas Pipe (in Japanese)," Master Thesis in Kyoto University, 1999.

[26] H. Kouno, "Study on Transmitting and Receiving Antennas of Wireless Power Transmission System for an Electric Vehicle (in Japanese)," Master Thesis in Kyoto University, 1998.

[27] ——, "The Study of Microwave Energy Transmission System to Moving Electric Vehicle (in Japanese)," Master Thesis in Kyoto University, 2000.

[28] N. Shinohara, T. Mitani, and H. Matsumoto, "Study on Ubiquitous Power Source with Microwave Power Transmission (in press)," in *Proc. of XXVIIIth General Assembly of the International Union of Radio Science (URSI GA)*, New Delhi, India, Oct. 2005.

[29] T. Kimura, Y. Omura, and H. Matsumoto, "Impacts of Oil Production Decline on Japanese Food Supply," *Japan Solar Energy Society*, vol. 31, no. 2, pp. 31–57, 2005.

[30] P. E. Glaser, "Power from the Sun; Its Future," *Science*, vol. 162, pp. 857–861, 1968.

[31] P. E. Glaser, F. P. Davidson, and K. Csigi, *Solar Power Satellites.* England: John Wiley & Sons Ltd, 1998.

[32] DOE and NASA report, "Satellite Power System; Concept Development and Evaluation Program," *Reference System Report*, Oct. 1978.

[33] J. C. Mankins, "A Fresh Look at the Concept of Space Solar Power," in *Proc. Space Power Systems Conference (SPS'97)*, Montreal, Canada, Aug. 1997, p. S7041.

[34] L. Summerer and F. Ongaro, "Solar Power from Space – Validation of Options for Future," in *Proc. of 4th International Conference on Solar Power from Space (SPS'04)*, Granada, Spain, June 2004, pp. 17–26.

[35] M. Mori, H. Kagawa, H. Nagayama, and Y. Saito, "Current Status of Study on Hydrogen Production with Space Solar Power Systems (SSPS)," in *Proc. of 4th International Conference on Solar Power from Space (SPS'04)*, Granada, Spain, June 2004, pp. 3–9.

[36] Y. Kobayashi, T. Saito, K. Ijichi, and H. Kanai, "Space Solar Power System for Terrestrial Power Utilities," in *Proc. of 4th International Conference on Solar Power from Space (SPS'04)*, Granada, Spain, June 2004, pp. 11–15.

[37] S. Sasaki, K. Tanaka, and USEF SSPS Study Team, "Tethered Solar Power Satellite for the Near-term Demonstration Experiments," in *Proc. of 4th International Conference on Solar Power from Space (SPS'04)*, Granada, Spain, June 2004, pp. 219–224.

[38] L. Sivan, *Microwave Tube Transmitters.* London: Chapman & Hall, 1994, ch. 6.

[39] R. Adler, "A study of locking phenomena in oscillators," *Proceedings of the IRE*, vol. 34, pp. 351–357, June 1946.

[40] W. C. Brown, "Update on the solar power satellite transmitter design," *Space Power*, vol. 6, pp. 123–135, 1986.

[41] ——, "The SPS transmitter Designed around the Magnetron Directional Amplifier," *Space Power*, vol. 7, no. 1, pp. 37–49, 1988.

[42] M. C. Hatfield, "Characterization and Optimization of the Magnetron Directional Amplifier," Ph.D. dissertation, the University of Alaska Fairbanks, 1999.

[43] N. Shinohara, T. Mitani, and H. Matsumoto, "Development of Phase-Controlled Magnetron (in Japanese)," *IEICE Transactions on Electronics*, vol. J84-C, no. 3, pp. 199–206, Nov. 2001.

[44] N. Shinohara, H. Matsumoto, and K. Hashimoto, "Solar Power Station/Satellite (SPS) with Phase Controlled Magnetrons," in *Proc. of Asia-Pacific Microwave Conference (APMC 2002), Vol.2*, Kyoto, Japan, Nov. 2002, pp. 795–6798.

[45] ——, "Solar Power Station/Satellite (SPS) with Phase Controlled Magnetrons," *IEICE Transactions on Electronics*, vol. E86-C, no. 8, pp. 1550–1555, Aug. 2003.

[46] H. Matsumoto, K. Hashimoto, N. Shinohara, and T. Mitani, "Experimental Equipments for Microwave Power Transmission in Kyoto University," in *Proc. of 4th International Conference on Solar Power from Space (SPS'04)*, Granada, Spain, June 2004, pp. 131–138.

[47] N. Shinohara, H. Matsumoto, E. Fujiwawa, Y. Takahashi, N. Tanaka, and K. Saga, "Small and Light Weight Microwave Power Transmitter COMET (in Japanese)," in *Proc. of 6th SPS Symposium*, Shizuoka, Japan, Oct. 2003, pp. 75–80.

[48] N. Shinohara and H. Matsumoto, "Phased Array Technology with Phase and Amplitude Controlled Magnetron for Microwave Power Transmission," in *Proc. of 4th International Conference on Solar Power from Space (SPS'04)*, Granada, Spain, June 2004, pp. 117–124.

[49] N. Shinohara, T. Mitani, and H. Matsumoto, "Development of Phase and Amplitude Controlled Magnetron," in *Proc. Sixth International Vacuum Electronics Conference (IVEC 2005)*, Noordwijk, Netherlands, Apr. 2005, pp. 61–64.

[50] S. Kato, "Study on Development of Phase and Amplitude Controlled Magnetron (in Japanese)," Master Thesis in Kyoto University, 2004.

[51] W. C. Brown, "Beamed Microwave Power Transmission and its Application to Space," *IEEE Transactions on Microwave Theory and Techniques*, vol. 40, no. 6, pp. 1239–1250, June 1992.

[52] I. Langmuir, "The Effect of Space Charge and Residual Gases on Thermionic Currents in High Vacuum," *Phys. Rev.*, vol. 2, pp. 450–486, 1913.

[53] I. Langmuir and K. B. Blodgett, "Currents Limited by Space Charge between Coaxial Cylinders," *Phys. Rev.*, vol. 22, pp. 347–356, 1923.

[54] M. Nakajima, *Microwave Engineering (in Japanese).* Tokyo: Morikita, 1975.

[55] I. Langmuir, "The Effect of Space Charge and Initial Velocities on the Potential Distribution and Thermionic Current between Parallel Plane Electrodes," *Phys. Rev.*, vol. 21, pp. 419–435, 1923.

[56] J. Ishikawa, *Science and Technology of Charged Particle Beams (in Japanese).* Tokyo: Corona Publishing Co., Ltd., 2001.

[57] N. Hamada and M. Wada, *Electron Tube Engineering (in Japanese).* Tokyo: Corona Publishing Co., Ltd., 1957.

[58] J. C. Slater, *Microwave electronics.* New York: D. Van Nostrand, 1950, ch. 13.

[59] F. F. Chen, *Introduction to plasma physics.* New York: Plenum Press, 1974.

[60] S. Tomonaga and M. Kotani, *Study of a UHF magnetron (in Japanese).* Tokyo, Japan: Misuzu Shobou, 1952.

[61] H. Matsumoto, K. Hashimoto, and N. Shinohara, "Frequency problem for Microwave Power Transmission (in Japanese)," in *Proc. of 3rd SPS Symposium*, Sapporo, Japan, Oct. 2000, pp. 21–31.

[62] T. Mitani, N. Shinohara, H. Matsumoto, M. Aiga, and T. Tsukada, "Study about increasing DC-RF Efficiency and reducing Noises of Magnetron for Microwave Power Transmission (in Japanese)," in *Proc. of 3rd SPS Symposium*, Sapporo, Japan, Oct. 2000, pp. 65–69.

[63] G. B. Collins, *Microwave Magnetron.* New York: Mcgraw-Hill Book Company, Inc., 1948.

[64] R. C. Davidson, *Physics of Nonneutral Plasmas.* Redwood City, CA: Addison-Wesley Publishing Company, 1990, ch. 4.

[65] L. S. Brown and G. Gabrielse, "Geonium theory: Physics of a single electron or ion in a Penning trap," *Reviews of Modern Physics*, vol. 58, no. 1, pp. 233–311, Jan. 1986.

[66] V. B. Neculaes *et al.*, "Magnetic Perturbation Effects on Noise and Startup in DC-Operating Oven Magnetrons," *IEEE Transactions on Electron Devices*, vol. 52, no. 5, pp. 864–871, May 2005.

[67] N. Shinohara and H. Matsumoto, "Possibility of Microwave Power Transmission System for Solar Power Station/Satellite (in Japanese)," in *Proc. of 4th SPS Symposium*, Tokyo, Japan, Oct. 2001, pp. 71–76.

[68] T. Ohnishi, "Research and Development of Electromagnetic Particle Code for Magnetrons (in Japanese)," Master Thesis in Kyoto University, 1997.

[69] A. Kita, "Study on Transmitting and Receiving Tubes for Microwave Power Transmission (in Japanese)," Master Thesis in Kyoto University, 1998.

[70] T. Fujieda, "Computer Experiments and Theoretical Analysis on Magnetrons (in Japanese)," Master Thesis in Kyoto University, 2000.

[71] H. Okita, "Computer Experiments on the Electromagnetic Interaction of Electrons in a Magnetron (in Japanese)," Master Thesis in Kyoto University, 2002.

[72] T. Hibino, "Study on Computer Experiments for Magnetrons (in Japanese)," Master Thesis in Kyoto University, 2003.

[73] S. Oohashi, "Computer Experiments on Magnetrons with 3D Electromagnetic Particle Code (in Japanese)," Master Thesis in Kyoto University, 2005.

[74] B. Goplen, L. Ludeking, D. Smithe, and G. Warren, "User-configurable MAGIC for electromagnetic PIC calculations," *Computer Physics Communications*, vol. 87, pp. 54–86, 1995.

[75] V. B. Neculaes *et al.*, "Low-Noise Microwave Oven Magnetrons With Fast Start-Oscillation by Azimuthally Varying Axial Magnetic Fields," *IEEE Transactions on Plasma Science*, vol. 32, no. 3, pp. 1152–1159, June 2004.

[76] J. I. Kim, J. H. Won, and G. S. Park, "Electron pre-bunching in microwave magnetron by electric priming using anode shape modification," in *Proc. Sixth International Vacuum Electronics Conference (IVEC 2005)*, Noordwijk, Netherlands, Apr. 2005, pp. 55–56.

[77] T. Hatsuda, K. Ueno, and M. Inoue, "Solar Power Satellite Interference Assessment," *IEEE Microwave Magazine*, vol. 3, no. 4, pp. 65–70, Dec. 2002.

[78] T. Hatsuda and K. Ueno, "Compatibility with Radio Communications – Interference Assessment to Space and Terrestrial Systems," in *Proc. of 2001 Asia-Pacific Radio Science Conference (AP-RASC'01)*, Tokyo, Japan, Aug. 2001, pp. 25–28.

[79] W. L. Stutzman and G. A. Thiele, *Antenna Theory and Design*, 2nd ed. the United States of America: John Wiley & Sons, Inc., 1998, ch. 3.

[80] Y. Yamada, Syarial, M. Omiya, and K. Itoh, "Characteristics of a Circular Microstrip Patch Antenna with Slits for Suppressing Re-radiation of Higher Harminics (in Japanese)," *IEICE Transactions on Communications*, vol. J81-B-II, no. 6, pp. 575–583, June 1998.

Publication Lists

Major Publications

1. Shinohara, N., T. Mitani, and H. Matsumoto, "Development of Phase-Controlled Magnetron (in Japanese)", IEICE Trans. Electron., vol.J84-C, no.3, pp.199–206, Mar. 2001.

2. Mitani, T., N. Shinohara, H. Matsumoto, K. Hashimoto, "Experimental Study on Oscillation Characteristics of Magnetrons after Turning off Filament Current (in Japanese)", IEICE Trans. Electron., vol.J85-C, no.11, pp.983–990, Nov. 2002.

2'. Mitani, T., N. Shinohara, H. Matsumoto, and K. Hashimoto, "Experimental Study on Oscillation Characteristics of Magnetrons after Turning off Filament Current (translated version into English)", John Wiley & Sons Inc., Electronics and Communications in Japan Part II. Electronics, vol.86 no.5, pp.1-9, May 2003.

3. Mitani, T., N. Shinohara, H. Matsumoto, and K. Hashimoto, "Improvement of Spurious Noises Generated from Magnetrons Driven by DC Power Supply after Turning off Filament Current", IEICE Trans. Electron., vol.E86-C, no.8, pp.1556–1563, Aug. 2003.

4. Mitani, T., N. Shinohara, H. Matsumoto, M. Aiga, N. Kuwahara, and T. Handa, "Time Domain Analysis of Noises Generated from Microwave Oven Magnetron (in Japanese)", IEICE Trans. Electron., vol.J87-C, no.12, pp.1146–1154, Dec. 2004.

4'. Mitani, T., N. Shinohara, H. Matsumoto, M. Aiga, N. Kuwahara, and T. Handa, "Time Domain Analysis of Noises Generated from Microwave Oven Magnetron (translated version into English)", John Wiley & Sons Inc., Electronics and Communications in Japan Part II. Electronics, Vol. 88, No.10, pp.28-36, 2005.

5. Mitani, T., N. Shinohara, H. Matsumoto, M. Aiga, N. Kuwahara, T. Handa and T. Ishii, "Noise Reduction Effects of an Oven Magnetron with a Cathode Shield on the High Voltage Input Side", IEEE Trans. Electron Devices, submitted.

Presentations in International Meetings

1. Mitani, T., N. Shinohara, H. Matsumoto, K. Hashimoto, M. Aiga, and T. Tsukada, "Study on Noises and Efficiency of Magnetron for Microwave Power Transmission", *2001 Asia-Pacific Radio Science Conference Digest*, p.280, Aug. 2001.

2. Mitani T., N. Shinohara, H. Matsumoto, K. Hashimoto, M. Aiga, and T. Tsukada, "Experimental Study on Noises and DC-RF Efficiency of Magnetron for Microwave Power Transmission", *Proceedings of the XXVIIth General Assembly of the International Union of Radio Science*, p.1459, Aug. 2002.

3. Matsumoto, H., K. Hashimoto, N. Shinohara, and T. Mitani, "SPORTS : Space Power Radio Transmission System", *Proceedings of the XXVIIth General Assembly of the International Union of Radio Science*, p.1493, Aug. 2002.

4. Mitani T., N. Shinohara, H. Matsumoto, K. Hashimoto, M. Aiga, and T. Tsukada, "Improvement of Noises Generated from Magnetrons Driven by DC Power Supply after Turning off Filament Current", *Proceedings of 2002 Asia-Pacific Microwave Conference*, vol.2, pp.1075–1078, Nov. 2002.

5. Matsumoto, H., N. Shinohara, K. Hashimoto and T. Mitani, "MPT and SPS Research at Radio Science Center for Space and Atmosphere, Kyoto University", *Proceedings of the 1st International Symposium on Sustainable Energy System*, p.40, Mar. 2003.

6. Mitani, T., N. Shinohara, H. Matsumoto, K. Hashimoto, M. Aiga, and T. Tsukada, "Time analysis of Frequency Spectrum Generated from Magnetron Driven by Non-Smoothing Half-Wave Voltage Doubler", *Proceedings of the 1st International Symposium on Sustainable Energy System*, p.40, Mar. 2003.

7. Mitani, T., N. Shinohara, H. Matsumoto, K. Hashimoto, M. Aiga, T. Tsukada, and T. Handa, "Experimental Study on Reduction of Noises Generated from Magnetron for Microwave Power Transmission", *Proceedings of 2003 Japan - United States Joint Workshop on Space Solar Power System (JUSPS'03)*, pp.204–205, Jul. 2003.

8. Matsumoto, H., K. Hashimoto, N. Shinohara, and T. Mitani, "Experimental Equipments for Microwave Power Transmission in Kyoto University", *Proceedings of the 4th International Conference on Solar Power from Space – SPS'04*, pp.131–138, Jul. 2004.

9. Mitani, T., N. Shinohara, H. Matsumoto, M. Aiga and K. Kuwahara, "Experimental Research and Development on Noise Reduction of 2.45GHz CW Magnetron", *Proceedings of the 4th International Conference on Solar Power from Space – SPS'04*, pp.239–244, Jul. 2004.

10. Mitani, T., N. Shinohara, H. Matsumoto, M. Aiga, and N. Kuwahara, "Experimental Research on Noise Reduction of Magnetrons for Solar Power Station/Satellite", *2004 Asia-Pacific Radio Science Conference Proceedings*, pp.603–606, Aug. 2004.

11. Katsumata, N., T. Mitani, T. Yoshimura, N. Shinohara, and Y. Imamura,"Preliminary Study on Wood Deterioration in the Simulated Space Environment", *Proceedings of the 5th International Wood Science Symposium*, p.411, Sep. 2004.

12. Kawasaki, H., T. Mitani, N. Shinohara, H. Matsumoto, and M. Mori, "Thermal Control of Transmitter for Space Satellite and Solar Power Satellite/Station", *International Astronautical Congress 2004 (IAC2004)*, Oct. 2004.

13. Mitani, T., N. Shinohara, T. Matsushima, and H. Matsumoto,"Study on High-Power Microwave Beam Forming with Transmitting System of SPORTS2.45", *Proceedings of the 2nd International Symposium on Sustainable Energy System*, p.132, Dec. 2004.

14. Shinohara, N., T. Mitani, and H. Matsumoto, "Study on Ubiquitous Power Source with Microwave Power Transmission", *Proceedings of the 2nd International Symposium on Sustainable Energy System*, p.130, Dec. 2004.

15. Nanokaichi, K., N. Shinohara, T. Mitani, H. Matsumoto, T. Kimura, and T. Mori, "A Study on Improvement of the Coupling Factor of a Slot-Coupled Active Integrated Antenna for High-Efficiency Microwave Power Transmission", *Proceedings of the 2nd International Symposium on Sustainable Energy System*, p.133, Dec. 2004.

16. Okada, K., N. Shinohara, T. Mitani, and H. Matsumoto, "Theoretical Study of mW-Class High Efficiency Rectenna", *Proceedings of the 2nd International Symposium on Sustainable Energy System*, p.136, Dec. 2004.

17. Ohashi, S., H. Usui, T. Mitani, N. Shinohara, and H. Matsumoto, "Computer Experiments on Magnetrons with 3D Electromagnetic Particle Code", *Proceedings of the 2nd International Symposium on Sustainable Energy System*, p.137, Dec. 2004.

18. Tanabe, T., Y. Baba, N. Shinohara, T. Mitani, Y. Honda and T. Watanabe, "Conversion of Japanese Cedar to Ethanol by Pretreatments with White Rot Fungi and Microwave Irradiation", *Proceedings of the 2nd International Symposium on Sustainable Energy System*, p.143, Dec. 2004.

19. Kawasaki, H., T. Mitani, N. Shinohara, H. Matsumoto, and M. Mori, "Estimation of Thermal Characteristic of Magnetron for Space Satellite and Solar Power Satellite/Station", *Proceedings of the 2nd International Symposium on Sustainable Energy System*, p.144, Dec. 2004.

20. Miyasaka, J., A. Oida, H. Nakashima, K. Ohdoi, M. Watanabe, H. Matsumoto, K. Hashimoto, N. Shinohara and T. Mitani, "Study on Mobility of Microwave-Driven Agricultural Vehicle", *Proceedings of the 2nd International Symposium on Sustainable Energy System*, p.145, Dec. 2004.

21. Kidera, S., T. Sakamoto, T. Sato, T. Mitani, and S. Sugino, "A high-resolution imaging algorithm based on scattered waveform estimation for UWB pulse radar systems", *Workshop for Space, Aeronautical and Navigational Electronics (WSANE 2005)*, Mar. 2005.

22. Shinohara, N., T. Mitani, and H. Matsumoto, "Development of Phase and Amplitude Controlled Magnetron", *Proceedings of the 6th International Vacuum Electronics Conference IVEC 2005*, pp.61–65, Apr. 2005.

23. Mitani, T., N. Shinohara, H. Matsumoto, M. Aiga, and N. Kuwahara, "Experimental Research on Generation Mechanism of Spurious Noises from Microwave Oven Magnetron", *Proceedings of the 6th International Vacuum Electronics Conference IVEC 2005*, pp.317–320, Apr. 2005.

24. Mitani, T., N. Shinohara, K. Nanokaichi and H. Matsumoto, "Numerical Simulation on Microwave Beam Pattern of SPS / Test Satellite in Consideration of Electrical and Structural Errors", *Proceedings of the XXVIIIth General Assembly of the International Union of Radio Science*, HXP.2(0789), Oct. 2005.

25. Shinohara, N., T. Mitani, and H. Matsumoto, "Study on Ubiquitous Power Source with Microwave Power Transmission", *Proceedings of the XXVIIIth General Assembly of the International Union of Radio Science*, C07.5(01145), Oct. 2005.

26. Nanokaichi, K., N. Shinohara, S. Kawasaki, T. Mitani, and H. Matsumoto, "Development of Waveguide-Slot-Fed Active Integrated Antenna for Microwave Power Transmission", *Proceedings of the XXVIIIth General Assembly of the International Union of Radio Science*, D08.4(0950), Oct. 2005.

27. Sakamoto, T., S. Kidera, T. Sato, T. Mitani, and S. Sugino, "An Experimental Studyy on a Fast and Accurate 3-D Imaging Algorithm for UWB Pulse Rader Systems", *Proceedings of the XXVIIIth General Assembly of the International Union of Radio Science*, F05.7(0921), Oct. 2005.

Presentations in Domestic Meetings

1. Tominari, H., T. Mitani, N. Shinohara, H. Matsumoto, and I. Nagano, "The study of part of power transmission on wireless electric power transmission system with Magnetron", *Proceedings of the 1999 IEICE General Conference*, p.22(B-1-22), Mar. 1999.

2. Shinohara, N., J. Fujiwara, T. Mitani, H. Matsumoto, and K. Hashimoto, "Development of Microwave Beam Control System with Phase-controlled Magnetrons", *Proceedings of the 2nd SPS Symposium*, pp.57–61, Nov. 1999.

3. Mitani, T., N. Shinohara, H. Matsumoto, M. Aiga, and T. Tsukada, "Study about increasing DC-RF Efficiency and reducing Noises of Magnetron for Microwave Power Transmission', *Proceedings of the 3rd SPS Symposium*, pp.65–69, Oct. 2000.

4. Mitani, T., N. Shinohara, H. Matsumoto, K. Hashimoto, M. Aiga, and T. Tsukada, "Study on Noise and Efficiency of Magnetron for Microwave Power Transmission", *Proceedings of the 2001 IEICE General Conference*, p.71(B-1-53), Mar. 2001.

5. Mitani, T., N. Shinohara, H. Matsumoto, and K. Hashimoto, "Compatibility of High Frequency Noises generated from Magnetron and Other Communication Systems", *Proceedings of the 4th SPS Symposium*, pp.85–89, Oct. 2001.

6. Mitani, T., N. Shinohara, H. Matsumoto, K. Hashimoto, M. Aiga, and T. Tsukada, "Improvement of Fundamental Frequency Spectrum and Spurious Noises Generated from Magnetrons after Turning off Filament Current", *Proceedings of the 5th SPS Symposium*, pp.53–58, Nov. 2002.

7. Mitani, T., N. Shinohara, H. Matsumoto, K. Hashimoto, M. Aiga, and T. Tsukada, "Improvement of Free-running Frequency Spectrum and Spurious Noises generated from Magnetron after turning off Filament Current", *Proceedings of the 2002 IEICE Society Conference*, p.36(C-2-14), Sep. 2002.

8. Mitani, T., N. Shinohara, H. Matsumoto, K. Hashimoto, M. Aiga, and T. Tsukada, "Time Domain Analysis of Frequency Spectrum of a Magnetron Driven by Non-Smoothing Half-Wave Voltage Doubler", *The 1st Domestic Symposium on Sustainable Energy System*, Jan. 2003.

9. Takeno, H., H. Nishio, Y. Ohsawa, T. Mitani, N. Shinohara, H. Matsumoto, and K. Hashimoto, "Measurement of Microwave Leakage to Develop Life Controllable Concrete", *The Papers of Technical Meeting on Electromagnetic Compatibility, IEE Japan*, pp.7–11(EMC–03–2), Jan. 2003.

10. Shinohara, N., H. Matsumoto, K. Hashimoto, and T. Mitani, "Microwave Power Transmission Experiment with SPORTS in RASC of Kyoto University", *Proceedings of the 3rd meetings Term Limited Technical group of IEICE Solar Power Satellite/Station (SPS)*, pp.1–8(SPS2002–03), Mar. 2003.

11. Takeno, H., J. Tabayashi, H. Nishio, Y. Ohsawa, K. Urabe, H. Namiki, T. Mitani, N. Shinohara, H. Matsumoto, and K. Hashimoto, "Microwave Irradiation Experiments on Real Scale Concrete to Develop Life Controllable Concrete", *Proceedings of the 3rd*

meetings Term Limited Technical group of IEICE Solar Power Satellite/Station (SPS), pp.21–26(SPS2002–13), Mar. 2003.

12. Mitani, T., N. Shinohara, H. Matsumoto, and K. Hashimoto, "Improvement of Frequency Spectrum Generated from Microwave Oven Magnetrons for Microwave Power Transmission", *Proceedings of the 3rd meetings Term Limited Technical group of IEICE Solar Power Satellite/Station (SPS)*, pp.21–26(SPS2002–18), Mar. 2003.

13. Mitani, T., N. Shinohara, H. Matsumoto, K. Hashimoto, M. Aiga, and T. Tsukada, "Time Analysis of Frequency Spectrum Generated from Magnetron Driven by Non-Smoothing Half-Wave Voltage Doubler", *Proceedings of the 2003 IEICE General Conference*, p.49(C-2-17), Mar. 2003.

14. Takeno, H., K. Urabe, H. Namiki, M. Hojo, T. Mitani, N. Shinohara, H. Matsumoto, and K. Hashimoto, "Analysis of Microwave Heating Characteristics of Easy-break Concrete", *Proceedings of The Society of Materials Science Conference, Japan*, pp.175–176(612), May. 2003.

15. Takeno, H., K. Urabe, H. Namiki, T. Mitani, and H. Matsumoto, "Measurements of Microwave Transmission and Absorption Characteristics of Easy-break Concrete", *Proceedings of Annual Conference of Civil Engineers 2003, JSCE Kansai Chapter*, pp.V-2-1–V-2-2, May. 2003.

16. Miyasaka, J., A. Oida, H. Nakashima, K. Ohdoi, S. Yamada, M. Watanabe, H. Matsumoto, K. Hashimoto, N. Shinohara, and T. Mitani, "Study on Mobility of Microwave-Driven Agricultural Vehicle – Orientation Control of Power Transmitter Using Image Processing –", *Proceedings of the 5th meetings Term Limited Technical group of IEICE Solar Power Satellite/Station (SPS)*, pp.21–28(SPS2003–14), Mar. 2004.

17. Kawasaki, H., T. Mitani, N. Shinohara, and H. Matsumoto, "Thermal Estimation of Magnetron in Vacuum", *Proceedings of the 5th meetings Term Limited Technical group of IEICE Solar Power Satellite/Station (SPS)*, pp.41–46(SPS2003–17), Mar. 2004.

18. Shinohara, N., H. Matsumoto, T. Mitani, H. Shibata, T. Adachi, K. Okada, K. Tomita and K. Shinoda, "Experimental Study on "Wireless Power Space"", *Proceedings of the 5th meetings Term Limited Technical group of IEICE Solar Power Satellite/Station (SPS)*, pp.47–53(SPS2003–18), Mar. 2004.

19. Matsumoto, H., K. Hashimoto, N. Shinohara, T. Mitani, I. Mikami, K. Kitoh, and K. Kawasaki, "COE Research of Space Power Transmission and Roadmap", *Proceedings of the 2nd Domestic Symposium on Sustainable Energy System*, p.31, Mar. 2004.

20. Mitani, T., N. Shinohara, H. Matsumoto, M. Aiga, and T. Handa, "Study of Low-Noise Magnetron for Microwave Power Transmission", *Proceedings of the 2nd Domestic Symposium on Sustainable Energy System*, p.36, Mar. 2004.

21. Matsumoto, H., K. Hashimoto, N. Shinohara and T. Mitani, "COE of Space Solar Power System", *Proceedings of the 2nd Domestic Symposium on Sustainable Energy System*, p.95, Mar. 2004.

22. Mitani, T., H. Kawasaki, N. Shinohara and H. Matsumoto, "Estimation of Thermal Control of Magnetron in Vacuum Environment", *Proceedings of the 2nd Domestic Symposium on Sustainable Energy System*, p.98, Mar. 2004.

23. Kato, S., N. Shinohara, T. Mitani and H. Matsumoto, "Study of Development of Phase and Amplitude Controlled Magnetron", *Proceedings of the 2nd Domestic Symposium on Sustainable Energy System*, p.101, Mar. 2004.

24. Mizutani, H., N. Shinohara, T. Mitani and H. Matsumoto, "Development of Low-Loss Phase Controlled Magnetron System", *Proceedings of the 2nd Domestic Symposium on Sustainable Energy System*, p.102, Mar. 2004.

25. Shibata, H., N. Shinohara, T. Mitani, H. Matsumoto and K. Hashimoto, "Study on "Wireless Power Space System"", *Proceedings of the 2nd Domestic Symposium on Sustainable Energy System*, p.103, Mar. 2004.

26. Tomita, K., N. Shinohara, T. Mitani, and H. Matsumoto, "Development of Wireless Power Transmitter for Wireless Power Space", *Proceedings of the 2nd Domestic Symposium on Sustainable Energy System*, p.104, Mar. 2004.

27. Shinoda, K., N. Shinohara, T. Mitani, and H. Matsumoto, "Development of Rectenna and Receiving System for Wireless Power Space", *Proceedings of the 2nd Domestic Symposium on Sustainable Energy System*, p.104, Mar. 2004.

28. Mitani, T., N. Shinohara, H. Matsumoto, M. Aiga, and T. Handa, "Study on Noises of Magnetron from Viewpoint of Anode Voltage and Interaction Space Width", *Proceedings of the 2004 IEICE General Conference*, pp.S3–S4(SBC-1-2), Mar. 2004.

29. Nanokaichi, K., N. Shinohara, T. Mitani, H. Matsumoto, T. Kimura, and T. Mori, "Development of Microwave Power Transmission System with Active Integrated Antenna", *Proceedings of the 7th SPS Symposium*, pp.55–60, Sep. 2004.

30. Kawasaki, H., M. Mori, T. Mitani, N. Shinohara, and H. Matsumoto, "Effect of Temperature on the Efficiency of Transmitter", *Proceedings of the 7th SPS Symposium*, pp.85–88, Sep. 2004.

31. Mitani, T., N. Shinohara, T. Matsushima, and H. Matsumoto, "Study on High-Power Microwave Beam Forming with Transmitting System of SPORTS2.45", *Proceedings of the 7th SPS Symposium*, pp.120–125, Sep. 2004.

32. Sakamoto, T., S. Kidera, T. Sato, T. Mitani, and S. Sugino, "An experimental study on accurate shape estimation algorithm for UWB pulse radar systems", *Proceedings of the 8rd meetings Term Limited Technical group of IEICE Solar Power Satellite/Station (SPS)*, pp.25–31(SPS2004–15), Feb. 2005.

33. Takeno, H., N. Nishikawa, J. Tabayashi, Y. Yasaka, Y. Kobayashi, M. Tsuji, K. Ohno, H. Namiki, T. Mitani, N. Shinohara, and K. Hashimoto, "Basic Experiments for Detection of Defects and Reinforcing Bars in Concrete by Microwave Irradiation", *Proceedings of the 8rd meetings Term Limited Technical group of IEICE Solar Power Satellite/Station (SPS)*, pp.33–38(SPS2004–16), Feb. 2005.

34. Ohashi, S., H. Usui, T. Mitani, N. Shinohara, and H. Matsumoto, "Computer Experiments on Magnetrons with 3D Electromagnetic Particle Code", *Proceedings of the 8th meetings Term Limited Technical group of IEICE Solar Power Satellite/Station (SPS)*, pp.1–7(SPS2004–17), Feb. 2005.

35. Mitani, T., N. Shinohara, H. Matsumoto, M. Aiga, N. Kuwahara, and T. Ishii, "Research and Development on Low-Noise Magnetron for Microwave Oven –Consideration on Time-Domain Analysis Experiments of Noises–", *Proceedings of the 8th meetings Term Limited Technical group of IEICE Solar Power Satellite/Station (SPS)*, pp.9–14(SPS2004–18), Feb. 2005.

36. Miyasaka, J., A. Oida, H. Nakashima, K. Ohdoi, M. Watanabe, H. Miyanaga, H. Matsumoto, K. Hashimoto, N. Shinohara, and T. Mitani, "Study on Control for Microwave-Driven Agricultural Vehicle and Effects of Microwave Exposure on Radish Seed Germination", *Proceedings of the 8th meetings Term Limited Technical group of IEICE Solar Power Satellite/Station (SPS)*, pp.15–24(SPS2003–19), Feb. 2005.

37. Kawasaki, H., T. Mitani, N. Shinohara, and H. Matsumoto, "Thermal Estimation of An Efficiency of Magnetron", *Proceedings of the 8th meetings Term Limited Technical group of IEICE Solar Power Satellite/Station (SPS)*, pp.23–27(SPS2004–20), Feb. 2005.

38. Shinohara, N., K. Okada, T. Mitani, and H. Matsumoto, "Study on Parameter Optimization of Rectifying Circuit of Rectenna for Microwave Power Transmission", *The 24th ISAS Space Energy Symposium*, Mar. 2005.

39. Ohashi, S., H. Usui, T. Mitani, N. Shinohara, and H. Matsumoto, "Computer Experiments on Magnetrons with 3D Electromagnetic Particle Code", *The 24th ISAS Space Energy Symposium*, Mar. 2005.

40. Kidera, S., T. Sakamoto, T. Sato, T. Mitani, and S. Sugino, "An experimental study on a high-resolution imaging algorithm based on scattered waveform estimation for UWB pulse radar systems", *Proceedings of the 2005 IEICE General Conference*, p.25(B-1-25), Mar. 2005.

41. Sakamoto, T., S. Kidera, T. Sato, T. Mitani, and S. Sugino, "An experimental study on a fast algorithm of 3-dimensional imaging for UWB pulse radars", *Proceedings of the 2005 IEICE General Conference*, p.26(B-1-26), Mar. 2005.

42. Nanokaichi, K., N. Shinohara, S. Kawasaki, T. Mitani, and H. Matsumoto, "A Waveguide-slot-fed Active Integrated Antenna for Microwave Power Transmission", *Proceedings of the 2005 IEICE General Conference*, p.162(C-2-129), Mar. 2005.

43. Shinohara, N., H. Matsumoto, K. Hashimoto, T. Mitani, H. Usui and H. Kojima, "Research of Microwave Power Transmission in Kyoto University", *Proceedings of the 9th meetings Term Limited Technical group of IEICE Solar Power Satellite/Station (SPS)*, pp.11–17(SPS2005–03), Apr. 2005.

44. Takeno, H., M. Takenaka, N. Nishikawa, M. Tsuji, H. Namiki, and T. Mitani, "Basic Experiments for Detection of Defects and Reinforcing Bars in Concrete by Microwave Irradiation", *Proceedings of Annual Conference of Civil Engineers 2003, JSCE Kansai Chapter*, May. 2005.

45. Kawasaki, H., T. Mitani, N. Shinohara, and H. Matsumoto, "Fundamental Estimation of Magnetron with Constant Temperature", *Proceedings of the 10th meetings Term Limited Technical group of IEICE Solar Power Satellite/Station (SPS)*, pp.7–10(SPS2005–06), Jun. 2005.

46. Fukutani, K., T. Mitani, N. Shinohara and H. Matsumoto, "Evaluation of Basic Performance of 5.8GHz Magnetron", *Proceedings of the 8th SPS Symposium*, in poress, Sep. 2005.

47. Mitani, T., H. Kawasaki, N. Shinohara and H. Matsumoto, "Basic Experiments on DC-RF Conversion Efficiency and Frequency Spectrum of Magnetron in Continuous Run", *Proceedings of the 49th Space Sciences and Technology Conference*, pp.203–208, Nov. 2005.

48. Kimura, T., T. Mori, K. Nanokaichi, T. Mitani, N. Shinohara and H. Matsumoto, "Study on High-efficiency Microwave Power Transmission of Slotted Waveguide Power Divider", *Proceedings of the 49th Space Sciences and Technology Conference*, pp.209–212, Nov. 2005.